PUBLICATIONS OF
THE UNIVERSITY OF EASTERN FINLAND

Dissertations in Health Sciences

LAURI JUHANI LEHTO

APPLICATIONS OF SWEEP IMAGING WITH FOURIER TRANSFORMATION (SWIFT)

Imaging brain microstructure and calcifications

Applications of Sweep Imaging with Fourier Transformation (SWIFT)

LAURI JUHANI LEHTO

Applications of Sweep Imaging with Fourier Transformation (SWIFT)

Imaging brain microstructure and calcifications

To be presented by permission of the Faculty of Health Sciences, University of Eastern Finland for public examination in the auditorium of Tietoteknia, University of Eastern Finland, Kuopio, on Tuesday, April 5th 2016, at 12 noon

Publications of the University of Eastern Finland
Dissertations in Health Sciences
Number 339

A. I. Virtanen Institute for Molecular Sciences, Department of Neurobiology, Faculty of Health Sciences, University of Eastern Finland
Kuopio
2016

Grano Oy
Jyväskylä, 2016

Distributor:
University of Eastern Finland
Kuopio Campus Library
P.O.Box 1627
FI-70211 Kuopio, Finland
http://www.uef.fi/kirjasto

ISBN (print): 978-952-61-2067-6
ISBN (pdf): 978-952-61-2068-3
ISSN (print): 1798-5706
ISSN (pdf): 1798-5714
ISSN-L: 1798-5706

Author's address: Department of Neurobiology, A. I. Virtanen Institute for Molecular Sciences
University of Eastern Finland
KUOPIO, FINLAND

Supervisors: Professor Olli Gröhn, Ph.D.
Department of Neurobiology, A. I. Virtanen Institute for Molecular Sciences
University of Eastern Finland
KUOPIO, FINLAND

Alejandra Sierra López, Ph.D.
Department of Neurobiology, A. I. Virtanen Institute for Molecular Sciences
University of Eastern Finland
KUOPIO, FINLAND

Assistant Professor Curtis Corum, Ph.D.
Department of Radiology, Center for Magnetic Resonance Research
University of Minnesota
MINNEAPOLIS, USA

Reviewers: Professor Mark Does, Ph.D.
Department of Biomedical Engineering
Vanderbilt University
NASHVILLE, USA

Associate Professor Jang-Yeon Park, Ph.D.
IBS Center for Neuroscience Imaging Research
Sungkyunkwan University
SUWON, REPUBLIC OF KOREA

Opponent: Lecturer Karin Shmueli, Ph.D.
Department of Medical Physics and Biomedical Engineering
University College London
LONDON, UK

Lehto, Lauri
Applications of Sweep Imaging with Fourier Transform (SWIFT)
University of Eastern Finland, Faculty of Health Sciences
Publications of the University of Eastern Finland. Dissertations in Health Sciences 339. 2016. 85 p.

ISBN (print): 978-952-61-2067-6
ISBN (pdf): 978-952-61-2068-3
ISSN (print): 1798-5706
ISSN (pdf): 1798-5714
ISSN-L: 1798-5706

ABSTRACT

Sweep imaging with Fourier transform (SWIFT) is a magnetic resonance imaging (MRI) technique with virtually simultaneous excitation and acquisition. This enables imaging of so-called short T_2^* components with extremely fast decaying signals. The aim of this thesis was to demonstrate the benefits of SWIFT for imaging the brain using both magnitude and phase contrast.

A calcification in the brain forms because of disturbed energy metabolism in the tissue. These structures can be difficult to detect with MRI and hard to distinguish from e.g. hemorrhages since both cause a fast T_2^* decay. Reliable detection of calcifications would provide an additional way of assessing disease progression. In addition, the calcifications are known to be diamagnetic and likely to be visible in phase contrast. Hence, SWIFT magnitude and magnitude contrasts were applied to detect the calcifications formed after traumatic brain injury (TBI) as well as after epileptic seizures in animal models. Furthermore, since in the near absence of echo time, it could be thought that the SWIFT phase contrast is counterintuitive; therefore phase contrast was further evaluated in healthy brain tissue. Multiple properties of the contrast were examined in detail.

The sensitivity of SWIFT magnitude contrast was evaluated further by measuring the magnetization transfer (MT) ratio with SWIFT to assess the integrity of the thalamocortical pathway in rats after a TBI with a comparison to diffusion tensor imaging (DTI). Importantly, a histological analysis of cell density (Nissl), myelin and iron (Perls') was conducted to clarify the results of the MRI assessment.

SWIFT detected hyperintense and hypointense calcifications in the magnitude images, the latter being easily detected and distinguished from bleeding in the phase contrast image. The difference in magnitude contrast was related to the size of the granules forming the calcifications. The SWIFT phase contrast in brain structures was shown to be somewhat similar to conventional phase contrast, however, with crucial differences related to the spatial frequency content. Simulations and a separate MT experiment demonstrated a possibility for short T_2^* phase imaging. After TBI, and unlike the situation with DTI, MT-SWIFT revealed changes in all of the analyzed areas. According to the histological evaluation, the changes in the MT were mainly related to a loss of myelinated fibers

The results of this work may provide new methods for imaging healthy and diseased brain. Further studies will be needed to clarify the optimal way to exploit the short T_2^* sensitivity of SWIFT in brain imaging applications.

National Library of Medicine Classification: WL 141.5.M2, WL 300, WL 354, WL 385, WN 185
Medical Subject Headings: Diagnostic Imaging; Magnetic Resonance Imaging; Fourier Analysis; Brain; Brain Injuries; Epilepsy; Seizures; Disease Progression; Disease Models, Animal; Rats

Lehto, Lauri
SWIFT-magneettikuvausmenetelmän soveltaminen aivoissa
Itä-Suomen yliopisto, terveystieteiden tiedekunta
Publications of the University of Eastern Finland. Dissertations in Health Sciences 339. 2016. 85 s.

ISBN (print): 978-952-61-2067-6
ISBN (pdf): 978-952-61-2068-3
ISSN (print): 1798-5706
ISSN (pdf): 1798-5714
ISSN-L: 1798-5706

TIIVISTELMÄ

Sweep imaging with Fourier transformation (SWIFT) on magneettikuvausmenetelmä (MK menetelmä) jossa signaalin viritys ja keräys tapahtuvat lähes yhdenaikaisesti. Tämä mahdollistaa ns. lyhyiden T_2^* komponenttien erittäin nopeasti häviävän signaalin havaitsemisen. Tämän työn tarkoitus oli havainnollistaa SWIFT tekniikan hyötyjä aivojen MK:ssa käyttäen sekä magnitudi-, että vaihekontrastia.

Aivokalsifikaatio voi muodustua kudoksen häiriintyneen energiametabolismin seuraksena. Niitä on vaikea havaita MK:lla ja ne on helppo sekoittaa aivoverenvuotoihin, koska molemmat lyhentävät T_2^*:ä. Aivokalsifikaatioiden varma havannointi MK:lla antaisi lisäkeinon arvioida tautien kehitystä. Kalsifikaatioiden tiedetään myös olevan diamagneettisia, joten pidettiin todennäköisenä, että niitä voitaisiin havaita vaihekontrastin avulla. Tämän vuoksi tässä työssä hyödynnettiin SWIFT:n magnitudi- ja vaihekontrasteja aivokalsifikaatioiden havaitsemisessa epileptisen kohtauksen ja traumaattisen aivovamman (TA:n) rottaeläinmalleissa. Lisäksi koska SWIFT:n vaihekontrasti oli minimoidun kaikuajan mielessä epäintuitiivinen, SWIFT vaihekontrastin eri aspekteja tutkittiin tarkemmin terveessa aivokudoksessa.

SWIFT:n magnitudikontrastin herkkyyttä tutkittiin tarkemmin *magnetization transfer* (MT) tekniikan avulla tarkastelemalla TA:n jälkeisiä talamokortikaaliseen yhteyteen muodostuvia verraten pieniä vaurioita. SWIFT:ä verrattiin *diffusion tensor imaging* (DTI) tekniikkaan. Jotta voisimme paremmin selittää MK:n tuloksia, tehtiin lisäksi kattava histologinen tutkimus solutiheydestä, sekä myeliini- ja rautapitoisuuksista.

Aivokalsifikaatioita havaittiin SWIFT:llä magnitudikuvissa ympäristöönsä verrattuna kirkkaina ja tummina, joista jälkimmäiset erottuivat helposti aivoverenvuodoista käyttäen vaihekuvia. Magnitudikuvien vaihteleva kontrasti liitettiin kalsifikaation muodustumisen eri vaiheisiin niin, että kirkaana näkyvä kalsifikaatio kehittyy lopulta tummaksi. SWIFT vaihekontrasti aivoissa oli perinteisiin menetelmiin verrattuna samankaltainen, mutta myös merkittäviä eroja nähtiin liittyen eri rakenteiden erilaisiin spatiaalitaajuusjakaumiin. Simulaatiot ja erillinen MT koe toivat ilmi myös mahdollisuuden lyhyiden T_2^* komponenttien vaihekontrastin muodostamiseksi. TA:n jälkeen, toisin kuin DTI, MT-SWIFT havaitsi muutoksia lähes kaikissa analysoiduissa talamokortikaalisen yhteyden alueissa. MT muutokset liitettiin histologisten tulosten perusteella lähinnä myelinisoitujen aksonien häviämiseen.

Nämä tulokset tarjoavat uusia mahdollisuuksia aivokuvantamiseen. SWIFT:n lyhyiden T_2^* kompponenttien herkkyyden entistä parempaan hyväksikäyttöön tarvitaan lisätutkimuksia.

Luokitus: WL 141.5.M2, WL 300, WL 354, WL 385, WN 185
Yleinen suomalainen asiasanasto: kuvantaminen; magneettitutkimus; aivot; aivovammat; aivovauriot; epilepsia; koe-eläinmallit; rotat

Acknowledgements

The experimental work in this thesis was carried out between 2008 and 2015 in the Biomedical NMR research group housed in the University of Eastern Finland, A. I. Virtanen Institute for Molecular Medicine, Department of Neurobiology. The work involved close collaboration with the University of Minnesota, Center for Magnetic Resonance Research, where the author spent the winters of 2008-2009 and 2011-2012.

I am most grateful to my principal supervisor Professor Olli Gröhn, Ph.D., for the guidance, expertise, and seemingly unending calmness supply of serenity and reason when things were not going our way. I feel that I have been lucky to have such a humane chief during these years. I am very thankful for my second supervisor Alejandra Sierra Lopez, Ph.D., not only for her indispensable help with the more biological aspects of my work, but also for all the encouragement, the numerous jokes and never-ending banter. She has taught me always to strive to do the best that I can. I am also very grateful to my third advisor Curtis Corum, Ph.D., for his invaluable advice on the more technical side of my work. He truly inspired me with his contagious enthusiasm on all things engineering and science in general. I further thank Professor Asla Pitkänen, Ph.D., for her help and expertise for my work.

My thesis would not have been possible without the generosity of Professor Michael Garwood, Ph.D., who was kind enough to let our group in Kuopio have the SWIFT pulse sequence and also let me work in his research group with all its brilliant members. I also want to thank Assistant Professor Djaudat Idiyatullin, Ph.D., for his work on SWIFT and all the assistance he gave me while I was working in Minnesota.

I thank my official pre-examiners Professor Mark Does, Ph.D., and Associate Professor Jang-Yeon Park, Ph.D., for their invaluable criticism and feedback that clearly improved my thesis. I also want to thank Professor Ewen Mac Donald, Ph.D., for proofreading my thesis.

I want to thank the current and former members of my research group for their help and good times during these years, especially: Kimmo Jokivarsi, Ph.D., for always being such reliable lunch company, Joonas Autio, Ph.D., for great discussion about anything and everything, Juha-Pekka Niskanen, M.Sc., for giving us Aedes, and our technician Maarit Pulkkinen without whom we would be doomed. I also express my thanks to Artem Shatillo, M.D., Joanna Huttunen, Ph.D., Antti Airaksinen, M.Sc., Ekaterina Zhurakovskaya, M.Sc., Teemu Laitinen, M.Sc., Tuukka Miettinen, M.Sc., Raimo Salo, M.Sc., Eppu Manninen, M.Sc., Jaakko Paasonen, M.Sc, Riikka Immonen, Ph.D., Johanna Närväinen, Ph.D., and Mikko Kettunen, Ph.D. I also want to thank the MRI people of Kuopio outside my own group for their help and company: Timo Liimatainen, Ph.D., Mikko Nissi, Ph.D., Jari Rautiainen, Ph.D., Karthik Chary, M.Sc., Hanne Hakkarainen, M.Sc., Elias Ylä-Herttuala, M.Sc., Amna Yasmin, M.Sc., and Muhammad Arsalan Khan, M.Sc.

Finally, I want to thank my parents who have always supported me in everything, no matter how grumpy I was. We are now all Ph.Ds.

I also acknowledge the funders of my research: Doctoral Program for Molecular Medicine, ASLA-Fulbright, Emil Aaltonen Foundation, Finnish Cultural Foundation of Northern Savo, Finnish Foundation for Advancing Technology and the European Union's Seventh Framework Programme (FP7/2007-2013) under grant agreement n°602102 (EPITARGET).

Minneapolis, March 2016

Lauri Lehto

x

List of the original publications

This dissertation is based on the following original publications:

I Lehto L J, Sierra A, Corum C A, Zhang J, Idiyatullin D, Pitkänen A, Garwood M and Gröhn O. Detection of calcifications *in vivo* and *ex vivo* after brain injury in rat using SWIFT. *NeuroImage 61: 761-772, 2012.*

II Lehto L J, Garwood M, Gröhn O and Corum C A. Phase imaging in brain using SWIFT. *J Magn Reson 252: 20-28, 2015.*

III Lehto L J, Sierra A, and Gröhn O. Magnetization transfer SWIFT MRI detects myelin loss in the thalamocortical pathway more consistently than DTI after traumatic brain injury in rat. *Submitted*.

Contents

Abbreviations

3D	three dimensional
AD	axial diffusion
ADC	apparent diffusion coefficient
AIVI	A. I. Virtanen Institute
b0	non-diffusion weighted image for DTI
BPF	bound pool fraction
BSA	bovine serum albumin
BW	bandwidth
CCI	controlled cortical impact
CEST	chemical exchange saturation transfer
CMRR	Center for Magnetic Resonance Research
CNR	contrast-to-noise ratio
CT	computerized tomography
DAI	diffuse axonal injury
DTI	diffusion tensor imaging
DWI	diffusion weighted imaging
EAE	experimental autoimmune encephalomyelitis
FA	fractional anisotropy
FID	free induction decay
FLAIR	fluid attenuated inversion recovery
FOV	field of view
FPI	fluid percussion injury
FT	Fourier transform
GM	gray matter
GRE	gradient recalled echo
GRE3D	three dimensional gradient recalled echo
HS	hyperbolic secant pulse
IFT	inverse Fourier transform
LFPI	lateral fluid percussion injury
MGRE3D	three dimensional multi gradient echo
MRI	magnetic resonance imaging
MT	magnetization transfer
MTR	magnetization transfer ratio
NMR	nuclear magnetic resonance
PSF	point spread function
qMT	quantitative magnetization transfer
QSM	quantitative susceptibility mapping
RD	radial diffusion
RF	radio frequency
ROI	region of interest
SE	spin echo
SNR	signal-to-noise ratio
SSFP	steady state free precession
SW	spectral width, acquisition bandwidth
SWI	susceptibility weighted imaging
TBI	traumatic brain injury
TE	echo time
TMSP	tetramethyl-silyl-propionate
TR	repetition time
UTE	ultra-short echo time
WASSR	water saturation shift referencing
WM	white matter

ZTE	zero echo time

1 Introduction

Magnetic resonance imaging (MRI) is the most versatile medical imaging modality currently available. Modern MRI can be used to study all kinds of biological tissue and it is able to monitor a wide variety of physiological functions. MRI is based on magnetic fields six orders of magnitude stronger than the Earth's magnetic field, yet this magnetic field can be adjusted to much less than 1 ppm homogeneity and similarly these kinds of small magnetic field inhomogeneities can be exploited to obtain contrast.

Historically, nuclear magnetic resonance (NMR) experiments were made by sweeping through different resonance frequencies to excite signal from different chemical components. Soon afterwards, pulsed excitation was invented (Hahn 1950); this is still the predominant way of creating a signal in MRI. The first MRI images were taken with pulsed RF excitation by radially rotating the sample in a magnetic field gradient (Lauterbur 1973), although radial MRI was largely forgotten after the invention of Cartesian imaging (Mansfield & Maudsley 1977). Now, after many years of MRI, the development of a novel pulse sequence, sweep imaging with Fourier transform (SWIFT) (Idiyatullin et al. 2006) has closed the circle back to the historical frequency sweep excitation with radial data collection. This makes it possible for SWIFT to have a minimized delay between signal excitation and detection, almost avoiding any signal decay during this delay. This enables imaging of tissues like bone and cartilage that have proved difficult applications for conventional MRI.

This thesis concentrated on imaging healthy and pathological brain tissue using SWIFT. Brain is usually thought to emit an NMR signal that decays relatively slowly and is easily detected by conventional methods. However, there is evidence also that fast decaying components exist in neural tissue (Horch et al. 2011), motivating the use of SWIFT also in brain imaging.

The structural imaging of the brain in one sense is quite straightforward, as the brain provides a plethora of signal, is immobile and easily shimmed. However, the brain is clearly the most complicated organ in the human body and furthermore, it can suffer a multitude of different pathological processes each producing their signature alterations of the brain tissue. The blessing—or sometimes the curse—of MRI is that due its complexity, MRI requires that one seeks optimal methods for each aspect of a disease on a larger scale than any other medical imaging modality.

Studies **I** and **III** aimed to show the benefits of SWIFT in imaging two types of consequences of an insult to the brain tissue: pathological accumulation of calcium i.e. a calcification, in the thalamus, and structural changes of the thalamocortical pathway after a traumatic brain injury (TBI). Reliable detection of the calcification could enable a better estimation of disease progression, whereas a more robust assessment the integrity of the thalamocortical pathway after TBI could be used as a predictor for the outcome of the injury.

Most MRI studies concentrate on measuring the magnitude of the detected signal. However, the MRI signal also has a phase component that carries information of minute local magnetic field variations that can be related to the properties of the tissue. Conventionally, this so-called phase imaging has been conducted with gradient recalled echo (GRE) in which there is a relatively long delay between excitation and acquisition. However, as SWIFT had been shown to also obtain a phase contrast by using iron nanoparticles (Zhou et al. 2010) that strongly change the magnetic field, one component of study **I** continued this line of work by utilizing SWIFT phase contrast for the detection of the calcifications. At first, the existence of SWIFT phase contrast may have seemed somewhat counterintuitive in the virtual absence of any delay from excitation to acquisition, and study **I** found that although SWIFT phase contrast appeared to be similar, it was not the same as obtained for GRE. As phase imaging of the brain structures

has become an increasingly important field of MRI, study **II** concentrated on examining in detail the behavior of SWIFT phase contrast in brain.

The following two chapters will briefly examine the theoretical concepts relevant to the experimental part of this thesis and review the most important literature concerned with the individual studies.

2 Magnetic resonance imaging

This section briefly reviews the basics of the origins and behavior of the NMR signal, how it can be utilized to create an MRI image and finally describes some of the MRI pulse sequences relevant to this thesis.

2.1 NUCLEAR MAGNETIC RESONANCE

NMR depends on the magnetic dipole moment $\boldsymbol{\mu}$ of the nucleus that is related to the quantized spin angular momentum $\boldsymbol{S}$. Only nuclei with odd atomic mass numbers have a large spin angular momentum, so most conventional NMR is associated with these types of nuclei. The potential energy E of the magnetic moment in the presence of a magnetic field $\boldsymbol{B}$ can be written (Nishimura. 2010):

$$E = -\boldsymbol{\mu} \cdot \boldsymbol{B} = -\mu_z B_0 = -\gamma S_z B_0, \tag{1}$$

where the direction of the magnetic field has been set to be the z-direction (B_0), μ_z and S_z are the z-components of the spin angular momentum and the magnetic dipole moment, respectively, and γ is the nucleus specific gyromagnetic ratio. MRI is usually based on the signal from the hydrogen nuclei of water molecules present in the various environments of differing tissues. Since hydrogen has the simplest atomic nucleus with only one proton and no neutrons, S_z assumes one of two quantized states, $\pm 1/2\hbar$, where $\hbar$ is the Planck constant divided by 2π. This can be interpreted as μ_z of the nucleus being oriented either parallel or anti-parallel to the magnetic field. From Eq. 1, the anti-parallel state has a slightly higher energy. The energy difference between these states is:

$$\Delta E = \gamma \hbar B_0. \tag{2}$$

Thermal energy is sufficient to populate the upper state. The population ratio of the states is described by the Boltzmann distribution:

$$\frac{n_-}{n_+} = e^{-\Delta E/kT}, \tag{3}$$

where n_- and n_+ are the number of anti-parallel and parallel states of magnetic moments, respectively, k is the Boltzmann's constant and T is the absolute temperature. This ratio is close to unity at room temperatures with the commonly used magnetic field strengths, but there exists a large enough population difference that can be utilized to produce an NMR signal. The population difference leads to a net macroscopic magnetization $\boldsymbol{M} = \sum \boldsymbol{\mu}$ summing over all nuclei in a unit volume. The magnetic field exerts a torque on the net magnetization so that (Nishimura. 2010):

$$\frac{d\boldsymbol{M}}{dt} = \boldsymbol{M} \times \gamma \boldsymbol{B}. \tag{4}$$

This is one form of the Bloch equation (Bloch 1946), which describes the behavior of the net magnetization in the presence of an external magnetic field. From Eq. (4) the angular frequency of the net magnetization around the magnetic field $\boldsymbol{B}$ can be solved:

$$\omega_0 = -\gamma B_0. \tag{5}$$

In Eq. (5), ω_0, is the Larmor angular frequency, which by convention is referred to as the Larmor frequency. In quantum mechanical terms, the Larmor frequency is seen to be the angular frequency of a photon with energy corresponding to the difference between the two nuclear spin energy states. In order to create the signal, the sample is irradiated with a macroscopic RF field with this same frequency in order to induce transitions between the states. A much more in depth quantum mechanical analysis would be necessary if one wished to examine in more precise detail how the signal comes to exist, but that is beyond the scope of this thesis. According to the classical description, another rotating magnetic field, $\boldsymbol{B_1}$, is applied at the Larmor frequency perpendicular to the B_0 direction z, on the xy-plane. By using Eq. (4) the effect of this applied $\boldsymbol{B_1}$-field is to rotate the net magnetization $\boldsymbol{M}$ around the axis of $\boldsymbol{B_1}$ towards the xy-plane itself as long as $\boldsymbol{B_1}$ is on. Once perturbed from the z-direction, $\boldsymbol{M}$ continues to precess around the main magnetic field at the Larmor frequency. The circular motion of M_{xy}, the component of $\boldsymbol{M}$ in the xy-plane, induces an electromotive force in a receiving coil surrounding the sample enabling signal detection. This signal is called the free induction decay (FID) (Nishimura. 2010). The same coil can also be used to transmit the excitation field $\boldsymbol{B_1}$. The angle of the magnetization $\boldsymbol{M}$ as measured from the z-axis, the so-called flip angle, is written as follows (Bernstein et al. 2004):

$$\theta(t) = \int_{t'=0}^{T_p} B_1(t')dt', \tag{6}$$

where integration variable t' is time, T_p is the duration of the RF pulse and B_1 is the amplitude of the $\boldsymbol{B_1}$-field.

The frequency of $\boldsymbol{B_1}$ does not have to be exactly at the Larmor frequency. In this case, the net magnetization rotates around an effective field:

$$\boldsymbol{B}_{eff} = \boldsymbol{B_1} + \boldsymbol{\Delta B}, \tag{7}$$

where $\boldsymbol{\Delta B}$ is an additional fictitious field corresponding to the frequency difference in comparison to the Larmor frequency. To be more exact, it arises due to the frequency difference to the so-called rotating frame of a reference rotating at the Larmor frequency that is used to simplify the analysis of the behavior of the magnetization (Garwood & Delabarre 2001). Thus, with off-resonance, the flip angle becomes more complicated than in Eq. (6) as the effective field does not lie on the xy-plane. For example, if the angle of the effective field to the xy-plane is <45°, a full excitation or a 90° flip angle cannot be achieved as the magnetization cannot rotate to such an extent.

The $\boldsymbol{B_1}$ field is induced by so-called radio frequency (RF) pulses that have both a magnetic and an electric field component. The magnetic field component is used to manipulate the net magnetization, whereas the electric field component only acts as a source for potentially harmful energy deposition within the tissue. By controlling the amplitude, frequency and/or phase of the pulse, one can control the properties of the $\boldsymbol{B_1}$ field, and thus, importantly, the effective field $\boldsymbol{B}_\mathrm{eff}$ (Garwood & Delabarre 2001). This enables changing the flip angle, and also which frequencies are affected. This latter property is crucial for the design of practical RF-pulses, since the magnetic field B_0 is never truly homogeneous due to various reasons.

2.2 RELAXATION

After perturbation of the net magnetization from the z-axis using an RF-pulse, the magnetization immediately begins to recover back to the z-axis. In most cases the xy-component of the net magnetization decays faster than the z-component recovers (Traficante 1991). This section briefly describes different types of relaxation mechanisms for the NMR signal.

2.2.1 Longitudinal relaxation

The return of the z-component of the net magnetization, M_z, to thermal equilibrium described by Eq. (3), is called spin-lattice relaxation. This name comes from the energy exchange between the excited spin and its surroundings, the "lattice". According to the Bloembergen-Purcell-Pound-theory (Bloembergen et al. 1948), in the so-called motional averaging regime, where the random motions of molecules, especially in a liquid or solution, averages the dipolar interaction between the nuclei, then the spin-lattice relaxation can be described by an exponential decay constant T_1 such that (Nishimura. 2010):

$$M_z(t) = M_{z,0} - \left[M_{z,0} - M_z(0)\right]e^{-\frac{t}{T_1}}, \tag{8}$$

where M_z(t) is the z component of the net magnetization at time t and $M_{z,0}$ is the thermal equilibrium value. The origin of T_1 relaxation is the thermal random motion (including rotation and vibration) of molecules, their magnetic moments and associated magnetic fields. The dipolar component of the magnetic field predominates at most distances. Analogous to the $\boldsymbol{B_1}$ field, any magnetic field with a component in the xy-plane and oscillating near the Larmor frequency of a nucleus can cause transitions in the corresponding energy levels. Hence, the random motions of the ensemble of surrounding molecules generate a randomly fluctuating magnetic field at the nucleus of interest. The field induces a transition and energy is exchanged between the nucleus and the surrounding molecular lattice. This process is known as dipole-dipole relaxation. The source for the field does not have to be another same species nucleus, molecule or a differing molecule in solution; it can also be something else, such as the magnetic field surrounding an iron nanoparticle (Miguel et al. 2007).

A very important concept in relaxation theory is the Fourier transform (FT) of the autocorrelation function of the fluctuating fields due to the molecular motion that the nucleus experiences: the spectral density. In a simplified, but nonetheless informative manner, the spectral density for spin-lattice relaxation is (Gadian. 1995):

$$J(\omega) = \frac{\tau_c}{1 + \omega^2\tau_c^2}, \tag{9}$$

where τ_c is the so called correlation time describing the rate of molecular tumbling and ω is the angular frequency of the motion. T_1 can be shown to be inversely proportional to the spectral density:

$$T_1 \propto B_{xy}^2 \frac{\tau_c}{1 + \omega_0^2\tau_c^2}, \tag{10}$$

where B_{xy} is the amplitude of the fluctuating field on the xy-plane and ω_0 is the Larmor frequency. From Eq. (10) we can see that the minimum of T_1 is at Larmor frequency, which is reasonable since the energy level transitions are most easily induced at the Larmor frequency.

2.2.2 Transversal relaxation

The decay of the net transverse or xy-plane magnetization is called spin-spin relaxation. Two nuclear spins or nuclear magnetic moments interact, but no energy is exchanged with the lattice. The origin of transverse relaxation is in nuclei experiencing slightly different local, transverse or z-directional, magnetic fields. Nearby nuclei as well as other microscopic and macroscopic sources make contributions. If one considers two nuclei, if they are immobile, they will experience static and possibly differing fields due to each other's presence. The magnitude and sign of the field experienced will depend on the relative orientation of the two nuclei and their orientations with respect to the $\boldsymbol{B_0}$ field. In the case of a powdered solid, all nuclei are immobile and all possible orientations exist, hence, there is a wide distribution of resonance frequencies. The signal from nuclear populations with differing orientations will acquire phase differences, causing destructive interference, leading to a rapid decay of the net signal as summed over all the nuclei. On the other hand, in a liquid, the molecules are tumbling,

vibrating and translating rapidly at the microscopic scale. On average, the nuclei will experience much smaller variations of the magnetic field, leading to a slower signal decay.

Furthermore, given that the tumbling motion of the molecules is rapid, as in a liquid, the Bloembergen-Purcell-Pound-theory theory applies and the decay of the transverse magnetization is governed by an exponential decay constant so that (Nishimura. 2010):

$$M_{xy}(t) = M_{xy}(0)e^{-t/T_2}, \tag{11}$$

where $M_{\mathrm{xy}}(t)$ is the transverse magnetization at time t. The behavior of T_2 is also related to a spectral density so that (Gadian. 1995):

$$\frac{1}{T_2} \propto B_z \tau_c^2, \tag{12}$$

where B_{z} is the magnitude of the fluctuating field in z-direction. As would be expected, transverse or T_2 decay is fastest when the molecules are immobile, i.e. $\tau_{\mathrm{c}} \to 0$, although in that case, Bloembergen-Purcell-Pound-theory is no longer valid and the signal decay becomes non-exponential.

In addition to dephasing of the signal due to molecular tumbling, static field inhomogeneities with sources beyond the molecular scale add to the transverse decay. They can originate from different sources e.g. varying magnetic susceptibility of different tissue components (Nishimura. 2010), metallic implants, tissue/air interfaces as well sources outside the sample. These also induce a spectrum of slightly differing resonance frequencies, leading to destructive interference in the signal. These effects are usually described with an additional exponential decay constant T_2' and the inverse of the overall transverse decay constant is written as:

$$\frac{1}{T_2^*} = \frac{1}{T_2} + \frac{1}{T_2'}. \tag{13}$$

Usually, it is thought that static T_2' effects can be refocused in a so-called spin-echo (SE) experiment (Hahn 1950). In its most common form, after exciting the signal, a 180° flip angle RF pulse is applied. After excitation, transverse magnetization in slightly different magnetic fields accumulates phase differences. When the 180° pulse is applied on the xy-plane, the magnetization revolves around it to the other side of the xy-plane, reversing the sign of the phases. As the directions of phase accumulation remain the same, the magnetization will momentarily be refocused. This time is called the echo time (TE) and it is also seen as the the time delay between excitation and acquisition. The idea that T_2' effects can be refocused and T_2 cannot is naturally a simplification: e.g. the 180° pulse can be repeated, and depending on the delay between the pulses, interactions with different time scales can be refocused. In addition, the pulses need not be exactly at 180° in order to refocus signal, and often are not due to imperfections in the B_0 and $\boldsymbol{B}_1$ field.

2.2.3 Magnetization transfer

Magnetization transfer (MT) refers to the exchange of magnetization between molecules through different mechanisms. Usually, MT is described as occurring between the so-called free water pool and the bound pool that consists of bound water and macromolecules that are both slowly tumbling (Henkelman et al. 2001). It is also possible to include chemical exchange between two mobile pools in MT, such as the exchange between mobile water and metabolites. In chemical exchange, there is a chemical exchange reaction between the pools where hydrogen is constantly exchanged. Usually this type of MT between two mobile pools is referred to as the chemical exchange saturation transfer (CEST) (van Zijl & Yadav 2011), although chemical exchange exists also between mobile and bound pools.

The macromolecular pool is highly immobile, containing a large spectrum of resonance frequencies. Hence the transverse signal decay is very fast in the macromolecular pool. In a typical MT experiment, an RF pulse is applied off-resonance, usually 2 to 10 kHz, mainly

exciting the hydrogen of the macromolecules. Almost immediately, they become saturated due to the fast transverse decay and cannot produce a signal until there is adequate T_1 relaxation. At the same time, the free pool is continuously exchanging magnetization with the saturated macromolecular pool through chemical exchange and dipolar interactions. Both of the former processes are known to contribute to MT, although the dipolar interaction is more important (Eng et al. 1991). After the exchange, the saturated magnetization reduces the potential signal that could be induced in the free pool, and given that a normal MRI experiment follows the saturating RF pulse, the image intensity will be weighted by how much saturated magnetization has been exchanged to and remains in the free water pool. This weighting depends not only on the macromolecular content of the tissue, but also on a variety of other factors, such as the exchange rate between the pools, T_1 of the free pool and all of the parameters of the saturating RF pulse and the pulse sequence used to make the image.

The MT experiment can be done with a single continuous RF pulse that can be seconds in length. Often, this is not feasible due to hardware limitations and due to safety limitations on how much RF energy can be deposited into the tissue. An MT experiment can also be conducted by replacing the continuous pulse with a train of shorter pulses that can solve both limitations, or alternatively the saturation and imaging cycle can be repeated relatively often with a shorter saturation pulse (Graham & Henkelman 1997, Sled & Pike 2000).

Usually, the simplest MT experiment involves taking an image with and without the saturation pulse. From these images, usually the semi-quantitative measure, magnetization transfer ratio (MTR), is calculated:

$$MTR = \frac{M_0 - M_{sat}}{M_0}, \tag{14}$$

where M_0 is the measured signal without the MT saturation pulse and M_{sat} signal with the MT saturation. If the measurement is repeated with a long time of repetition (TR) allowing full T_1 relaxation, and a 90° pulse is used for excitation, M_0 represents the z-magnetization in thermal equilibrium. Otherwise, it is the z-magnetization in a steady state without full T_1 relaxation just before excitation. MTR is semi-quantitative since it is likewise affected by the experimental parameters and all the physical parameters of the MT phenomenon such as T_1, rate of exchange and macromolecular concentration are included together although they cannot be individually separated into the ratio. In more complex experiments, multiple off-resonances and multiple amplitudes for the saturation pulses are used and the data can be fitted into several different models (Sled & Pike 2001, Ceckler et al. 2001). This can make it possible to obtain different parameters e.g. the ratio of the free and bound pools with better accuracy, although at the same time, it will increase the experimental time.

2.3 IMAGE FORMATION

This section outlines the basics of forming an MRI image in general, how SWIFT and similar sequences work and how they differ from conventional MRI pulse sequences.

2.3.1 Signal equation

Almost all spatial localization in MRI is based on a linear combination of three orthogonal magnetic gradient fields in xyz-directions:

$$G_x(t) = \frac{dB_z(t)}{dx}, G_y(t) = \frac{dB_z(t)}{dy} \text{ and } G_z(t) = \frac{dB_z(t)}{dz}. \tag{15}$$

Thus the gradient coils are designed to produce a changing z-component of the magnetic field that varies linearly along a specified direction. The value at the scanner isocenter is designed to be zero. The effect of adding a gradient is to make the Larmor frequency spatially dependent:

$$\omega_0(\boldsymbol{r},t) = \gamma(B_0 + \boldsymbol{G}(t)\cdot\boldsymbol{r}), \tag{16}$$

where $\boldsymbol{r}$ is the spatial coordinate (x,y,z) and $\boldsymbol{G}(t)$ is the gradient vector. Hence, after RF excitation with the gradients on, the time varying magnetization can be written:

$$M(\boldsymbol{r},t) = M_0(\boldsymbol{r})e^{-\frac{t}{T_2}}e^{-i\omega_0 t}e^{-i\gamma\boldsymbol{G}(t)\cdot\boldsymbol{r}t}. \tag{17}$$

The exponential term $e^{-i\omega_0 t}$ for the effect of the Larmor frequency can be omitted since it is demodulated from the received signal. For simplicity, relaxation effects can also be ignored. Integrating over all excited locations in the sample, the total signal can be written (Nishimura. 2010):

$$s(t) = \iiint M_0(\boldsymbol{r})e^{-i2\pi[k_x(t)x+k_y(t)y+k_z(t)z]}dx\,dy\,dz, \tag{18}$$

where

$$k_x(t) = \frac{\gamma}{2\pi}\int_0^t G_x(\tau)d\tau,\ k_y(t) = \frac{\gamma}{2\pi}\int_0^t G_y(\tau)d\tau \text{ and } k_z(t) = \frac{\gamma}{2\pi}\int_0^t G_z(\tau)d\tau. \tag{19}$$

Eq. (18) is the signal equation for MRI assuming uniform excitation and reception. It shows how time evolution in the presence of the gradients traces the FT of the magnetization distribution $M_0(\mathbf{r})$ along the path $\boldsymbol{k}(\mathrm{t})$ with the parametric coordinates described by Eq. (19). If one wishes to solve the distribution and obtain an image, in principle, one needs only to arrange the values of $s(t)$ for each $\boldsymbol{k}$ position and then perform an inverse FT (IFT) of the collected data. For historical reasons, the variable *k* is used to describe the coordinates in the Fourier space and the data collected in MRI is called k-space.

2.3.2 K-space trajectories and reconstruction

K-space can be sampled with almost arbitrary trajectories by modulating the gradients according to Eq. (19). The majority of MRI uses a Cartesian trajectory where the k-space is sampled line by line, with each sampled point falling onto a Cartesian grid. This is achieved with so-called phase encoding and frequency encoding gradients: phase encoding chooses the line coordinate and frequency encoding acquires a line through the k-space. Cartesian imaging became popular due to the simplicity of analysis and ease of reconstructing the image with a simple IFT, although some pre-processing may still be required (Buonocore & Gao 1997).

The very first MRI images were not acquired in a Cartesian manner (Lauterbur 1973), and alternative trajectories have started to come back, due to advances in hardware and post-processing techniques. By using a radial trajectory, the measurement point in k-space moves in a straight line through the center k-space or starting from the center of k-space to the edge of k-space (center out). Radial trajectories typically sample a disc shaped k-space in 2D and a sphere in 3D.

The reconstruction of non-Cartesian data requires additional steps or different algorithms in comparison to Cartesian data. For radial imaging, this can be achieved with filtered back projection as in nuclear tomographic methods. Another option is the so-called regridding method (Beatty et al. 2005) e.g. the approach that SWIFT uses, although it can also be used for other non-Cartesian methods. Regridding interpolates and resamples non-Cartesian data by applying a convolution kernel $C(k_\mathrm{x},k_\mathrm{y})$ to the acquired data and evaluating the convolution at the Cartesian grid points:

$$\widehat{M}(k_x,k_y) = \left[\left(M(k_x,k_y)S(k_x,k_y)\right) * C(k_x,k_y)\right]III\left(\frac{k_x}{\Delta k_x},\frac{k_y}{\Delta k_y}\right), \tag{20}$$

where $M(k_\mathrm{x},k_\mathrm{y})$ is the magnetization of the object, $S(k_\mathrm{x},k_\mathrm{y})$ is the radial sampling function, $III(\cdot)$ is the Cartesian sampling function and $\Delta k_{\mathrm{x,y}}$ is the resolution in k-space. The term $\mathrm{M}(\mathrm{k_x},\mathrm{k_y})\mathrm{S}(\mathrm{k_x},\mathrm{k_y})$ represents the collected data. After IFT, Eq. (20) becomes:

$$\hat{m}(x,y) = \left[\left(m(x,y) * s(x,y)\right)c(x,y)\right] III\left(\frac{x}{FOV_x}, \frac{y}{FOV_y}\right), \quad (21)$$

where $FOV_{x,y}$ is the field of view in image space in the x and y-directions. There are a number of design problems in the regridding process. For example, an ideal convolution kernel would be an infinite sinc-function, in which IFT would be a rectangle or a cube. However, this is not possible in practice and hence a windowed sinc or some other type of window has to be used (Jackson et al. 1991). Furthermore, from Eq. (21) it can be seen that the image is multiplied by the IFT of the convolution kernel. Hence, due to the finite convolution kernel, intensity variations in the final image are possible. In addition, when using the radial k-space trajectory, the sample density is variable, being the highest at the center. This also needs to be taken into account or otherwise the image can display severe artefacts (Johnson & Pipe 2009).
Excellent solutions to these kinds of issues have been found, and with the computational power available today, radial and other non-Cartesian sampling can be used routinely. Radial methods offer benefits over Cartesian imaging, e.g. high robustness for motion since the center of k-space is sampled multiple times and flexibility is achieved about how long k-space needs to be acquired for a single image and how the acquired data is divided for dynamic studies (Rasche et al. 1995, Lin et al. 2008). However, Cartesian imaging continues to be more popular in MRI, due to its ease of use and well known theory.

2.4 SHORT ECHO TIME IMAGING

This section will briefly describe pulse sequences that enable imaging with a very short TE to detect signals with a short T_2^*, especially SWIFT. One class of short TE pulse sequences not reviewed here but that should be mentioned, are the single point imaging methods (Balcom et al. 1996), where each excitation is followed by acquisition of only a single point in k-space. However, these methods are not practical for *in vivo* imaging as they are very slow and involve large amounts of RF energy deposition into the sample.

2.4.1 Gradient recalled echo

Gradient recalled echo (GRE) (Haase et al. 1986) is one the most basic MRI pulse sequences. GRE only consists of an excitation RF pulse followed by spatial encoding and is thus sensitive to T_2^* instead of T_2. The TE is defined as the time from the center of the RF pulse to the center of acquisition as shown in Figure 1, or in other words, to the point of crossing the center of k-space. The first frequency encoding the gradient lobe moves the measurement point to the edge of the k-space before the actual acquisition. Usually, after each acquisition, a so-called spoiler gradient is applied to strongly dephase the transverse magnetization, effectively only leaving

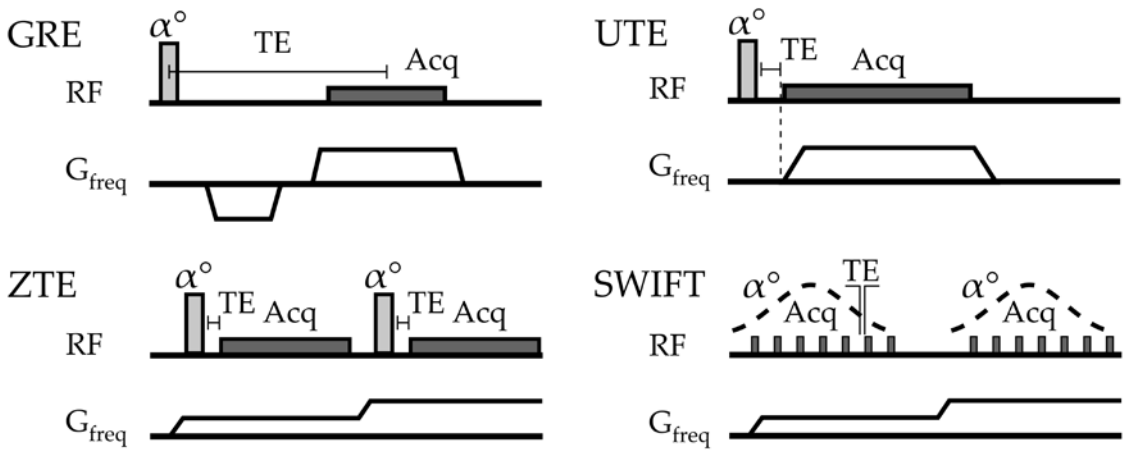

Figure 1 MRI pulse sequences capable of imaging short T_2^* components.

longitudinal magnetization for the next TR. The term spoiled GRE can be used for accuracy, but usually spoiling is assumed in the GRE pulse sequence. GRE is mostly used in a Cartesian manner but is also possible to apply non-Cartesian k-space trajectories.
The signal of GRE is described by the Ernst equation (Ernst & Anderson 1966):

$$M_{xy}(t) = M_0 \frac{1 - e^{-TR/T_1}}{1 - e^{-TR/T_1}\cos\alpha} e^{-TE/T_2^*} \sin\alpha, \quad (22)$$

where α is the flip angle and M_0 is the longitudinal magnetization in thermal equilibrium. The flip angle giving the maximum signal with a certain T_1 is called the Ernst angle for that T_1. The image contrast can be weighted differently by changing the parameters: short TE, short TR and high flip angle lead to T_1 weighting; long TE, long TR and small flip angle lead to T_2^* weighting; short TE, long TR and low flip angle lead to so-called proton density weighting. Typical parameters for GRE are in the order of TE = 2 ms to 25 ms, TR = 50 ms to 500 ms and α = 5° - 60°. Shorter TEs can be achieved with high performing gradients e.g. in small animal scanners, though this often means sacrificing resolution and signal-to-noise ratio.

2.4.2 Ultra-short echo time

Ultra-short echo time (UTE) enables detecting very short T_2^* components. As shown in Figure 1, the magnetization is excited by an RF pulse followed by rapid ramping of the frequency encoding gradient (Robson et al. 2003, Tyler et al. 2007). The signature property of UTE is that the acquisition starts immediately with the ramping of the gradient. This means that UTE is inherently a center-out radial sequence. In addition, since the amplitude of the frequency encoding gradient is increasing during the acquisition, the sampling rate of k-space is accelerating until the gradient reaches a plateau. Even though UTE does not involve a gradient echo or a spin-echo, the term TE is still used to describe the delay between excitation and beginning of acquisition that for center-out radial sequences is at the center of k-space. The term acquisition delay has been suggested for use in relation to SWIFT (Zhou et al. 2010).

UTE can be used for 2D slice imaging (Pauly et al. 1989a) or for 3D imaging (Glover et al. 1992). In 2D imaging, half-sinc or half-Gauss pulses are used for excitation in combination of a slice encoding gradient (Pauly et al. 1989a). In this case, two acquisitions are needed for the intended slice profile with reversed slice selection gradients, since the excitation profile of a single pulse is asymmetric and outside the intended slice. The benefit of the half-sinc/Gauss pulse is that it removes the need for the gradient lobe for compensating intra-slice dephasing effects during excitation using normal RF pulses (Bernstein et al. 2004). The behavior of these pulses can be interpreted as ending the pulse at the center of the so-called excitation k-space (Pauly et al. 1989b). In 3D UTE imaging, a non-selective short hard pulse is used, followed by the frequency encoding gradient (Glover et al. 1992).

Conventionally, T_2^* decay is assumed to be negligible during the RF pulses ($T_2^* \gg T_p$, where T_p is the pulse length), in which case, a good approximation of TE can be calculated from the center of the excitation RF pulse for symmetric RF pulses (Bernstein et al. 2004). However, when the transverse decay is in the range of the pulse length or shorter ($T_2^* < T_p$), TE effectively becomes T_2^* dependent, and when $T_2^* \to 0$, TE can be calculated from the end of the pulse (Carl et al. 2010). In general, with long T_2^*, UTE follows the Ernst equation [Eq. (22)]. However for short T_2^* components, the equation needs to be generalized to take into account the signal decay during the RF pulse (Carl et al. 2010).

An additional effect related to short T_2^* is associated with the length of the acquisition time, T_{acq}. If $T_2^* \gg T_{\mathrm{acq}}$, effectively no signal decay happens during the acquisition. However, if $T_2^* \sim T_{\mathrm{acq}}$, image magnitude is affected by the T_2^* decay since the magnitude is proportional to the integral over k-space. The T_2^* decay can also be seen as a low pass filter for the k-space. Given that $T_2^* \ll T_{\mathrm{acq}}$, the image will suffer from significant blurring (Rahmer et al. 2006). The blurring effect can be compensated by decreasing the acquisition time, or in other words, increasing the acquisition bandwidth or spectral width (SW). An optimal T_{acq} has been suggested to be 0.69 T_2^*

for UTE giving a compromise between image sharpness and SNR (Rahmer et al. 2006). Due to slower k-space sampling during ramping of the frequency encoding gradient, UTE may be more susceptible to a T_2^* decay than zero echo time (ZTE) or SWIFT pulse sequences, since relatively speaking, there is a greater effect at the center of the k-space.

UTE has found many applications mainly in the musculoskeletal MRI including bone, tendon and cartilage (Du et al. 2011b), and also in lungs (Takahashi et al. 2010). It has also been shown that myelinated nerve fibers have short T_2^* components that are possible to detect: a relatively short T_2^* signal is related to so-called myelin water that is trapped between the myelin sheaths (Mackay et al. 1994), and a very short T_2^* signal that has been related to the myelin lipids themselves (Horch et al. 2011). The problem of direct myelin imaging is the suppression of the long T_2^* components that clearly make up the majority of the signal. In UTE, the myelin signal weighted imaging has been sought by using a combination of subtracting two images with different TEs and a long adiabatic inversion pulse (Wilhelm et al. 2012, Du et al. 2014, Garwood & Delabarre 2001). The inversion pulse is set so that long T_2^* components of either gray matter (GM) or white matter (WM) are nulled based on T_1 at excitation (Nishimura. 2010) and either WM or WM has a small residual signal. The long T_2^* residual signal will not decay significantly between the echoes and it will be suppressed by the subtraction. The short T_2^* component, however, does not experience any inversion due to transverse decay during the pulse (Larson et al. 2006, Larson et al. 2007): they give a signal in the first echo but not in the second echo. Hence, after subtraction, only the short T_2^* signal of the first echo related to myelin is left.

2.4.3 Zero echo time

ZTE (Weiger et al. 2011), also known as the back-projection low angle shot (Hafner 1994) or projection imaging (Kuethe et al. 2007), is another pulse sequence with minimized TE. As shown in Figure 1, the excitation RF pulse is applied when the frequency encoding gradient is already on followed by acquisition. TE is defined as the delay between the RF pulse and the beginning of the acquisition. ZTE is inherently a 3D pulse sequence, since the frequency encoding gradient is on during excitation. ZTE uses very short hard RF pulses i.e. down to 1 μs (Weiger et al. 2013b) for excitation. These short pulses enable broadband excitation enforced by the frequency encoding gradient. However, in order to excite the magnetization, these short pulses need to be high powered, leading to small flip angles due peak power limitations (Weiger et al. 2011). By using the hard pulse with the frequency encoding gradient on, the encoding of the k-space starts already during the pulse. Additionally, there is a delay at the beginning of acquisition due to hardware switching from the transmit mode to the receive mode and due to the group delay of digital filters. Hence, the acquisition does not start at the center of the k-space, which needs to be taken into account in the reconstruction (Weiger et al. 2010) or by acquiring the center of k-space by applying single point imaging (Grodzki et al. 2012). Regardless of these issues, ZTE permits slightly better detection of short T_2^* components than UTE, since the gradient does not need to be ramped (Weiger et al. 2012) leading to less T_2^* decay at the center of k-space. On the other hand, in UTE, TE is a parameter that can be adjusted to obtain different T_2^* weightings enabling relatively simple T_2^* mapping.

As UTE, ZTE has found its main usage in musculoskeletal MRI (Weiger et al. 2013b, Weiger et al. 2013a). T_1 weighted brain imaging has also been demonstrated (Weiger et al. 2014, Weiger et al. 2013a), and imaging with long T_2^* suppression but not in brain (Weiger et al. 2015).

2.4.4 Sweep imaging with Fourier transform

SWIFT has also been designed for the detection of very short T_2^* components. SWIFT takes a unique approach by adding gaps to hyperbolic secant (HS) pulses (Garwood & Delabarre 2001) and acquiring inside these gaps (Idiyatullin et al. 2006), as shown in Figure 1. HS pulses are used in SWIFT since the broad bandwidths needed for excitation during the frequency encoding gradient can be achieved with the relatively long pulse lengths that are needed for the

gapping to be feasible. In SWIFT, the excitation bandwidth needs to match the acquisition bandwidth that usually ranges from 31 kHz to 125 kHz.

Usually HS pulses are used for inversion in the adiabatic region where the initially z-directional magnetization is forced to follow the effective field $\boldsymbol{B}_{eff}$ towards the -z-direction. Adiabatic pulses fulfill the so called adiabatic condition (Garwood & Delabarre 2001):

$$\left|\frac{d\alpha}{dt}\right| \ll \gamma|\boldsymbol{B}_{eff}|, \tag{23}$$

where α is the angle between the effective field and z-axis. For example, unlike UTE and ZTE that use only amplitude modulated pulses, HS pulses are both amplitude and frequency modulated pulses, making possible the modulation of the amplitude and angle α of the effective field $\boldsymbol{B}_{eff}$ in the rotating frame of reference. One benefit of HS pulses is their insensitivity to $\boldsymbol{B}_1$ inhomogeneities and also to B_0 inhomogeneities, given that the pulse is driven at high enough power.

In SWIFT, the HS pulses are driven at low power in the sub-adiabatic, the so-called "linear, rapid passage" region. Rapid passage means that the rate of the frequency sweep of the pulse is much faster than the transverse decay of the signal. The linear region means that the pulse power is much lower than that needed for an adiabatic pulse; the flip angle is well below 180° and it is linearly proportional to the pulse power.

The addition of gaps in the HS pulse does not significantly change the behavior of the pulse; in essence, only the pulse peak power needs to be increased, the more so the longer the gaps are. The gap length varies from a few μs to tens of μs, depending on the pulse duty cycle and bandwidth. In the sense of transverse decay, these gaps are very short and there is almost no time for signal loss.

Table 1. The benefits and disadvantages of the three main ultrashort TE pulse sequences.

	Pros	**Cons**
UTE	+2D possible, enables short scan times +Can adjust initial TE +Can collect secondary echoes +No flip angle restrictions	-Some blur from T_2^* decay possible because of gradient ramping -2D requires two acquisitions per k-space spoke -Noisy
ZTE	+Shortest possible TE +Simple RF pulses +Acquisition bandwidth restricted only by maximum gradient amplitude +Silent +Broad excitation BW	-Inherently 3D -Peak power restricts flip angle -Acquiring the center of k-space can be problematic
SWIFT	+Shortest possible TE +Higher flip angles possible compared to ZTE +Silent +Broad excitation BW	-Inherently 3D -Acquisition bandwidth restricted by RF switching -Use of gapped HS pulses adds to the complexity of post-processing

Since HS pulses are frequency swept, i.e. the excitation frequency of the pulse changes with time, in SWIFT, different isochromates will be excited at different times. This means that the raw acquired SWIFT signal contains FIDs in different points of the transverse decay and also with differing phases due to the varying phase of the HS pulse. Since SWIFT is used with small flip angles, the so-called small flip angle approximation (Nishimura. 2010) can be applied. Hence, according to the theory of linear systems, the response $r(t)$ of the magnetization to the RF pulse can be written (Idiyatullin et al. 2006):

$$r(t) = h(t) * x(t), \tag{24}$$

where $h(t)$ is impulse response or the desired rephased FID and $x(t)$ is the RF pulse. From here, $h(t)$ could be solved by using deconvolution, but the solution can be achieved much easier in the transform domain. By carrying out the Fourier transform and applying the convolution theorem, we obtain:

$$H(\omega) = \frac{R(\omega)X^*(\omega)}{|X(\omega)|^2}, \tag{25}$$

where H(ω), R(ω) and X(ω) are the FTs of the FID, raw signal and the RF pulse, respectively. This process is repeated for all the acquired signals; they are Fourier transformed back into k-space and finally reconstructed with the regridding method. It should be noted that there are additional complexities to post-processing of the SWIFT data originating from the gapping of the RF pulse, but also effectively gapping the acquisition (Corum et al. 2015).

Applications of SWIFT have so far been similar to UTE and ZTE: musculoskeletal imaging (Idiyatullin et al. 2011, Luhach et al. 2014, Kendi et al. 2011, Nissi et al. 2014, Rautiainen et al. 2013), although there has also been imaging of lungs (Kobayashi et al. 2014), breast (Corum et al. 2014), cardiac tissue(Zhou et al. 2010) and detection of nanoparticles (Wang et al. 2013, Zhang et al. 2014). Almost all of the work where SWIFT has been exploited in brain imaging is presented in this thesis.

In comparison to UTE, SWIFT has many benefits. The broadband excitation pulses used by SWIFT make it possible to excite even very off-resonance isochromates, e.g. when there are large susceptibility differences due to metallic implants. The broadband excitation is spatially dependent: the center of the FOV always experiences the bandwidth [-BW/2 BW/2] since there the off-resonance due to the frequency encoding gradient is zero. On the other hand, the location at the edge of the FOV experiences bandwidths between [0 ±BW] and [-BW/2 BW/2], when the frequency encoding gradient is parallel or perpendicular to the location, respectively. There are also other benefits including better short T_2^* sensitivity since there is no gradient ramping, and for the same reason there is much less chance for misplacing data points in k-space due to gradient inaccuracies. From the view of patient comfort, it is very beneficial that SWIFT can be made virtually silent. This applies also to ZTE. In both pulse sequences, the readout gradient does not need to be zeroed between acquisitions and can be gently adjusted for the next acquisition.

There are some downsides of SWIFT in comparison to UTE e.g. not being able to adjust TE and not being able to image 2D slices. The former would enable T_2^* weighting and mapping even with short T_2^* components and the latter would be beneficial if very short scan times are needed. Both of these drawbacks also apply to ZTE. It is in theory possible to collect echoes with SWIFT after the initial RF modulated FID. HS pulses have been utilized for GRE and SE type of imaging before (Park et al. 2006, Park et al. 2011, Park & Garwood 2009). In addition, although SWIFT is easier for the gradient hardware than UTE, it is more demanding on the RF transmit-receive chain due to the fast switching between excitation and acquisition.

SWIFT and ZTE are approximately equally capable of detecting short T_2^* components since their TE is very similar and dependent on the same hardware issues. However, the greatest downside of SWIFT is that the SW is limited by the switching speed of the RF hardware. This is a disadvantage when imaging very short T_2^* components, since significant blurring will be seen when $T_2^* \ll T_{acq}$ as explained before for UTE. In practical terms, the upper SW limit of SWIFT is around 125 kHz. However, recently a modification to the original gapped SWIFT, exploiting the excitation sidebands induced by the gapping (Idiyatullin et al. 2008), was introduced, enabling SWs of several hundreds of kHz (Idiyatullin et al. 2015). The benefits of SWIFT over ZTE are its much lower peak RF power that makes feasible relatively high flip angles, and there is no ambiguity at the center of k-space.

In conclusion, each of these sequences has their pros and cons (Table 1). Similar results can be achieved with all of them, and if one can choose, the sequence should be selected so that it is optimal for the particular application. In the case of brain imaging, if short T_2^* contrast or mapping is desired, UTE may be the sequence of choice at this time since this contrast has

already been demonstrated. In terms of T_1 weighting and for detecting virtually all short T_2^* components, SWIFT may be a better choice since higher flip angles can be achieved than with ZTE.

2.5 PHASE AND FREQUENCY IMAGING

The majority of MRI is concentrated on the magnitude of the signal. However, due to B_0 inhomogeneities of a different spatial scale, and due to different kinds of motion of excited magnetization during gradients applied in the pulse sequences, transverse magnetization will gain phase differences during the pulse sequence making MRI image complex valued. There are several sources of motion i.e. movement of the patient, physiological motion and flow of blood and cerebrospinal fluid. Motion during gradients will lead to unintended changes in phase, since the moving nuclei will experience different magnetic fields and thus the magnetization will rotate at different Larmor frequencies than intended. This can be exploited e.g. when measuring blood flow and in angiography (Bernstein et al. 2004). There are also other mechanisms that can affect the phase, e.g. phase of the $\boldsymbol{B}_1$ field, but these are usually not of interest.

The main focus of this thesis was the static field inhomogeneities in the brain induced by brain calcifications and brain tissue. The effects of static inhomogeneities are refocused by SE pulse sequences, and hence the majority of phase or frequency contrast imaging has been based on GRE. If one examines the GRE signal from magnetization in a single location (x, y) (gradients excluded for simplicity):

$$M(x, y, t) = M_{ss}(x, y)e^{-i2\pi\Delta f t} = M_{ss}(x, y)e^{-i2\pi\Delta f(t-TE)}e^{-i2\pi\Delta f TE}, \tag{26}$$

where $M_{\mathrm{ss}}(x, y)$ is the steady state magnetization according to Eq. (22) and Δf is the off-resonance deviation from B_0 in Hertz. From here, one can see that after IFT of the GRE signal, the last exponential constant term will remain as it is. Hence, in GRE, the phase in image space is directly proportional to the off-resonance and TE

$$\phi_{GRE} = 2\pi\Delta f TE. \tag{27}$$

Further, it is now possible to discern that the field inhomogeneity can be solved from Eq. (27) to create a frequency map. Usually, however, it is solved by using at least two different TEs to remove constant offsets in the phase due other phase sources (Schweser et al. 2011).

Although phase or frequency mapping with GRE is very simple in principle, difficulties arise in the post-processing. Since the phase is confined into the range $[-\pi\ \pi]$, full revolution of the magnetization in the rotating frame of reference due to being off-resonance will wrap into this range. Hence it is not trivial to assess the total accumulated phase. In the raw phase image, wrapping can be seen as sharp boundaries where the phase jumps from maximum to minimum or vice versa. In addition, the effect of large scale field deviations due to imperfect shimming are added into the phase of interest and these need to be removed. The simplest way of removing the phase wraps and the unwanted phase contributions is the so-called homodyne filtering (Noll et al. 1991) which involves a complex division of the original image with a low-pass filtered version of the image:

$$\rho'(x, y) = \frac{\rho_{orig}(x, y)}{\rho_{lp}(x, y)}, \tag{28}$$

where $\rho_{\mathrm{orig}}(\mathrm{x}, \mathrm{y})$ is the original image and $\rho_{\mathrm{lp}}(\mathrm{x}, \mathrm{y})$ is the low-pass filtered image. The complex division acts as a high-pass filter for the phase image. Homodyne filtering is very simple and easy, but it tends to also remove the wanted phase contrast when more and more filtering is needed due to stronger large scale B_0 field fluctuations. There are more sophisticated post-

processing methods, where phase unwrapping and the removal of unwanted phase are separated (Schweser et al. 2011).

Phase or frequency mapping has also been conducted with a few other methods, including water saturation shift referencing (WASSR) (Lim et al. 2014), steady state free precession SSFP (Lee et al. 2011a) and UTE (Carl & Chiang 2012). WASSR is a method that uses direct saturation of water to probe where the signal is maximally attenuated, which is also where the true resonance frequency should be located. WASSR enables frequency mapping without phase wrapping, but also requires more RF energy deposition into the patient than required with other approaches e.g. GRE. SSFP is a high SNR pulse sequence with a strong sensitivity to B_0 inhomogeneities. This sensitivity makes it rather prone to artefacts but it can also be exploited for achieving a phase contrast with a high contrast-to-noise ratio (CNR). However, there is a small dynamic range for off-resonances not leading to artefacts. UTE has been used for phase imaging of meniscus (see section 3.2.3). As shown in this thesis for SWIFT, similarly as with UTE, there is almost no phase accumulation at the center of k-space, but phase does still accumulate during acquisition.

Susceptibility weighted imaging (SWI) is a GRE phase based method that mixes information from both magnitude and phase (Haacke et al. 2004, Haacke et al. 2009). In SWI, the phase is first unwrapped e.g. by using homodyne filtering (Haacke et al. 2009). Next, a phase mask is created so that the more negative the phase, the lower is the mask value. Finally, the magnitude image is multiplied with this mask. The mask can also be made more sophisticated so that the negative and positive phases have differing mask values. The resulting image will highlight relatively strong areas of magnetic field differences, e.g. hemorrhages and veins (Mittal et al. 2009).

QSM is another MRI method that is based on the phase contrast of GRE. As noted previously, frequency shift maps can be calculated from Eq. (27) based on multiple different TEs or a multi-echo acquisition using GRE. It has been shown that the field induced by the magnetic susceptibility of the tissue can be approximately written as the convolution of the tissue susceptibility map and a unit dipole (Salomir et al. 2003, Marques & Bowtell 2005). In principle, this enables a fast solution of the susceptibility map using the convolution theorem (Haacke et al. 2005, Shmueli et al. 2009). One of the limitations encountered in QSM has been how to can handle streaking artefacts, this being due to the ill-conditioned inversion problem of solving the susceptibility. There are at least some partial solutions to this problem (Shmueli et al. 2009, Schweser et al. 2011) and QSM is a now a very promising technique.

2.6 DIFFUSION TENSOR IMAGING

Diffusion weighted imaging (DWI) is an MRI technique where the image contrast is related to the diffusion of water in different environments (Le Bihan et al. 1986, Jones. 2010). This is possible by using a pair of gradients so that the second gradient compensates for the dephasing effects of the first gradient. Given that water with excited magnetization diffuses equally in all directions, i.e. in an isotropic manner, the diffusion gradient pair will attenuate the signal equally regardless of the direction of the gradient vector. However, if the diffusion occurs preferentially in some direction, i.e. it is anisotropic, a stronger signal attenuation will be seen the closer the gradient vector is to this preferential direction. The amount of signal decay depends on how strong the diffusion is in the diffusion gradient direction, the gradient amplitude and the gradient lobe length δ, and on the time separation of the gradient lobes, also known as diffusion time Δ. This signal attenuation using rectangular gradient lobes can be described by the Stejskal-Tanner equation (Stejskal & Tanner 1965):

$$A = e^{-\gamma^2 G^2 D \delta^2 (\Delta - \frac{\delta}{3})}, \tag{29}$$

where G is the gradient amplitude and D is the fluid diffusion coefficient that depends on the temperature, the viscosity of the fluid and the size of the particle according to the Einstein-Stokes relation. In practice, all the gradients and their exact shapes in the pulse sequence need to be taken into account if one wishes to accurately calculate the diffusion weighting. The signal attenuation can further be written:

$$A = e^{-bD}, \tag{30}$$

where b is the so-called b-factor or the b-value containing all the gradients of the pulse sequence (Le Bihan et al. 1986). The b-value is used to describe the amount of diffusion weighting of the pulse sequence. Typical values vary from hundreds of s/mm^2 in clinical scanners to thousands in experimental animal scanners.

A single DWI image only displays the effect of diffusion in one direction. However, brain tissue, in fact tissue in general, has a complicated 3D dimensional architecture. Diffusion tensor imaging (DTI) is an extension of DWI where the interest is focused on diffusion in three dimensions (Jones. 2010). This enables fuller description of diffusion in tissue and thus also gives more information about the tissue structure. In this case, b-value and diffusion coefficient are written in matrix form and the signal attenuation becomes

$$A(\boldsymbol{b}) = A(\boldsymbol{b} = \boldsymbol{0})\exp\left(-\Sigma_{i=1,2,3}\Sigma_{j=1,2,3} b_{ij} D_{ij}\right). \tag{31}$$

$\boldsymbol{D}$ is also known as the diffusion tensor and it arises from an assumption of a 3D Gaussian displacement distribution for the water molecules (Jones. 2010). The diffusion tensor can be solved from Eq. (31) by collecting images with at least six different diffusion gradient directions and one without diffusion weighting. Often more gradient directions are used if one wishes a more robust estimation (Jones 2004).

The 3D diffusion can be described by the eigenvalues $\lambda_{1,2,3}$ of the diffusion tensor where each of them describes the diffusivity in their respective orthogonal directions. Usually, the direction with the largest eigenvalue is called the principal diffusion direction and the eigenvalue itself is called the longitudinal or axial diffusivity (AD), $\lambda_{||}$. The average of the two smaller eigenvalues is called radial diffusivity (RD), $\lambda_{\perp}$. The diffusion tensor can be described by an ellipsoid where the eigenvectors define the orientation and the eigenvalues define the length of each dimension of the ellipsoid. One of the most common ways of describing the shape of the ellipsoid, or the anisotropy of the diffusion, is the so-called fractional anisotropy (FA) (Basser & Pierpaoli 1996):

$$FA = \sqrt{3/2}\frac{\sqrt{(\lambda_1 - \lambda_{mean})^2 + (\lambda_2 - \lambda_{mean})^2 + (\lambda_3 - \lambda_{mean})^2}}{\sqrt{\lambda_1^2 + \lambda_2^2 + \lambda_3^2}}, \tag{32}$$

where λ_{mean} is the mean of the eigenvalues. FA is the standard deviation of the eigenvalues or diffusivities normalized to [0 1], and it does not contain information about the orientation of the ellipsoid. If FA = 0, the ellipsoid becomes a sphere and the diffusion is isotropic. If FA = 1, diffusion would be completely parallel in one direction. In tissue, these extremes are never achieved, however, very clear differences can be seen. WM largely consists of myelinated axons that can be very organized directionally, leading to higher FA values. On the other hand, GM has much less myelinated axons and is often more homogeneous, giving low FA values. For example, in human WM, FA has been shown to be around 0.5-0.9 (Kochunov et al. 2015) and in GM <0.3 (Seehaus et al. 2015).

3 *Imaging calcifications and brain structures*

This section covers the literature more specific to studies **I**-**III**.

3.1 DETECTING CALCIFICATIONS AFTER BRAIN INSULTS

3.1.1 Calcifications in different brain diseases

A relatively common finding in brain diseases is a calcification. They can be found in many diseases including infections (Caldemeyer et al. 1997), tumors (Okuchi et al. 1992), epilepsy (Arnold & Kreel 1991), infarction (Parisi et al. 1988), head trauma (Cervós-Navarro & Lafuente 1991), hypoxic brain tissue (Ansari et al. 1990), Alzheimer's disease (Friedland et al. 1990) and Parkinson's disease (Vermersch et al. 1992). The formation of calcifications, or precipitation of calcium, has also been observed in many animal models of these diseases such as cerebral ischemia (Mäkinen et al. 2007), TBI (Osteen et al. 2001), and in animal models of epilepsy using pilocarpine or kainic acid (Gayoso et al. 2003, Lafreniere et al. 1992). Calcifications have been seen to form as early as three days after ischemia (Shirotani et al. 1994, Watanabe et al. 1998) or five days after systemic kainic acid injection (Gayoso et al. 2003). Often, calcifications are detected in chronic time point of the disease progression, several months after TBI (Pierce et al. 1998) or brain ischemic insult (Mäkinen et al. 2007). Calcifications do also exist for non-pathological reasons in individuals of all ages with the most common location being in the pineal gland (Daghighi et al. 2007).

The exact role of the calcifications in diseases is still under debate. They have been related to synaptic excitotoxicity, i.e. in pathological conditions, the post-synaptic receptors are flooded by abnormally high amounts of neurotransmitters such as glutamate (Sattler & Tymianski 2000, Ramonet et al. 2006). The cell is unable to meet the increase in energy demand triggered by receptor activation, e.g. it cannot pump out increasing amounts of cytoplasmic calcium leading to abnormally high concentrations of calcium in the cell. Ca^{2+} is a common secondary messenger in the cell for example, leading to activation of enzymes that damage the cell organelles contributing to cell death. Excitotoxicity is thought to be the common denominator for many neurodegenerative diseases (Dong et al. 2009). Since the high concentration of calcium ions in the cells is so harmful, the formation of the calcifications has been seen as means for the cells to try to restore calcium homeostasis and reduce further brain damage (Ramonet et al. 2006, Mäkinen et al. 2007). The calcifications occur in the form of hydroxyapatite (Mäkinen et al. 2007), similar to what is found in bones (Clarke 2008).

The calcifications have a varying size and morphology depending on the progression of the disease (Ramonet et al. 2006), and the extent of the calcification has been shown to correlate with the amount of glutamate receptor activation (Petegnief et al. 1999). The calcifications can also dissolve with recovery (Lievens et al. 2000). Hence, accurate detection of their stage in time might provide a surrogate marker for the state of the disease.

3.1.2 Imaging methods other than MRI

Calcifications have been imaged with methods other than MRI, although mainly with X-ray based methods. With respect to bone, the relatively high atomic mass number of calcium (Z = 20) leads to a higher photoelectric absorption in the calcification compared to soft tissue, providing a contrast in a computerized tomography (CT) image (Bushberg & Boone. 2011).

Simple cranial x-ray was used to detect calcifications already in the early 1900's (Levin 1926, Murphy 1928), but eventually CT was found to be superior (Norman et al. 1978). In the early days of MRI, CT was shown to be superior in the detection of calcification (Oot et al. 1986), and

it may still be considered as the best method for this purpose (Sedghizadeh et al. 2014). In small animal imaging, CT seems to be only occasionally used for calcification imaging based on this literature review. It has been recently applied to detect calcifications due to bilateral neonatal hippocampal lesions in rats (Macedo et al. 2010, Sandner et al. 2010) and calcifications in genetically modified mice (Keller et al. 2013).

Even though CT is very useful for calcification imaging, it is well known that MRI offers much better soft tissue contrast over CT and unlike CT, MRI does not deliver a high radiation dose to the patient. In the case of brain imaging, good WM-GM contrast is often essential, and CT cannot offer this. In addition, although CT is sensitive to the calcifications, it has also recently been shown to be unable to differentiate between calcifications and a hemorrhage, whereas the MRI method, QSM, was able to distinguish between these conditions (Chen et al. 2014b). It should be noted though that CT is still being developed and steps towards this kind of differentiation have been taken (Nute et al. 2015).

Cranial ultrasound has also been used to detect brain calcifications in small children (Lago et al. 2007, Dykes et al. 1982). The severe limitation of ultrasound imaging is that it cannot be used after the skull bones have grown together, since ultrasound waves do not penetrate through the skull (Pinton et al. 2012).

3.1.3 MRI Magnitude contrast

MRI magnitude contrast is sensitive to calcifications due to their diamagnetic properties and due to their surface interactions with water (Henkelman et al. 1991, Wehrli 2013). In T_2^*-weighted imaging, a calcification is usually seen as a signal void area; this is because the calcification in itself does not emit a signal, since the most common isotope of calcium has a zero spin and is not usable for NMR, and also because its susceptibility induces relatively strong field distortions into its surrounding which lead to intravoxel dephasing and thus fast T_2^*-decay. There are very few studies intentionally trying to detect calcifications in humans or in animals using magnitude contrast of MRI. Human brain samples of stroke have been studied using X-ray fluorescence and compared to T_2^*-maps, phase and susceptibility maps (Zheng et al. 2012). Stroke lesions were found to contain iron, zinc and calcium not always colocalizing spatially, and T_2^*-maps failed to differentiate between iron and calcium, whereas susceptibility maps were able to separate these two from each other. In addition, there have been attempts based on T_2^* to differentiate between bleeding and a calcification (Han et al. 2004). In general, in the context of T_2^* based imaging, calcifications have been reported mainly as signal voids about which one needs to exercise caution , i.e. they have not been considered as very useful or even important. In pursuit of detecting microbleeds, T_2^*-hypointensities have been determined as calcifications based on CT (Kinoshita et al. 2000, Imaizumi et al. 2003), based on shape and bilateral symmetry (Kato et al. 2002, Scheid et al. 2003), based on T_1 weighted images (Vernooij et al. 2008) or the nature of the hypointensity has remained uncertain (Werring et al. 2004).

T_2 weighted imaging is less suited for calcification imaging, since the intravoxel dephasing caused by the calcification is largely refocused in SE type of pulse sequences. T_2 weighted images have been shown to match the place of calcification displaying hypointensity (Melville et al. 1999). In this case, the signal void of the calcification itself overpowers any water or other components with hydrogen in the region. On the other hand, T_2 weighted image findings have been also shown not to match with the calcification detected by CT (Avrahami et al. 1994), or their effect was not seen at all in T_2 weighted images (Iuvone et al. 2002).

Using T_1 weighted contrast, brain calcifications have been shown to be seen as hypointense (Brant-Zawadzki et al. 1983, Holland et al. 1985, Oot et al. 1986, Kjos et al. 1985), isointense or not visible (Brant-Zawadzki et al. 1983, Kjos et al. 1985), but interestingly also hyperintense (Dell et al. 1988, Araki et al. 1990). The hyperintesity has been shown to be due to T_1 shortening using phantoms with increasing amounts of calcium phosphate in solution (Dell et al. 1988) and with increasing amounts of calcium hydroxyapatite in agarose gel (Henkelman et al. 1991), where T_1 also decreased with an increasing surface area of the mineral. In the first case, calcium

ions act as a mild contrast agent. In the second case, the T_1 shortening was related to the surface interaction with the hydroxyapatite where the motion of the water molecules was slowed down, improving energy transfer to the lattice in line with Eq. (10). This kind of surface interaction has been seen using silica powder (Hanus & Gillis 1984), glass beads (Glasel & Lee 1974) and also powdered bone (Davis et al. 1986).

Since calcifications can cause severe signal loss through T_2^* decay, their exact size and shape can be concealed. In this sense, the SWIFT type of imaging could be very useful. Furthermore, in combination with the T_1 shortening, the positive contrast of calcifications might be further enhanced with SWIFT.

3.1.4 MRI Phase, frequency and susceptibility contrast

The field distortion induced by the susceptibility difference of the calcification in comparison to the surrounding tissue, will also affect the MRI phase. In SE, phase accumulates but it is refocused by the 180° RF-pulse. In GRE, the phase created by the field distortion can be seen in the phase contrast, depending on TE and the magnitude of the frequency shift following Eq. (27).

GRE phase contrast and phase maps have been used in calcification detection. One benefit of the phase contrast is that it can differentiate, because of the different direction of the phase accumulation, between calcifications and hemorrhages, since calcifications are diamagnetic and hemorrhages are composed of weakly paramagnetic compounds (Bradley 1993). To date, publication **I** is the only phase imaging study to detect calcifications in animal models. In humans, phase imaging has been used to detect calcifications and to differentiate them from hemorrhages in many pathologies including cancerous tissue, epilepsy, Struge-Weber syndrome and many more (Gronemeyer et al. 1992, Yamada et al. 1996, Gupta et al. 2001, Löbel et al. 2010, Zhu et al. 2008, Saini et al. 2009, Wu et al. 2009). As for the more advanced GRE phase based methods, both SWI and QSM are well suited for calcification detection as, at least in principle, they can differentiate between diamagnetic and paramagnetic substances. Some attempts have been made to detect calcifications and to differentiate them from hemorrhages with SWI (Zhu et al. 2008, Saini et al. 2009, Bosemani et al. 2014) and QSM (Schweser et al. 2010, Liu et al. 2012, Deistung et al. 2013, Chen et al. 2014c) in humans with encouraging results, but there are no animal studies at present on this topic.

Similarly to the situation with the magnitude contrast, SWIFT phase imaging could be very beneficial for calcification imaging since it is not sensitive to T_2^* decay. In comparison to magnitude contrast, the sign of the phase contrast could help in differentiating between a calcification and a bleed. Combined, SWIFT phase and magnitude imaging could accurately describe the state of the calcification.

3.2 PHASE CONTRAST OF BRAIN STRUCTURES

The usefulness of GRE phase maps in brain was shown over two decades ago (Young et al. 1987). However, only recently it has become of greater interest in MRI due to the exquisite contrast between GM and WM demonstrated at 7 T (Duyn et al. 2007), even though the Larmor frequency difference is in the order of <10 Hz. The nature of this contrast has been much debated but no full consensus has been reached (Duyn & Barbara 2014, Duyn 2014, Yablonskiy et al. 2014, Yablonskiy & Sukstanskii 2014). In general, the contrast has been related to the magnetic susceptibility difference between GM and WM due to the high myelin content of WM. The vast majority of phase imaging of the brain structures has been done with GRE, although there are a few tantalizing glimpses of other sequences being exploited (Lee et al. 2011a).

3.2.1 Origins of phase contrast in brain

Multiple contributors have been postulated for the WM-GM phase contrast of GRE, but so far it seems that the main factor is the magnetic susceptibility difference between GM and WM due to

myelin. For example, it was shown in mice with demyelinating cuprizone diet (Blakemore 1973) that the WM-GM frequency contrast decreased from approximately -3.58 Hz to approximately -1.45 Hz at 7 T in the corpus callosum (Lee et al. 2012). A similar finding was demonstrated in shiverer mice that naturally express dysmyelination (Liu et al. 2011, Lodygensky et al. 2012). Finally, a correlation has been demonstrated between the resonance frequency shift and histologic staining of the corpus callosum and the anterior commissure of rats of different ages (Lodygensky et al. 2012). Myelination of the axons continues until adulthood.

The WM phase contrast has been shown to depend on the orientation of the WM fibers in comparison to B_0 (Denk et al. 2011, Lee et al. 2010a, Bender & Klose 2010, Sati et al. 2013). In relation, T_2^* has been shown to be orientation dependent (Lee et al. 2011b, Sati et al. 2012, de Pasquale et al. 2013, van Gelderen et al. 2012, Rudko et al. 2014). The origins of the orientation dependence have been roughly related to either the likely anisotropy of the magnetic susceptibility of WM (Lee et al. 2010a) or to the microstructure of the tissue (He & Yablonskiy 2009). Originally, the orientation dependence was shown in a human corpus callosum cut into pieces, with the pieces in different orientations (Lee et al. 2010a). With the WM fiber orientation parallel to B_0, the frequency shift was approximately -3.89 Hz, and with perpendicular fibers to be +0.56 Hz at 7 T. *In vivo*, orientation dependence was shown in humans by using DTI to measure fiber orientation in different brain structures, although this did not directly show the orientation dependence in the same structure. These kinds of findings have been repeated in a fixed mouse brain (Marques et al. 2009) and marmoset monkey brain (Sati et al. 2013) but not in a rat brain before the second publication of this thesis (**II**). In the marmoset brain, Sati et al. (Sati et al. 2013) found the best fit to the GRE frequency data with a three pool model representing intra-axonal, interstitial and myelin water that is relatively immobile water trapped between the myelin sheaths (Mackay et al. 1994). The frequency shifts of the three compartments measured in the optic radiation perpendicular to B_0 were 35.7 Hz and -5.4 Hz, 1.9 Hz, and in the parallel orientation 2.5 Hz, and 6.9 Hz and 1.1 Hz, respectively. Hence, the fiber orientation has a significant effect on the contrast.

The myelin sheath surrounding an axon is mainly composed of highly organized phospholipids (Baumann & Pham-Dinh 2001) that are long molecules with a hydrophilic phosphorus head and a hydrophobic hydrocarbon body. The phospholipids are organized as a bilayer so that the hydrophilic head is pointing outwards. The anisotropic susceptibility of WM has been related to the structure of myelin sheaths (Lee et al. 2010a, Wharton & Bowtell 2012a), and it has been shown in shiverer mice that the anisotropy disappears in the virtual absence of myelin (Li et al. 2012). The anisotropic susceptibility of a lipid bilayer has also been demonstrated in a bilayer suspension (Lounila et al. 1994).

In terms of anisotropic susceptibility, Wharton and Bowtell applied a so-called hollow cylinder model to describe multi-echo GRE signal from WM with good success (Wharton & Bowtell 2012a, Wharton & Bowtell 2015). The inside and outside of the hollow cylinder represented the intra-axonal and extracellular space, and were set to have zero susceptibility. The cylinder that represented the myelin layers, was set to have an isotropic susceptibility component and different axial and radial susceptibility components to describe anisotropic susceptibility. Although very simplistic, the model was able to fit the data very well. A similar model has been applied successfully by other authors (Sati et al. 2013, Li et al. 2012, Chen et al. 2013).

Another suggestion for the origin of the orientation dependence of the WM phase contrast has been related to the so-called Lorentzian sphere correction. In isotropic media (e.g. liquid) residing inside a homogeneous magnetic field B_0, the macroscopic magnetic field induced by the magnetic susceptibility of the substance is not the same as the field experienced by a single molecule in the media. Instead, because of molecular motion of the surrounding molecules and the molecule itself, the molecule experiences the average field of its surroundings. This can be seen as a spherically symmetric smoothing process leading to average experienced field of zero. Thus, the molecule can be viewed as sitting in a hollow sphere, the Lorentzian sphere, in the

bulk medium. The total magnetic field it experiences due to the medium is the Lorentzian sphere correction summed with the field of the bulk that depends on the overall shape of the object (Durrant et al. 2006).

The Lorentzian sphere assumes that the medium is isotropic. He and Yablonskiy (He & Yablonskiy 2009) argued that a Lorentzian sphere does not apply in WM, since it contains longitudinal susceptibility inclusions, e.g. the myelin sheaths and neurofilaments inside the axons. Instead, they proposed that one should apply a generalized Lorentzian correction, and in the case of myelinated axons, a Lorentzian cylinder. This approach has also been shown to be successful in an experimental setting in explaining the phase contrast behavior of an MS lesion (Yablonskiy et al. 2012) and of a rat optic nerve in different orientations in B_0 (Luo et al. 2014). Recently, Yablonskiy and Sukstanskii expanded the generalized Lorentzian approach to include also the effects of anisotropic susceptibility (Yablonskiy & Sukstanskii 2015). Hence, it may be that the orientation dependence is explained by the combination anisotropic susceptibility and the Generalized Lorentzian correction, though the debate is still on-going.

Another component of the phase contrast in brain has been shown to be chemical exchange (Zhong et al. 2008, Luo et al. 2010, Shmueli et al. 2011). In chemical exchange, a hydrogen atom changes its host molecule from water to another type of molecule in a chemical reaction. As a result, its resonance frequency is changed for the duration that it is in the other molecule (van Zijl & Yadav 2011). How this effect is seen in the signal collected at the water Larmor frequency depends on how fast the hydrogen switches between the pools. If this so-called exchange rate is much slower than the Larmor frequency difference between water and the other species, two distinct peaks would be seen in a spectrum. On the other hand, if the exchange rate is very fast in comparison to the resonance frequency difference, the peaks of these two molecules effectively start to coalesce (Levitt. 2001). In this case, the resonance frequencies shift towards each other, as weighted by the molecule concentrations. Hence, in practice, a small shift of the water frequency towards the other molecule's resonance frequency is seen in areas with chemical exchange.

Zhong et al. (Zhong et al. 2008) were the first to suggest that the chemical exchange between water and macromolecules might influence the resonance frequency. They utilized a bovine serum albumin (BSA) phantom to demonstrate that the resonance frequency of water increases linearly with the concentration of BSA. The frequency change was measured between water and a reference solution, tetramethyl-silyl-propionate (TMSP) that was not thought to interact with macromolecules as it is chemically inert and displays a non-overlapping resonance peak with compounds commonly detected with NMR (Cavanagh et al. 1995). Luo et al. (Luo et al. 2010) went further with similar BSA phantoms by quantifying the contributions of the macromolecule-water exchange and the magnetic susceptibility of the macromolecules to the frequency shift. Luo et al. used dioxane as a reference chemical. According to their results, the effect of susceptibility was approximately double in comparison to that of the water-macromolecule exchange, the former inducing a negative frequency shift and the latter a positive frequency shift.

Shmueli et al. (Shmueli et al. 2011) demonstrated this effect in human and pig brain samples by first immersing the samples in either dioxane or TMSP and then separating the different components by using chemical shift imaging. The exchange effect was shown to be approximately of the same magnitude as the effect of susceptibility but with an opposite sign, being in line with the BSA experiments of Luo et al. TMSP was shown to give different results than dioxane, which was related to TMSP's small, but likely interaction with the macromolecules (Shimizu et al. 1994, Cavanagh et al. 1995). Importantly, a greater frequency shift due to exchange was found in the WM, suggesting that the components of myelin may also be the dominant factor to the frequency shift attributable to the water-macromolecule exchange.

In a recent publication, the use of dioxane and TMSP as reference substances was studied in even more detail (Leutritz et al. 2013) taking into account the possible interaction between water

and the reference, and macromolecules and the reference. It was shown that dioxane shifted water's resonance frequency to a lower field if the concentration was too high, and the interaction between TMSP and water shifted TMSP's resonance frequency to a higher value, though the shift stabilized at sufficiently high concentrations. Hence, dioxane can underestimate the frequency shift and TMSP can overestimate it. It was shown that when TMSP was present at a stable concentration that the frequency shift due to susceptibility may be approximately 1.5 times the water-macromolecule exchange shift instead of double as suggested previously. Clearly, more research is needed on this topic.

Deoxyhemoglobin also seems likely to be a contributor to the phase or frequency contrast. However, the effect of deoxyhemoglobin on the WM-GM tissue contrast has been shown to be negligible by examining phase images in rats breathing oxygen or CO_2 (Marques et al. 2009) or in rats with and without superparamagnetic contrast agent that has a much stronger effect than deoxyhemoglobin (Lee et al. 2010b). On the other hand, the resonance frequency and magnetic susceptibility, calculated using QSM reconstruction, have been shown to be affected by the oxygenation of hemoglobin in functional MRI studies (Bianciardi et al. 2014, Balla et al. 2014). This may be related to a global effect of CO_2 or oxygen breathing and the contrast agent, such that there is a baseline shift but no change in WM-GM frequency difference is seen, whereas the blood oxygen level dependent contrast is localized to the activated brain region. Thus, deoxyhemoglobin is not likely to be a factor contributing to the anatomical contrast.

Iron has been shown to be a strong factor in intracortical phase contrast in human brain samples, and that contrast was also shown to drastically change after removal of iron (Fukunaga et al. 2010), although, in *ex vivo* rat brains, the WM-GM phase contrast was not found to change after removing the iron (Lodygensky et al. 2012). Phase contrast has been shown to correlate with the iron content of brain tissue in the GM but not in the WM of human brain (Ogg et al. 1999). Similarly, *in vivo* human QSM has been demonstrated to correlate with previously published values of iron content in different brain areas after correcting for the effect of different amounts of myelin (Schweser et al. 2011), and further, QSM was shown to correlate well with the iron content in GM but only weakly with that of WM in human brain samples (Langkammer et al. 2012). Hence, iron can have a major role in the phase contrast.

3.2.2 Applications to brain diseases

There have been rather few applications of phase imaging in brain diseases with the majority concentrating on multiple sclerosis e.g. detecting the lesions (Eissa et al. 2009), monitoring the frequency increase inside the lesion over time (Wiggermann et al. 2013) and for detecting different pathological phases of the lesion (Yablonskiy et al. 2012). Additionally, phase images have been used to differentiate between iron rich areas of the brain (Vertinsky et al. 2009), and phase contrast in the cortex has been shown to change over time in Alzheimer's disease patients (van Rooden et al. 2014). There are very few phase brain imaging studies in animal models and those have concentrated more on studying the origins of the phase contrast as presented in section 3.2.1.

Although there are a rather limited number of studies using the phase contrast for brain diseases, QSM is starting to attract considerable interest for clinical (Chen et al. 2014a, Langkammer et al. 2013, Acosta-Cabronero et al. 2013) and preclinical studies (Li et al. 2015, Santin et al. 2015). Since phase images are always an intermediate step in QSM, studying them is also very important. In addition to the excellent contrast, the popularity of QSM is likely related to the quantitative aspect of QSM and its localized contrast; in phase and frequency maps, the contrast extends beyond the source because the field change due to a susceptibility difference extends beyond the source.

3.2.3 Phase imaging using near zero echo time

At present, there is a very limited amount of research exploiting SWIFT, UTE, ZTE or similar pulse sequences for phase imaging. The only example of this kind of work in brain structure

imaging is publication **II** of this thesis. The only reminiscent publication is that of Carl and Chiang using UTE, to examine the phase contrast of a meniscus and also formulated a theory for the phase behavior (Carl & Chiang 2012). It was explained how in UTE phase accumulates during the RF pulse, while ramping the readout gradient and also during the flat portion of the readout gradient. In order to estimate phase accumulation with different sequence parameters for different amplitudes of the off-resonance frequency, Carl and Chiang made an assumption of a sinc-function shaped object, and further assumed that the phase at the center of the object represented the whole object. The theoretical results from the sinc-object were also applied to the meniscus. Despite these seemingly far-reaching assumptions, good correspondence was found between simulations and theory, as well as between phantom experiments and theory. The meniscus experiments showed the power of UTE and other similar sequences: good phase contrast was seen even though the T_2^* values were mostly in the range of < 5 ms. Frequency shifts were in the range of 60 – 80 Hz which is much larger in comparison to difference between GM and WM. With no prior phase imaging studies of the brain using a near zero echo time sequence, there was clearly room for SWIFT in this application. In addition, since the phase contrast with no echo was not as intuitive as with GRE, there was clearly a need for further description of the behavior of the contrast.

3.3 IMAGING TRAUMATIC BRAIN INJURY

3.3.1 Traumatic brain injury

TBI is one of the most common reasons for disability and death. For example, in the United States, approximately 53,000 people die annually after suffering a TBI (Coronado et al. 2011). The most common causes are traffic accidents, falls—especially in the elderly—and violent assault (Bruns & Hauser 2003). TBI is more common in young people and hence, even if not fatal, its socioeconomic and humane impact can be considered as being as especially heavy.

TBI can be classified as either focal or diffuse. The damage occurring after a focal injury is caused by the compression of the tissue immediately below the site of impact to the skull or on the opposite side, where the brain hits the skull. A diffuse TBI is thought to happen more due to rapid linear or rotational acceleration of the brain. Different parts of the brain are differently connected to the skull and also have different elastic properties, leading to different speeds of motion and thus to shear, tensile and compressive forces in the brain tissue that can lead to injury (Andriessen et al. 2010). However, the diffuse injury is not exclusively an immediate tearing of axons, instead, the disconnection of the WM fibers can happen over time (Büki & Povlishock 2006). Both types of injuries can coexist in the same patient, thus complicating the pathology even more.

The effects of TBI have been roughly divided into two components: the primary injury is the initial mechanical damage to the brain and the secondary injury is the ensuing molecular and physiological cascade of events that can last days, months or even years (Ghajar 2000, McMillan & Herbert 2004). In fact, it is the secondary injuries that have been shown to be the leading cause of mortality in TBI patients (Marshall et al. 1991).

3.3.2 Conventional diagnosis

The most common way of assessing the severity of a TBI in a clinic is to apply the Glasgow Coma Scale that reflects how lucid the patient is and how well he/she responds to different types of stimuli. However, this does not reflect the exact underlying brain damage (Andriessen et al. 2010) and is hence inadequate for treatment decisions. Naturally, this means that the physician will wish to access different types of medical imaging modalities. CT is currently the method of choice in the acute phase since it is quick at detecting the initial structural damage and intracranial hematomas that may require immediate intervention (Maas et al. 2008, Davis 2007). MRI is the preferred method in the chronic phase since it is more sensitive to subtle changes in the brain tissue. MRI can also be used in the acute phase if the head trauma is

initially evaluated as being mild as in that situation, fast imaging is not as crucial. The most dramatic effects of TBI are easily visualized by CT, but it has been shown that even in the acute phase, MRI detects pathological features not detected by CT (Lee et al. 2008).

Conventionally, MRI of TBI has been conducted with four pulse sequence types: fluid attenuated inversion recovery (FLAIR), T_2^* weighted imaging, T_2 weighted imaging and diffusion weighted imaging (DWI) (Brandstack et al. 2006). FLAIR detects the main contusion, brain edema and bleeding at the surface of the brain, whereas T_2^* weighted imaging is more sensitive to bleeding in the brain parenchyma. SWI has been shown to sensitize T_2^* weighted imaging even more (Nandigam et al. 2009). T_2 weighted imaging provides better WM-GM contrast, although on the other hand DWI has been shown to be more sensitive to cellular damage (Galloway et al. 2008). Interestingly, after the acute period, these methods start to lose sensitivity to the underlying tissue pathologies, and without the initial images, these may go unnoticed (Brandstack et al. 2006). On the other hand, for example in an acute phase of a mouse TBI model, DTI has been shown to be more sensitive to WM injuries than T_2 or DWI (Mac Donald et al. 2007a). Thus, many aspects of TBI are left undetected by conventional MRI (Provenzale 2010). Hence, one of the goals of this thesis was to further explore the power of more sophisticated MRI methods for detecting subtle changes in the brain due to TBI.

3.3.3 Experimental traumatic brain injury

Studying TBI in humans in detail is close to impossible not only because of acute need for care but also because of ethical reasons. Many animal models have been developed in attempts to elucidate the pathophysiology of TBI. Since TBI is such a multifaceted pathology, it is impossible to include all the effects within one single model. Additional complexities arise from interspecies differences, although rodents are the animals most commonly used (Xiong et al. 2013).

The models include e.g. controlled cortical impact, weight-drop, blast injury and fluid percussion injury (FPI), with multiple variations of each (Xiong et al. 2013). The controlled cortical impact model uses a rigid impactor hitting the exposed dura of the animal. The impact strength can be controlled very precisely which is also the greatest benefit of the model. The weight drop model uses an impactor with a controlled path and a weight dropped from a certain height onto the exposed skull, with or without an exposed dura. This model is less controllable, but it can mimic the human TBI better than FPI. The blast injury model has been developed mainly because as a way of investigating the damage in military personnel who display signs of TBI but with no external injuries. In this model, the animal may be inserted into a tube where a blast wave is induced by a pressure shock.

In FPI, the exposed dura is connected to a fluid that causes a pressure wave produced by a weighted pendulum or a specialized microcontroller device (Kabadi et al. 2010). The severity of the injury is controlled by adjusting the pressure and length of the wave. The placement of the craniectomy divides the FPI into midline FPI or lateral FPI (LFPI). The LFPI (McIntosh et al. 1989) is one of the most commonly used TBI models and it is also the model used in this thesis (**I**, **III**). There are two main benefits associated with LFPI (and FPI); it is highly reproducible and the severity is very adjustable. On the other hand, it needs a craniectomy and it has a rather high mortality rate. LFPI has been deemed as a clinically relevant model since it displays several different features of human TBI (Thompson et al. 2005). LFPI also leads to a mix of focal and diffuse injuries.

Finally, although results emerging from experiments conducted with different TBI models have profoundly increased knowledge about TBI, no clinically successful therapeutics have still been discovered (Maas et al. 2008, Greve & Zink 2009, Andriessen et al. 2010, Xiong et al. 2013). Hence, further studies with the TBI models are needed.

3.3.4 Thalamocortical pathway

The corticothalamic and thalamocortical fibers connect the thalamus and the six layers of the cortex (Grant et al. 2012). Different nuclei of the thalamus are connected to one or multiple cortical layers, and on the other hand, the cortical layers are linked to one or multiple nuclei in the thalamus. These complicated thalamocortical and corticothalamic pathways form the so-called corticothalamic circuit, a crucial pathway not only in processing peripheral sensory information, i.e. vision, audio, etc., but also in higher order processing. Hence, the proper functioning of the thalamocortical pathway is essential for a normal life. Since MRI cannot differentiate between pathways with different directions, for simplicity, the term thalamocortical pathway is used here.

It is already known that the placement of a diffuse axonal injury (DAI) can be very crucial for the severity of the network dysfunction in the brain, even if the damage is not extensive (Sharp et al. 2014). For example, in patients with TBI, a reduction in WM integrity was found in multiple areas using DTI, but the damage to the cortico-subcortical connections was the main factor in task switching deficits (Leunissen et al. 2014). These kinds of findings emphasize the importance of studying the thalamocortical pathway after TBI in animal models. Furthermore, in the sense of MRI, it is important to determine the optimal methods and to elucidate what aspects of the pathologically altered tissue they actually show.

3.3.5 MT imaging of traumatic brain injury

There have been very few MT studies of TBI and there are no MT studies in TBI models using rats. However, MT has been applied to TBI imaging in humans and in a minipig model. Kimura et al. (Kimura et al. 1996) were the first to apply MT into a DAI model in a minipig seven days after injury. Rotational acceleration was applied to the head to induce DAI. The benefit of the minipig as a model is the structure and size of the brain that are close to that of the human being. MT was seen to be reduced in 19 out of 41 analyzed areas and verified by histology to have undergone an axonal injury. In some cases, T_2 weighted images were also positive (6 out of 19 areas with MT change). McGowan et al. also imaged a minipig DAI model at 3 h and 7 days after injury (McGowan et al. 1999). MTR was reduced in multiple areas, whereas no changes were seen with T_2 weighted imaging. The positive and negative predictive values for MTR in detecting the DAIs were 67 % and 56 %, respectively, with both time points and 89 % and 61 % for only the acute time point.

Bagley et al. (Bagley et al. 2000) were the first to apply MT to human TBI with mixed injury severities. They found no statistically significant decreases in MTR between patients and controls, however, MTR was always reduced in patients with a poor outcome compared to those with a good outcome, even when the T_2 weighted imaging was positive. McGowan et al. (McGowan et al. 2000b) observed a reduced MTR in mild TBI patients, but MTR was found to correlate with neuropsychological testing in only two out of 13 patients. They speculated that this might have been related to heterogeneities in the patient populations and their symptoms and the fact that the ROI analysis was conducted on WM, whereas neuropsychological testing reflected more the functionality of GM. Comparable results were found by Sinson et al. (Sinson et al. 2001) who detected no correlation between MTR and TBI outcome, although reduced MTR was observed in the patients. Kumar et al. (Kumar et al. 2003) reported decreased MTR and increased T_2 in the GM of TBI patients when conventional T_2- and T_1 weighted imaging was negative. Finally, Mamere et al. (Mamere et al. 2009) applied MTR to TBI patients at a chronic time point (average of 3.1 years after TBI) in an attempt to detect secondary damage. They found decreased MTR and increased T_2 in normal appearing WM and the corpus callosum compared to the control group and in addition, increased ADC was detected.

Promising results have been shown with MT in imaging TBI, but it seems to have been under-utilized. In addition, the studies presented above did not reveal results that would explain the MT contrast behavior in depth. MT has also shown excellent results in disease models of other neurodegenerative diseases (Fjær et al. 2013, McGowan et al. 2000a, Ou et al.

2009), e.g. being sensitive to demyelination, a very common aspect of WM pathology. Hence, in this thesis, we sought to apply MT for the first time in an LFPI rat model in both GM and WM. In addition, since SWIFT enables almost an absence of T_2^* weighting, it was possible to obtain a more pure MT contrast e.g. ensuring that blood products did not bias the results obtained.

3.3.6 Diffusion MRI of traumatic brain injury

Although DWI has been shown to be a very useful tool in detecting DAI based on decreased ADC due to cytotoxic edema (Sotak 2004), DTI offers much more detailed information about the subvoxel microenvironment and is thus better at detecting less obvious pathology. DTI has slowly attracted interest for TBI imaging, however, it is not yet used in clinics on a regular basis (Zappala et al. 2012), although it is often seen by the MRI community as the golden standard method with which to assess WM integrity.

FA and RD have been related to demyelination so that the opening extracellular space has less effect to restrict diffusion (Song et al. 2002, Song et al. 2005), and decreased, not increased, AD has been commonly related to axonal damage based on animal models which has been interpreted to mean that axonal debris restricts diffusion (Song et al. 2003, Wu et al. 2007, Sun et al. 2008). In human studies, DTI has been shown to differentiate between mild and moderate or severe TBI, so that the number of WM areas with a significant FA decrease was larger in more severe cases (Kraus et al. 2007). In addition, increased AD and RD were found in more severe TBI, but only increased AD was found in mild TBI, and although in contrast to the results from animal studies, the authors related these findings to axonal and myelin damage. In a longitudinal study of TBI patients (Sidaros et al. 2008), FA and AD decreased while RD increased initially. In the follow-up, in those patients with a good outcome, FA and AD increased back close to normal without any change in RD, whereas in patients with a poor outcome the parameters remained unchanged. Furthermore, it has been shown that at a longer time point after TBI in patients, AD can increase above controls, possibly reflecting axon regrowth or even recovery (Kinnunen et al. 2011). Hence, in a simplified manner, it may indeed be the case that AD can be related to axonal damage, being decreased in the acute phase and with possible recovery, increasing over time. FA and RD can be viewed as more related to myelin damage, although of course these parameters are interrelated.

There are only a few DTI studies with TBI animal models. *Ex vivo* DTI has been used to study the hippocampal structures (Laitinen et al. 2010, Sierra et al. 2013) and WM structures in an LFPI model (Laitinen et al. 2015). Animal model studies have revealed similar results to human studies. In the acute phase, AD and FA have been shown to decrease with no change in RD (Mac Donald et al. 2007a), and further in the subacute phase FA and AD increase close to normal levels, even with axonal injury verified by histology, while RD starts to increase (Mac Donald et al. 2007b, Li et al. 2011). In a chronic time point after a severe LFPI, decreased FA and increased RD were seen in WM structures of the rat (Laitinen et al. 2015). The cortex has not been studied in this model and the thalamocortical pathway has not been studied with DTI in any TBI model. Hence, a detailed study of the DTI contrast with a comparison to histology would be extremely valuable.

DTI has shown great promise for diagnosing TBI and other brain insults, but it does have limitations. The principal limitation as with all MRI approaches, is that DTI collects information averaged over a voxel. Hence, even though it is sensitive to diffusion at the microscopic level, it can only describe averaged diffusion (Jones et al. 2013). Furthermore, since the DTI pulse sequences are only sensitive to dephasing of the magnetization, assumptions have to be made about how the signal has originated. In the case of DTI, it is assumed that the diffusion follows a 3D Gaussian probability distribution (see section 2.6). Because of these facts, one major topic of interest in DTI and diffusion imaging has been the so-called crossing fibers. Given that a voxel contains only parallel WM fibers, it is easy to see how the single Gaussian probability distribution can describe the diffusion rather accurately, the highest probability of diffusion being in the direction of the fibers. On the other hand, given that there are two populations of

fibers perpendicular to each other inside the voxel, the average diffusion is described by a Gaussian probability distribution, symmetric at the plane of the fibers, as if diffusion was equally probable to any direction in this plane. In addition, there is no restriction on where inside the voxel these two populations would cross, because the result is the same in any case. Naturally, brain structures rarely consist of purely parallel or perpendicular fibers and as such, this kind of directional averaging happens more or less depending on the fiber orientation distribution. In a healthy brain, this can cause misinterpretation of the underlying structure. In brain pathology, this can lead to misdiagnosis or entirely missing the pathology. For example, as stated before, increasing RD has been shown to reflect demyelination and this also decreases FA. On the other hand, this was shown in the corpus callosum that may be the most parallel in fiber orientation out of all WM structures. In the case of crossing fibers, the situation becomes problematic i.e. if both fiber populations experience demyelination, diffusion would change equally perpendicular in both directions and hence FA would remain unchanged. In addition, the terms RD and AD, although by definition pointing to the eigenvalues of the diffusion tensor, often seem to be relating to the fiber direction in the literature. However, in the crossing fiber situation, this idea becomes almost meaningless (Wheeler-Kingshott & Cercignani 2009). Naturally, pathology can further complicate the situation. All this does not render DTI useless, but it does mean that care does need to be taken when interpreting the data, and furthermore, it emphasizes the desirability of more detailed studies comparing DTI and histology.

4 *Aims of the study*

This thesis focused on applying the emerging pulse sequence SWIFT for brain imaging. It was noticed early on that SWIFT produces phase contrast, even though this seemed counterintuitive based on what was known about GRE phase imaging. Hence, the first publication explored the use of SWIFT phase contrast for detecting diamagnetic calcifications. The second publication studied SWIFT phase contrast of brain structures, taking a step in the direction of examining much weaker magnetic field perturbers. Research continued towards applying SWIFT phase imaging for brain structures after a brain insult and comparing to DTI, but the phase contrast results were deemed corrupted due to experimental difficulties. Hence, in the final publication, SWIFT magnitude contrast results were used instead.

The aims of the study were:

1. To study the feasibility of using SWIFT phase contrast to detect relatively strong field deviations created by brain calcifications

2. To examine the potential of using SWIFT phase contrast for brain structures with very small field differences and to clarify the properties of SWIFT phase contrast

3. To detect subtle changes due to secondary injuries after TBI using SWIFT magnitude contrast with a comparison to DTI and histology.

5 Materials and methods

This chapter explains the MRI methods, data analyses, animal models and the histological methods of the original publications. All animal experiments were done using rats. The animal procedures were approved by the Animal Ethics Committee of the Provincial Government of Southern Finland (for TBI 2008-05812, for epilepsy 2010-05651), and conducted in accordance with the guidelines set by the European Union 2010/63/EU.

In study **I,** the animal experiments were done in the A. I. Virtanen Institute for Molecular Sciences (AIVI) and the phantom experiment was done in Center for Magnetic Resonance Research (CMRR) of University of Minnesota. For study **II,** *in vivo* rat imaging and human brain sample imaging were done in CMRR, all other experiments were done in AIVI. For study **III**, all studies were done in AIVI. All experiments used MRI scanners with Agilent DirectDrive consoles (Agilent, Palo Alto, CA).

5.1 BRAIN PERFUSION AND PREPARATION FOR *EX VIVO* IMAGING (I, II, III)

Ex vivo imaging of the rat brain was conducted in every publication, and histology was performed in original publications **I** and **III**. In both of these experiments, perfusion of the brain was necessary. The animals were deeply anesthetized with an i.p. injection (7 ml/kg) of solution containing sodium pentobarbital (10 mg/ml), chloral hydrate (10 mg/ml), magnesium sulfate (21.2 mg/ml), propylene glycol (40%), and absolute ethanol (10%) and perfused transcardially with saline for 5 min (30 ml/min) followed by 4% paraformaldehyde in 0.1 M phosphate buffer, pH 7.4 (30 ml/min) for 25 min. The brains were removed from the skull and post-fixed in 4% paraformaldehyde for 4 h. Prior to *ex vivo* MRI, the brains were washed and stored in 0.9% NaCl solution. For *ex vivo* imaging, the brains were immersed in perfluoro polyether Fomblin® LC08 (**I**) or Galden® (**II**, **III**; Solvay Solexis, Milan, Italy) for susceptibility matching, to prevent tissue drying and to avoid signal sources from outside the brain. The container for the imaging in studies **I** and **III** was made out of Teflon® in order to further minimize signal from outside the brain, since SWIFT would detect short T_2^* signal from most of commonly used plastics (Marjanska et al. 2008).

5.2 PHANTOM MRI AND SIMULATION EXPERIMENTS (I, II)

Phantom studies are an essential part of MRI in studying and demonstrating different physical phenomena and signal acquisition related effects. Phantoms were used in studies **I** and **II**.

5.2.1 Glass bead phantom (I)

To demonstrate how a dipole field would be reflected by SWIFT phase in comparison to GRE and to verify the theoretical predictions in study **I**, a phantom was made out of a glass bead of diameter 212–300 μm (Sigma-Aldrich, St. Louis, MO) imbedded in agar gel made in saline. The phantom was imaged on a horizontal 9.4 T magnet using a single loop coil. The SWIFT parameters were: TR = 8.1 ms, acquisition bandwidth (SW) = 31.125 kHz, flip angle = 7°, 128000 spokes, FOV = 4.5^3 cm^3, reconstruction matrix size = 384^3, two averages and a scan time of 36 min. The GRE3D parameters were TR = 20 ms, TE = 5 ms, SW = 62.5 kHz, flip angle = 11° (500 μs sinc), FOV = 3^3 cm^3 and matrix size = 256^3, and scan time of 33 min.

5.2.2 Short T2* phantom (II)

To study the SWIFT phase behavior with different T_2^* relaxation times, 5 mm NMR tubes with 0.25 mM, 1.00 mM and 4.00 mM $MnCl_2$ solutions were imaged with SWIFT in a horizontal 9.4 T magnet using a 19 mm quadrature volume coil. The center frequency was shifted by 0, -30, -60, -90 and -120 Hz. The relaxation times were measured to be 18.8 ms, 5.2 ms and 1.8 ms, respectively, at the center slice of the sample using multi GRE 3D (MGRE3D, TE = 0.8 / 1.8 / 2.8 / 3.8 / 4.8 / 5.8 / 6.8 / 7.8 ms). The phantom was imaged with SWIFT using different SWs to achieve varying acquisition times, and with different FOVs to have different relative object sizes which provided different spatial frequency contents of k-space. SWIFT parameters were: TR ≈ acquisition time, SW = 62500, 41667, 31250, 25000, 21888, 17860 and 15625 Hz, flip angle = 10°, 64000 spokes and reconstruction matrix size = 192^3. The data was acquired using a gapped HS pulse (n = 2, R = 128; HS2R128) so that the first half of the acquisition period alternated between RF pulsing and acquisition, and in the second half acquisition was continued without RF pulsing. A total of 128 points were collected, reducing to 96 points after correlating with the HS pulse. Data was acquired and reconstructed using CMRRpack v0.45a software (www.cmrr.umn.edu/swift/). True off-resonances and scanner drift were approximated with linear interpolation between B_0 maps before and after SWIFT acquisitions.

Simulations of a cylindrical object with parameters equal to the phantom were made based on the equations shown in study **II,** and compared to average phases of regions of interest (ROI) drawn in Matlab (Mathworks, MA, USA) using Aedes (aedes.uef.fi) at the center of the phantom images and simulated cylinders. Pixels close to the phantom edge were excluded to avoid partial voluming effects.

Additional simulations with varying magnitude ratios of "GM" and "WM", and varying "WM" T_2^* were conducted in a 1D "WM stripe" to demonstrate phase behavior in a structure with geometry closer to a "WM" structure such as the corpus callosum, as it has a different spatial frequency content compared to a cylinder.

5.3 *IN VIVO* MRI (I, II, III)

Only SWIFT was used in *in vivo* imaging experiments for detecting calcifications with phase contrast (**I**), to demonstrate *in vivo* WM-GM phase contrast (**II**) and to measure MTR of the thalamocortical pathway (**III**).

The *in vivo* SWIFT imaging parameters are shown in Table 1. Imaging was conducted using a Teflon housed quadrature RF-transceiver coil custom made for SWIFT (**I**, **III**) and a normal quadrature RF-transceiver coil (**II**). Some signal was observed as originating from the latter's plastic structures, but it was included in the FOV and did not reach the brain itself. The *in vivo* experiments were done at a 9.4 T horizontal scanner (**I**, **III**), and at a 16.4 T horizontal scanner (**II**).

In study **III**, MT weighting was achieved by applying two consecutive HS4R20 (20 ms, BW = 1 kHz, ω_1 = 500 Hz) pulses at ± 1.5 kHz off-resonance repeated every 16 acquisitions. HS pulses were used because of their sharp profile. For the MT reference image, the MT preparation was replaced by a fat saturation scheme (Table 1). Since it is a radial pulse sequence, SWIFT requires more acquisitions for full sampling of the k-space in comparison to Cartesian imaging with the same matrix size. Hence, the TR is usually minimized, and to further minimize scan time, magnetization preparations are not applied on every TR. Usually, T_1 is much longer than the time between the preparations and hence the signal level variation is not significant. In study **I**, **the** SWIFT acquisition used HS1R256 with no acquisition after the RF pulse leaving 128 post-correlation points per acquisition, and in studies **II** and **III,** HS2R128 was used with 128 points acquired after the RF pulse leaving 192 post-correlation points. The same pulses were used in the corresponding *ex vivo* studies.

Table 2. SWIFT parameters for *in vivo* imaging.

	B_0 (T)	TR (ms)	SW (Hz)	Flip (°)	Reconstruction matrix	FOV (cm^3)	Fat suppression	Spokes	Averages
I	9.4	8.1	31250	6	256^3	6 x 4.5 x 4.5	Sinc, 90°, 6 ms, every 16 spokes	49152	4
II	16.4	8.6	31250	5	256^3	4^3	Gauss, 120°, 1 ms, every 16 spokes	393000	1
III	9.4	8.1	31250	5	256^3	6 x 4 x 4	Gauss, 90°, 3.3 ms + 36.7 ms delay, every 16 spokes	196608	1

In the *in vivo* imaging, the animals were anaesthetized using an oxygen/nitrogen 21%/79% mixture with 1.0-1.5 % isoflurane, incubation with 5% isoflurane. The animals were placed in a plastic animal holder, immobilized with ear pins and a tooth bar. Respiration was monitored using a pressure sensor and the respiration rate was kept at 60-70 per minute by adjusting the isoflurane level accordingly. The animals were kept warm by a heated water circulation.

5.4 *EX VIVO* MRI (I, II, III)

Ex vivo imaging was an important part of this thesis. Small animal MRI in general can be challenging in terms of the SNR, since the animal brains are considerably smaller than the human brain. Given that similar anatomical resolution is desired, signal levels can become low, especially with 3D imaging. Hence, *ex vivo* imaging is often very useful for highlighting different phenomena and demonstrating what is possible with a certain pulse sequence given that adequate SNR can be achieved. All the studies in this thesis included *ex vivo* experiments. The *ex vivo* experiments of studies **I** and **III** were done at vertical 9.4 T scanner, and for study **II** all *ex vivo* scans were done at horizontal 9.4 T except for the human brain sample that was scanned at horizontal 16.4 T.

Table 3. SWIFT parameters for *ex vivo* imaging for studies **I** and **III**.

	B_0 (T)	TR (ms)	SW (Hz)	Flip (°)	Reconstruction matrix	FOV (cm^3)	Coil	Spokes	Averages
I	9.4	5.1	62500	5	256^3	4^3	19 mm volume	128000	4
III	9.4	8.1	31250	6	384^3	3.7^3	19 mm volume	524288	1

5.4.1 Pilocarpine and TBI animals (I, III)

SWIFT was used to detect calcifications *ex vivo* in pilocarpine-treated and TBI rat brain with phase contrast (**I**) and to measure MTR of the *ex vivo* rat thalamocortical pathway after TBI (**III**). The *ex vivo* SWIFT parameters are shown in Table 3.

Fewer averages and more spokes were acquired in study **III** than in study **I**, as there were improvements in the SWIFT pulse sequence itself and also in the reconstruction program. To fully sample k-space in 3D radial imaging, one needs πN^2 spokes, where N is the final matrix size in one dimension. Hence, for a 256^3, approximately 200000 spokes are needed. However, when using the earlier version of SWIFT in study **I**, even though under-sampled, the chosen parameters were found to be optimal in practice. A dedicated *ex vivo* 19 mm quadrature volume coil was used in both studies. Since the coil elements of this particular coil are seen using SWIFT, the FOV was set as relatively large in comparison to the brain to include the coil in the FOV.

In study **I**, using SWIFT phase in *ex vivo* calcification detection was compared to conventional single echo GRE. The parameters were TR = 50 ms, TE = 1.9 ms, SW = 208.3 kHz, flip angle = 25° (500 μs sinc), 4 averages, FOV = 2 × 2 × 4 cm^3, matrix size = 128 × 128 × 256.

The main part of study **III** compared MTR, measured with SWIFT, and DTI, in a chronic time point after a TBI. The DTI protocol consisted of a simple 3D SE using the minimum of six diffusion weighted directions and a b-value of 1000 s/mm^2. The parameters were: TR = 1 s, TE = 30 ms, acquisition bandwidth = 33.8 kHz, FOV = 2.93 x 1.65 x 1.37 cm^3, matrix size = 256 x 72 x 60, two averages, resolution after zero padding = 114^3 μm^3, Δ = 17 ms, δ = 5 ms and one acquisition without diffusion weighting. Although the DTI protocol was lengthy, it was deemed very robust, in the sense of eddy currents, and high SNR. The diffusion weighted images were eddy current corrected using a linear affine alignment to the non-diffusion weighted image and the diffusion tensors were solved with FSL (http://www.fmrib.ox.ac.uk/fsl/) (Jenkinson & Smith 2001, Jenkinson et al. 2002, Jenkinson et al. 2012).

5.4.2 Orientation dependence of the phase contrast in brain (II)

One of the key features of WM-GM phase contrast is the orientation dependence. Hence, it was considered important to compare SWIFT phase contrast behavior to GRE phase contrast in this context. In addition, the comparison provided a way to determine the magnitude of change when the resonance frequency changed by only a few Hertz in the same structure.

An *ex vivo* rat brain was immersed in perfluoro ether in a 20 mm NMR tube with no SWIFT detectable signal. The tube was big enough so that the brain could be placed inside horizontally. The tube was further put inside an approximately 20 mm wide loop coil so that the brain was in the middle of the loop. This set-up enabled rotation of the brain. The loop coil structures emitted no SWIFT visible signal. The brain was scanned with SWIFT and MGRE3D so that the rostro-caudal axis of the brain was at angles 0°, 18°, 36°, 54°, 72° and 90° to B_0. The angle was checked based on pilot GRE images. The SWIFT parameters are shown in Table 4 and the MGRE3D parameters in Table 5. MGRE3D flip angle and TR were set accordingly so that the T_1-contrast was approximately the same as with SWIFT.

5.4.3 Phase accumulation time and phase contrast (II)

Since the acquisition delay or TE of SWIFT is minimal, it has a minimal effect on phase accumulation. Instead, the acquisition time was seen to be the time for phase accumulation. To demonstrate this phenomenon, an *ex vivo* rat brain was scanned with SWIFT using different SWs. The used SWs led to effective acquisition times of 12.3/9.2/6.1 ms. TR was set to equal 34.5 ms by adding the corresponding delay after the acquisition, enabling a direct comparison to MGRE3D in the sense of TR and flip angle. The parameters are shown in Table 4 and Table 5 for SWIFT and MGRE3D, respectively.

Table 4. SWIFT parameters for ex vivo imaging study **II**.

	B_0 (T)	TR (ms)	SW (Hz)	Flip (°)	Reconstruction matrix	Res (μm^3)	Coil	Spokes	Averages
Orientation	9.4	8.6	31250	7	384^3	78	Loop	524288	4
Acq length	9.4	34.5	15625 20833 31250	14	384^3	96	19 mm volume	524288	1
Human brain sample	16.4	8.6	31250	7	384^3	130	TEM volume	1048576	1

In these experiments, the scanner drift was noted to have a relatively large effect on SWIFT phase contrast. Hence, this had to be taken into account. In the version of the SWIFT pulse sequence used in studies **II** and **III**, acquiring a full data set was divided into parts so that in one part it consisted of 65536 spokes. This was then repeated eight times for total of ~500k spokes. This type of acquisition enabled collecting a water line between each part and the peak

frequency was used to follow the scanner drift. The mean frequency offset during a single SW experiment was then used to correct for scanner drift in the image reconstruction.

5.4.4 MT preparation (II, III)

Since SWIFT is able to detect very short T_2^* components, the question of being able to detect myelin lipid signal directly was considered during this thesis project. Some attempts were made for long T_2^* suppression using long adiabatic inversion pulses (Larson et al. 2006, Lehto et al. 2010), but the results were believed to be unreliable due to MT. However, a similar approach was later used with UTE to detect a myelin lipid signal (Wilhelm et al. 2012, Du et al. 2014) with verification by longer TEs (Du et al. 2014). Nevertheless, because of suspected MT contamination, it was decided to use a clear MT preparation to suppress any possible short T_2^* components.

In study **II,** the length of acquisition experiments were repeated with a Gaussian pulse of 24.4 ms applied at −1.4 kHz off-resonance with amplitude of 0.6 kHz every 4th TR in both SWIFT and MGRE3D. As a reference, the initial length of acquisition scans were done with a 24.4 ms delay every 4th TR. In study **III,** the *ex vivo* MT weighting was applied as for *in vivo* (see section 5.3): two consecutive HS4R20 (20 ms, BW = 1 kHz, ω_1 = 500 Hz) pulses at ± 1.5 kHz off-resonance every 16 acquisitions. In the reference scan, the MT-preparation was replaced with a 40 ms delay.

5.4.5 Phase contrast of a human brain sample (II)

Since rat brain is small, it is difficult achieve sufficiently high resolution to have multiple pixels over the width of a WM structure. Hence, in order to demonstrate better how SWIFT phase would behave inside a WM structure that is large relative to the FOV, a human brain sample was scanned.

A coronal 1 cm slice of a donated formalin fixed healthy human brain was acquired from Laboratory Medicine and Pathology of University of Minnesota Hospital. A piece cut off from the temporal lobe was placed in a SWIFT invisible tube and immersed in perfluoro ether (Galden®, Solvay Solexis, Milan, Italy). SWIFT parameters are shown in Table 4. For comparison, the brain sample was also imaged with MGRE3D with the parameters shown in Table 5.

5.4.6 GRE phase and frequency map processing

For frequency and phase map calculation, the GRE3D or MGRE3D data were high-pass filtered using complex division with Gaussian kernel (Mittal et al. 2009). In study **I,** the kernel widths were 15 and 10 pixels for phantoms and brains, respectively. In study **II,** the kernel width was always 10 pixels. The frequency maps were calculated using a simple one compartment linear fit.

Table 5. MGRE3D parameters for study **II**.

	B_0 (T)	TR (ms)	TE (ms)	SW (Hz)	Flip (°)	Res (μm^3)	Coil	Averages
Orientation	9.4	34.5	3.4/9.5/15.6 /21.7/27.8	62500	14	78	Loop	10
Acq length	9.4	34.5	2.7/7.6/12.5 /17.3/22.2	62500	14	96	19 mm volume	14
Human brain sample	16.4	20	2.0/5.4/8.8/ 12.1	62500	11	130	TEM volume	4

5.5 ANIMAL MODELS

5.5.1 Pilocarpine injection (I)

Pilocarpine injections are used to induce status epilepticus. The initial injection may or may not lead to spontaneous seizures (Goffin et al. 2007). Injections were conducted in male Wistar rats (10 weeks old, weight 300–350 g, National Laboratory Animal Center, Kuopio) (n = 8). Rats were injected with scopolamine (s.c., 2 mg/kg; # S-8502, Sigma, Chemical Co., St. Louis, MO, USA) to reduce the adverse effects of pilocarpine. Thirty minutes later, pilocarpine injection was administered (i.p., 320 mg/kg, # P-6503, Sigma, Chemical Co., St. Louis, MO, USA). The development of status epilepticus was observed visually for 3 h, and only the rats that developed recurrent generalized seizures were included in the study. Finally, diazepam (i.p., 10 mg/kg, Stesolid Novum, Dumex-Alpharma) was administered to reduce mortality. Age- and weight-matched controls received saline (n = 6).

5.5.2 Lateral fluid percussion injury (I, III)

LFPI (Kharatishvili et al. 2006) was chosen for modeling TBI in studies **I** and **III** because of its high reproducibility. Male Sprague–Dawley rats (10 weeks old, weight 300–350 g, Harlan Netherlands B.V., Horst, Netherlands). Briefly, rats (study **I**, n = 5; study **III**, n = 6) were anesthetized by an injection of a mixture (6 ml/kg, i.p.) containing sodium pentobarbital (58 mg/kg), chloral hydrate (60 mg/kg), magnesium sulfate (127.2 mg/kg), propylene glycol (42.8%), and absolute ethanol (11.6%). A craniectomy of 5 mm in diameter was performed between the bregma and lambda on the left convexity (anterior edge 2.0 mm posterior to the bregma; lateral edge adjacent to the left lateral ridge). LFPI was induced by a transient fluid pulse (21–23 ms) against the exposed dura by using a fluid-percussion device (AmScien Instruments, Richmond, VA). The impact pressure was controlled to 3.2–3.4 atm, to induce a severe brain injury. After impact, the dura was checked to ensure that it had remained intact. Sham-operated control animals (study **I**, n = 4; study **III**, n = 5) received all surgical procedures except the impact.

5.6 HISTOLOGY

The possibility to compare MRI results with histology is one of the great benefits of animal experiments. Histology enables us to examine at microscopic level what MRI, a macroscopic imaging method, is actually detecting. In human studies, although sometimes samples are available, the interpretation of the MRI results is more difficult. Histology played an important part in this thesis, being extensively used in studies **I** and **III**. In all studies, the brains were cut into 1-in-5 series with a 30 μm section thickness. The pilocarpine brains of study **I** were sectioned in the coronal place, while all TBI brains were sectioned in the horizontal plane (**I**, **III**).

Alizarin staining (Mäkinen et al. 2007) was used to detect the calcifications and Nissl staining was used to assess the cytoarchitectonic borders, gliosis, and severity of neurodegeneration in various brain areas in study **I**. To show the presence of glial cells, GFAP and OX-42 immunostainings were used to stain astrocytes and microglia, respectively.

In study **III**, the adjacent series of sections of the TBI brains were stained with Nissl, gold chloride to detect myelin, and with Perls' iron staining. These three stains were assessed as being the most important ways to reveal the DTI and MTR changes at a chronic time point after TBI. Nissl staining showed all cells in general and hence the extent of gliosis could be analyzed through a comparison to the hemisphere contralateral to the injury and to the sham animals. Loss of myelinated axons is an essential component of the secondary injuries of TBI (Andriessen et al. 2010) and has been related to both DTI and MT contrasts as stated above. Iron is also an important factor of TBI and can accumulate due to e.g. bleeding.

5.7 DATA ANALYSIS

5.7.1 Calcifications (I)

Although the calcifications were known not to be perfectly spherical, they were still predicted to create a dipole like field surrounding them. Since they were also known to be diamagnetic in comparison to the surrounding tissue, it was found to be possible to separate them from paramagnetic substances such as blood products, based on the orientation of the dipole. Hence, the calcifications were located by using the SWIFT phase maps or the imaginary component. SWIFT phase images did not need post-processing.

The volume of the calcifications was calculated based on SWIFT magnitude images using Aedes (aedes.uef.fi/) based on signal intensity. Hypointense and hyperintense calcifications (see below) were separated based on their contrast with the surrounding brain tissue in magnitude images. Each calcification detected with SWIFT was identified from Alizarin stained sections and the size was measured for correlation.

The presence of astroglia and microglia was separately evaluated in calcifications from GFAP or OX42-immunostained sections. Most of the calcifications were analyzed in both immunostainings in consecutive sections. The scoring was as follows: 0 = no glial cells, 1 = a few scattered glial cells around the calcification, 2 = a band of glial cells surrounding the calcification, and 3 = a thick and densely populated rim of glial cells around the calcifications. The mean score over the sections was calculated for each calcification and used for statistical analysis.

5.7.2 Brain phase imaging (II)

The phase data from the T_2^* phantom and *ex vivo* rat brains were analyzed with ROIs using Aedes. The phantom ROIs were drawn to the center of the tubes avoiding partial voluming from the edge of the tubes. Various brain areas expressing strong phase contrast were chosen for the ROI analysis.

5.7.3 Thalamocortical pathway after TBI (III)

The thalamocortical pathway in rat LFPI model of TBI was analyzed from the cortical layers to the thalamus. The cortex and the external capsule were analyzed using a profile approach, whereas the subcortical areas were analyzed using ROIs. The profile analysis concentrated on the barrel cortex of the primary somatosensory cortex as it was outside the primary lesion, visually intact according to conventional MRI, but known to be affected by the secondary damage based on the experience from prior experiments with the same model. The profile analysis included the cortical layers and the external capsule, whereas the ROI analysis included the striatum, globus pallidus, internal capsule and thalamus including the ventral posteromedial and ventral posterolateral nuclei.

For the MRI data, the profiles were drawn starting from the external capsule and the cortical layers to the pia surface on horizontal slices. The profiles were orthogonally averaged over 1 mm, parallel to the cortical layers. This was repeated on 3 slices for *ex vivo* SWIFT, 2 for *in vivo* SWIFT and 3 for *ex vivo* DTI. Individual profiles were normalized to a length of one and spline interpolated to contain 100 points. The normalized profiles were then averaged ipsilaterally or contralaterally per animal, to represent an individual animal. For analysis and visualization, the individual layers needed to be distinguished in the normalized profiles. Since in MRI, the layers consisted of only a few pixels, it was not possible to separate them when drawing the profiles. Hence, the thickness of each layer in the normalized profiles was estimated based on histology (see below), where individual layers are easily separated.

For histology, the quantitative analyses were only repeated for Nissl and myelin stainings. It was thought that patchy iron deposits would be averaged out in the profile or ROI analysis. The profiles were divided into seven segments consisting of the external capsule and cortical layers VIb-I, with layers III and II analyzed together. The profiles were drawn on grayscale images of

three consecutive 1-in-5 horizontal sections taken at 2.5x magnification. Each segment was drawn individually. The normalized length of each segment was averaged over the Nissl stained sections of the sham animals to be (from external capsule to layer I): 0.13, 0.09, 0.22, 0.22, 0.13, 0.14 and 0.07, their sum equaling one. Each segment of the individual profiles was normalized to these proportions and interpolated so that the full profile consisted of 2000 points. These segment lengths were also used to estimate the layers in the MRI profile analysis. Finally, the profiles were averaged per animal as for MRI. Layer I was used as a control area for the histology profiles and ROIs (five circular ROIs per section, 30 μm for Nissl and 60 μm for myelin) to take into account different staining backgrounds by normalizing the gray scale values of the profile so that profile value = $(Profile_{ref} - Profile_{area})/Profile_{ref}$. The profiles measured from the myelin stained sections were further normalized by dividing them with their own average to remove the remaining baseline differences.

ROIs of the subcortical structures were drawn on areas through which the thalamocortical pathway traverses. The ROIs were divided in half (except for thalamus) by drawing a line from the center of the internal capsule, since early in the analysis, it was noticed from histology that the TBI induced damage was more severe closer to the injury. It was also noticed that the most caudal analyzed area of the internal capsule was clearly the most badly damaged, and hence a third ROI was placed inside the second, caudal internal capsule ROI (see Figure 9 in section 6.3.1). For MRI, the ROIs were drawn on horizontal slices starting from the dorsal internal capsule to a depth of 4 (*in vivo* SWIFT and DTI) or 6 (*ex vivo* SWIFT) slices in sham animals and in the contralateral side of TBI animals, and 2 (*in vivo* SWIFT and DTI) or 3 (*ex vivo* SWIFT) slices in the ipsilateral side of the TBI animals. For histology, three consecutive sections were used for the ROI analysis, taking care that the sections matched the MRI as well as possible. Layer I was used as a reference as for the profile analysis.

The profiles were drawn using ImageJ (NIH, http://imagej.nih.gov/ij/) for both MRI and histology. The ROI analysis of MRI was conducted using Aedes and for histology by using ImageJ.

5.7.4 Statistical comparisons (I, III)

The difference between gliosis scoring surrounding hypointense and hyperintense calcifications was tested with Mann–Whitney U-test (**I**).

For the profiles analysis results of study **III**, the average values the layers were compared using Mann–Whitney U-test between TBI and sham animal groups, and with Wilcoxon signed-rank test within group between ipsilateral and contralateral cortices. For the results of the ROI analysis, the comparisons were made similarly with the same tests for each ROI.

6 Results

SWIFT phase contrast was applied to detect the presence of calcifications after two types of brain insults and for imaging structures of a healthy brain in studies **I** and **II**, respectively. Study **III** used the SWIFT magnitude contrast for MT imaging the thalamocortical pathway of the barrel field in the primary somatosensory cortex after a TBI.

6.1 SWIFT MAGNITUDE AND PHASE CONTRAST OF CALCIFICATIONS (I)

6.1.1 Theoretical predictions and the glass bead phantom

Some theoretical work was conducted in study **I**. Based on the signal equation (Eq. 18), the SWIFT k-space due to a dipole field in a homogeneous background can be approximated as

$$s(r_k, \theta_k, \phi_k) \approx \delta(r_k) + i\frac{16\pi}{3}\frac{\Delta f_0}{\gamma|G|} r_k(3\cos^2\theta_k - 1)/2, \quad (33)$$

where (r_k, θ_k, ϕ_k) are the spherical coordinates of the k-space, Δf_0 is the strength of the dipole in Hz at a distance r_0 from the center of the dipole at an angle 0° to B_0 and $|G|$ is the readout gradient amplitude. Eq. (33) shows how the phase at the center of k-space due to the dipole field is zero, since SWIFT acquisition always starts from the center of k-space. This acts as an intrinsic high-pass filter for the phase images. It can also be deduced from Eq. (33) that the stronger the readout gradient, the less phase accumulation there is in k-space, as also shown for UTE (Carl & Chiang 2012). This can further be related to the more intuitive acquisition time, as in study **II**.

In the SWIFT phase image, the dipole field due to the glass bead was displayed as being much sharper and without phase wrapping as opposed to the GRE phase image as shown in Figure 2A, B. Although the theoretical prediction above is an approximation and is not accurate close to the center of the dipole, an excellent match to the phantom data was acquired at the regions of predicted accuracy. Since the signal shift or "pile-up" ended 5 pixels from the center in the magnitude image, the dipole strength could be estimated to match the pixel frequency resolution (81 Hz) at this distance. The "pile-up" is a misplaced signal due to the dipole field which, however, is not lost due to decreased T_2^* since SWIFT has a minimal acquisition delay. The border of the "pile-up" reflects a point where the frequency shift is smaller than the pixel frequency resolution.

6.1.2 Detecting calcifications using SWIFT phase contrast

In vivo calcification detection using SWIFT phase contrast was demonstrated in rat brain in a chronic time point after TBI. Three out of five animals had a single large MRI detectable calcification ipsilaterally in the thalamus, one had a calcification seen only in histology and one animal did not display any evidence of calcification. The calcifications were composed of multiple smaller granules. Qualitatively, the calcifications of the TBI animals were detected equally well *in vivo* and *ex vivo* in SWIFT phase images, although it also seemed that the imaginary component of the image gave a better contrast than the actual phase images. The calcifications could be separated from veins, bleedings and air bubbles (*ex vivo*) based on the orientation of the dipole, since the former is diamagnetic and the latter are paramagnetic in comparison to water.

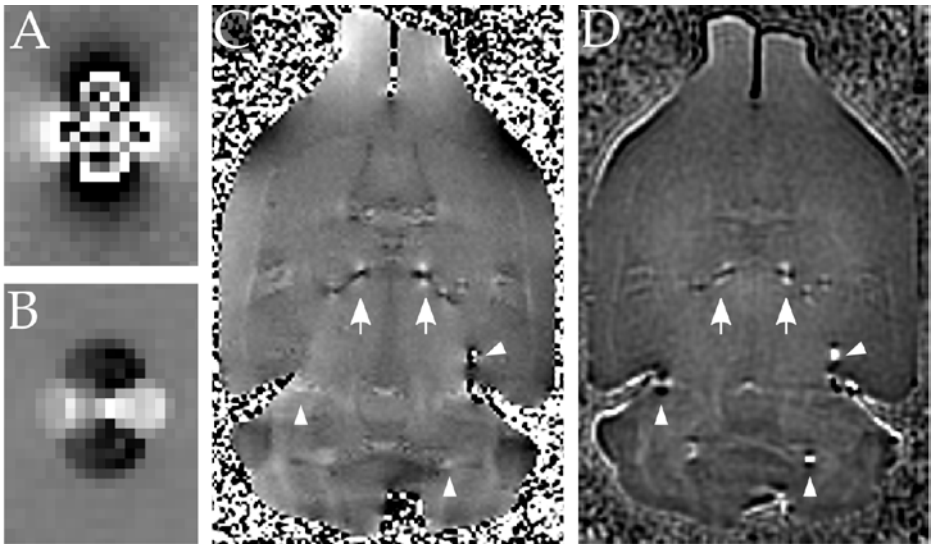

Figure 2. Dipole field in GRE and SWIFT phase images (**I**). Dipole field induced by a glass bead in agar gel as shown by (A) GRE phase (TE = 5.0 ms) and (B) SWIFT phase (T_{acq} = 8.1 ms). Dipole fields induced by brain calcifications (arrows) and air bubbles (arrow heads) in an *ex vivo* rat brain, as shown by (C) GRE (TE = 1.9 ms) and (D) SWIFT (T_{acq} = 4.1 ms).

The pilocarpine injected animals were imaged only *ex vivo*. These animals expressed varying amounts of calcifications bilaterally in the thalamus (Figure 2C, D; Figure 3A, B). The phase due to the calcification dipole fields were seen both with SWIFT and GRE. SWIFT detected some dipoles from air bubbles that were unseen by GRE (Figure 2C, D). The magnitude contrast of SWIFT and GRE were similar; a signal void was seen at the location of the calcification, but SWIFT had a clear signal "pile-up" surrounding the void. Interestingly, two types of

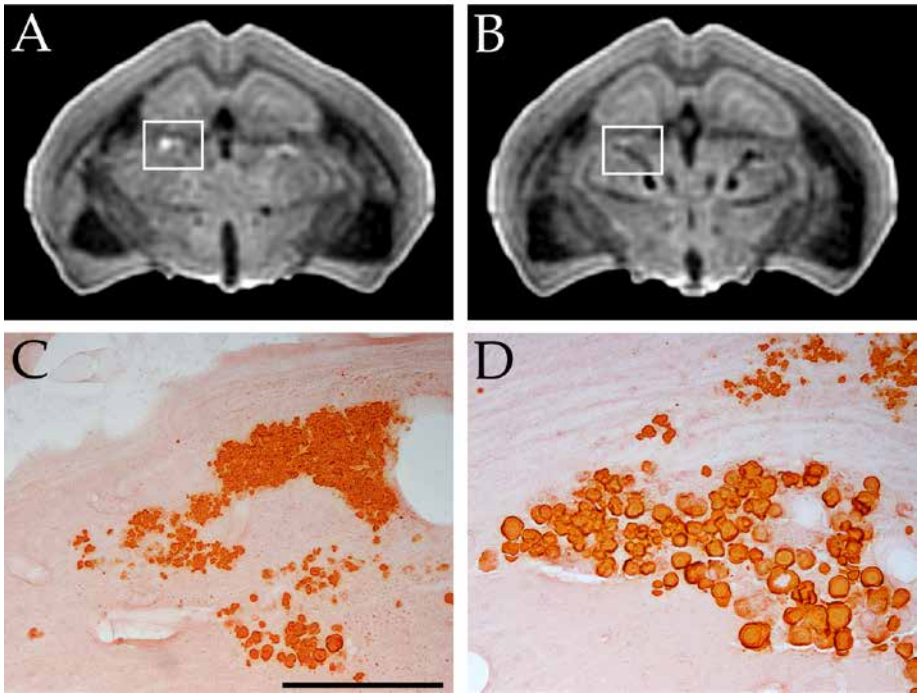

Figure 3. Representative images of the two stages of the calcifications in the pilocarpine-treated animals (**I**). SWIFT magnitude showing the (A) hyperintense and (B) hypointense calcification and (C, D) their Alizarin stained sections, respectively. Scalebar 300 μm.

calcifications were detected in the pilocarpine animals: hypointense with a signal void as described before (Figure 3B), and hyperintense with no signal void but a positive contrast in the magnitude images (Figure 3A). Four out of five pilocarpine-treated animals exhibited both types of calcifications, TBI animals only had hypointense calcifications.

6.1.3 Histology of the calcifications

The Alizarin stained sections of the brains of the pilocarpine-treated rats revealed a clear structural difference between the hypointense and hyperintense calcifications: the former were composed of relatively larger crystalized granules (Figure 3D) whereas the later were formed of larger quantity of small granules (Figure 3C). Both types of calcifications were surrounded by astrocytes and microglial cells as detected in the GFAP and OX42 stainings, respectively. However, based on the semi-quantitative scoring, the hyperintense calcifications were surrounded by more intense gliosis (p_{GFAP} = 0.013, p_{OX42} < 0.001). The scores for the astrogliosis and microgliosis around hypointense calcifications in rats with TBI were 1.71 ± 0.49 and 1.57 ± 0.53, respectively. The scores for hypointense calcifications in the status epilepticus model were comparable, being 1.73 ± 0.45 for the astrogliosis and 1.38 ± 0.54 microgliosis. The scores for the hyperintense calcifications were 2.40 ± 0.97 for astrogliosis and 2.81 ± 0.40 for microgliosis.

The correlations between the calcification sizes approximated from the *ex vivo* SWIFT magnitude images and Alizarin stained sections were moderately good, being r = 0.72 (p < 0.001) for the hypointense calcifications and r = 0.82 (p < 0.001) for the hyperintense calcifications.

6.2 SWIFT PHASE CONTRAST OF BRAIN STRUCTURES (II)

An excellent correspondence between T_2^* MnCl2 phantom and the virtual phantom was seen with different acquisition times and different relative object sizes. It was shown that the SWIFT phase in the tubes averaged over the ROIs increased slightly with decreasing T_2^* in both cases. As expected, phase increased with increasing acquisition time and also with decreasing the relative object size. In addition, simulations were conducted in a "WM stripe", representing a narrow WM structure (Figure 4A). Phase contrast was shown to be dependent on the magnitude contrast so that phase contrast can reverse sign if the "WM" signal amplitude is lower or higher than in "GM" (Figure 4B). By simulating a decreasing T_2^* in the "WM stripe", its phase was first shown to increase and then decrease with decreasing T_2^* (Figure 4C). However, compared to maximum phase in the "WM" stripe (0.13 rad with a 0.25 pixel shift), with a T_2^* of 0.1*T_{acq}, the phase was still considerable (0.08 rad) with the object dimensions used in the simulation ("WM" width 3 pixels). The magnitude dependence is further demonstrated in Figure 5 with two different "GM" amplitudes and a global offset of 0.25 pixels: the "GM" has an imaginary component inside "WM" (Figure 5B) which affects the overall phase (Figure 5D).

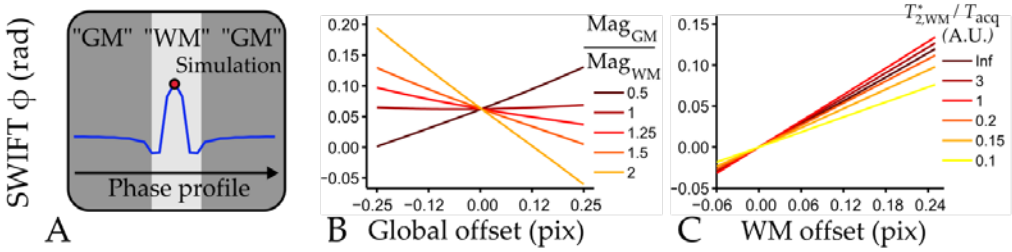

Figure 4. Simulation results of a 3 pixel wide "WM strip" (0.125 pixel offset, T_2^*/T_{acq} = 3) surrounded by "GM" (0 pixel offset, T_2^*/T_{acq} = 4) (**II**). (A) Sketch of the simulation, the effect of (B) magnitude contrast with added global offset, and (C) decreasing T_2^* relative to T_{acq} on SWIFT phase of "WM".

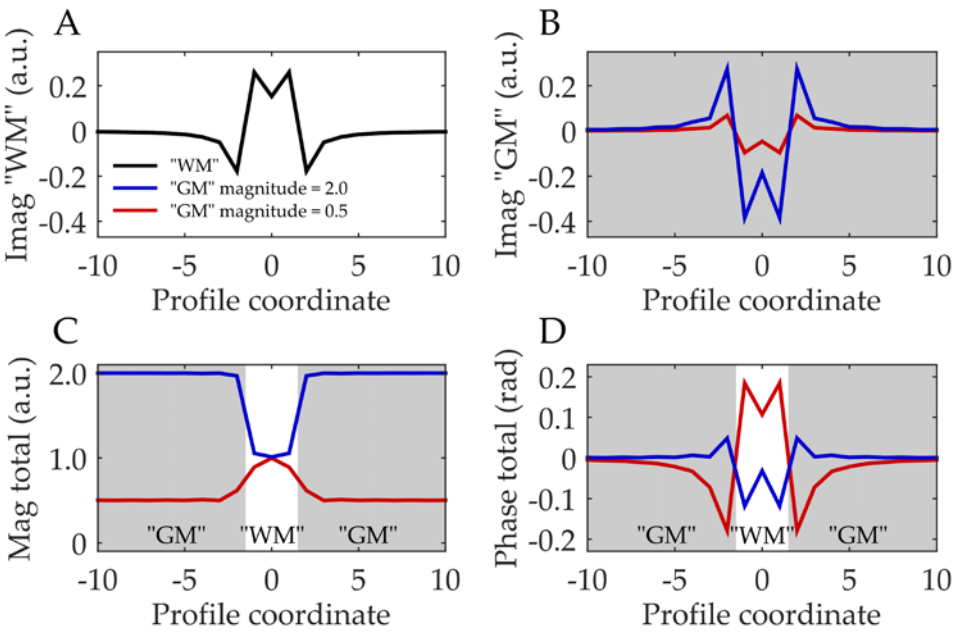

Figure 5. A closer look into the effect of magnitude contrast on phase contrast in presence of a global offset (**II**). The imaginary component of only (A) "WM" and (B) "GM", and (C) the magnitudes of the complete profiles and (D) the corresponding phase profiles. The simulation parameters match that of Figure 4B with "GM" magnitudes 2.0 and 0.5 and a global offset of 0.25 pixels.

Imaging a perfused rat brain in different orientations to B_0, with SWIFT and MGRE3D, revealed very similar phase/frequency behavior. Pooling together data from various brain structures, the Pearson correlation between SWIFT and MGRE3D was $r^2 = 0.95$ ($p < 0.001$). The largest variation in contrast was seen in the lateral ventricle. Naturally, this does not have an anisotropic microstructure, but has a flat macrostructure perpendicular to the horizontal plane of the brain, and it also likely has a bulk susceptibility difference compared to the surrounding brain structures. As in the case of calcifications, even without post-processing, SWIFT did not display phase wrapping and very little bulk susceptibility related large scale phase variation as opposed to MGRE3D.

The acquisition time analogy to TE in SWIFT phase imaging was further shown in a perfused rat brain (Figure 6): e.g. doubling acquisition approximately doubled the phase in various WM structures. The strongest phase was seen in the fimbria (T_{acq} = 6.14 ms, φ = -0.08 rad; T_{acq} = 12.29 ms, φ = -0.2 rad). In MGRE3D, the strongest phase accumulation was seen in the optic tract (TE = 2.76 ms, φ = -0.04 rad; TE = 22.23, φ = -0.58 rad), whereas the same structure in SWIFT hada considerably smaller phase (T_{acq} = 6.14 ms, φ = -0.05; T_{acq} = 12.29 ms, φ = -0.13 rad) compared to the fimbria.

When the MT preparation was used, SWIFT phase decreased (increase in absolute phase) in all the analyzed areas except in the mammothalamic tract, where phase increased (decrease in absolute phase, Figure 6D-F). The largest decrease in SWIFT phase was seen in the optic tract (T_{acq} = 12.29 ms, before MT φ = -0.13 rad and after MT φ = -0.19 rad). The largest change in MGRE3D measure frequency was in the fimbria (TE = 22.23 ms, before MT f = -3.5 Hz and after MT φ = -2.9 Hz), whereas the optic tract essentially did not change (TE = 22.23 ms, before MT f = -4.1 Hz and after MT φ = -4.0 Hz).

An apparent increase in non-linearity of relative phase accumulation was seen for SWIFT phase after applying the MT preparation (Figure 6D, E) so that from T_{acq} = 9.22 ms to T_{acq} = 12.29, the increase in absolute phase was much smaller than from T_{acq} = 6.14 ms to T_{acq} = 9.22 ms. An attempt was made to explain this behavior by conducting a two-pool simulation of a

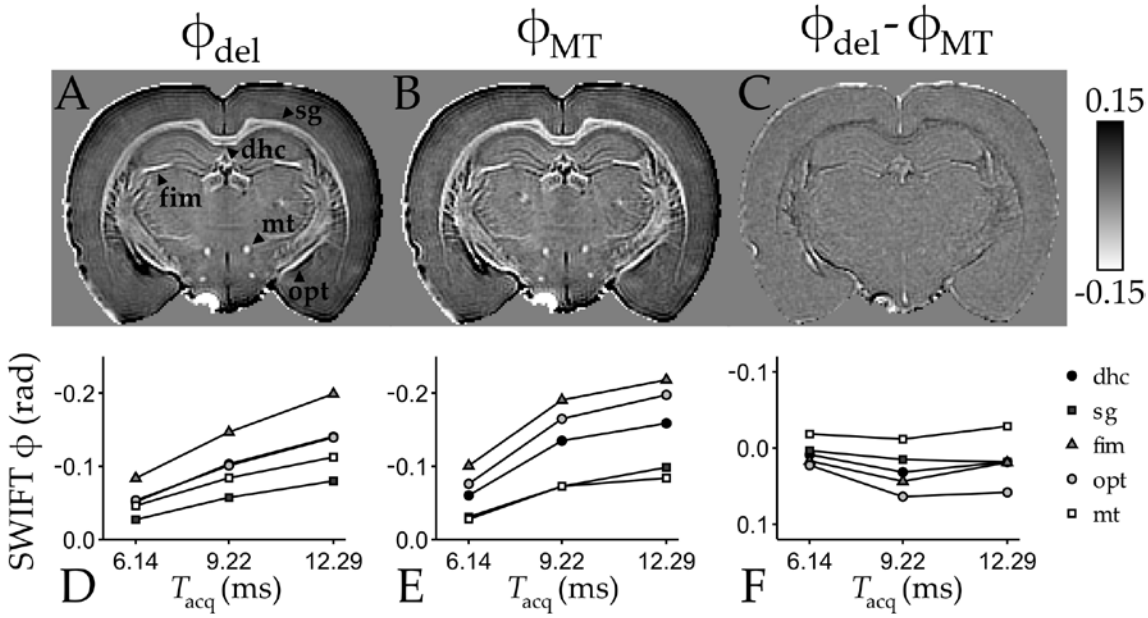

Figure 6. SWIFT phase imaging of an *ex vivo* rat brain with different acquisition times (**II**). Representative phase image (A) without an MT preparation, (B) with an MT preparation, (C) the difference (T_{acq} = 12.29 ms), and (D-F) the quantitation of selected white matter areas, respectively.

WM strip with and without a short T_2^* component with a opposite signed frequency shift. Simulation behavior was seen to be similar to the experimental data.

Interestingly, with the same MT preparation and as similar imaging parameter as possible, MTR with SWIFT was consistently higher. The MTR difference to MGRE3D was between 0.04 and 0.07. At SW = 20.8 kHz, the difference was even higher, but as the other two SWs showed approximately equal but lower MTRs, this even higher difference was considered as artefactual.

The SWIFT phase contrast of the human brain sample again showed similar features to MGRE3D phase images. SWIFT phase was seemingly more blurred in comparison to MGRE3D. Interestingly, inside WM, much detail was seen as dipole-like features that may be associated to individual fiber bundles. Orientation dependent contrast was seen in the U-fibers.

Finally, a rat brain was imaged *in vivo* for SWIFT phase contrast. This was achieved, but admittedly the contrast was surprisingly weak. However, major WM structures were detectable.

6.3 MTR VS. DTI AFTER TRAUMATIC BRAIN INJURY (III)

6.3.1 MRI of the thalamocortical pathway after TBI

In vivo MT SWIFT showed clear differences in MTR between the ipsilateral and contralateral barrel cortex of the TBI animals, and between the TBI and sham operated animals. A noticeable decrease in MTR was seen in the external capsule, and layers VIb and VIa. *Ex vivo* results were similar (Figure 7): MTR was shown to be decreased from the external capsule until layer IV in ipsilateral TBI (Figure 7E). The *in vivo* MTR percentage reductions in the external capsule, and layers VIb and VIa, ipsilateral TBI vs. ipsilateral sham, were: -6.4%, $p < 0.005$; -5.8%, $p < 0.005$ and -3.5%, $p < 0.005$. In the *ex vivo* experiment, the corresponding MTR reductions in the external capsule and layers VIb-IV were: -6.3%, $p < 0.005$; -8.1%, $p < 0.005$; -6.2%, $p < 0.005$; -4.1%, $p < 0.005$ and -3.5%, $p < 0.05$.

In the ROI analysis of the subcortical areas, *in vivo* MTR was significantly decreased only in the caudal internal capsule (ipsilateral TBI vs. ipsilateral sham: -6.8%, $p < 0.005$) and more so in the most caudal analyzed internal capsule (ipsilateral TBI vs. ipsilateral sham: -9.3%, $p < 0.005$).

The *in vivo* data was more variable than the *ex vivo* data based on standard deviation over the animals and ROIs. *Ex vivo* (Figure 8A, C), statistically significant reductions in MTR were seen in all the analyzed subcortical areas (Figure 9A), the caudal internal capsule having the largest decrease (ipsilateral TBI vs. ipsilateral sham: -7.5%, $p < 0.005$), and as *in vivo*, more so in the most caudal analyzed internal capsule (ipsilateral TBI vs. ipsilateral sham, -11.0%, $p < 0.005$).

DTI was only conducted *ex vivo*, since at least at the time, high resolution 3D *in vivo* DTI was not feasible in rats. Overall, DTI data was much more variable than MTR. In the profile analysis of the barrel cortex (Figure 7C, D, F), the only statistically significant differences were found to be a decreased FA in the external capsule (ipsilateral TBI vs. ipsilateral sham: -17.8%, $p < 0.05$) and an increased FA in layer VIa (ipsilateral TBI vs. ipsilateral sham: 40.0%, $p < 0.05$) when comparing ipsilateral TBI to ipsilateral sham animals. These FA changes were likely related to the decreased AD and increased RD in the external capsule, and increased AD in layer VIa, though none of these changes were statistically significant.

ROI analysis results of the DTI metrics in the subcortical areas (Figure 8B, D; Figure 9B) mirrored the profile analysis by also being very variable. In ipsilateral TBI as compared to contralateral TBI, FA increased in the caudal striatum (26.8%, $p < 0.05$), rostral internal capsule (32.5%, $p < 0.05$) and the thalamus (8.5%, $p < 0.05$). These FA increases were related to the increased AD in these areas (ipsilateral TBI vs. contralateral TBI: 7.4%, $p < 0.05$; 15.8%, $p < 0.05$; 14.6%, $p < 0.05$, respectively), and to decreased RD seen in the rostral internal capsule (ipsilateral TBI vs. contralateral TBI: -24.8%, $p < 0.05$) and thalamus (ipsilateral TBI vs. ipsilateral sham: -8.77%, $p < 0.05$). AD was also increased in the caudal globus pallidus (ipsilateral TBI vs. ipsilateral sham: 2.2%, $p < 0.05$). Interestingly, the most caudal internal capsule showed evidence of opposite behavior when compared to the rostral part, with an increased RD instead of decreased RD (ipsilateral TBI vs. ipsilateral sham: 19.3%, $p < 0.05$).

6.3.2 Histology of the thalamocortical pathway after TBI

The histological comparison was an essential component of this work, since it was intended to describe what kinds of changes in the tissue the MRI results were actually indicating. According to the Nissl staining, increased cell density was seen throughout the cortical layers, more so in the deep layers. The external capsule expressed the highest increase in cell density which was also verified by the quantitative profile analysis (ipsilateral TBI vs. ipsilateral sham, $p < 0.05$) at the same time being the only statistically significant result. This increased cell density can be

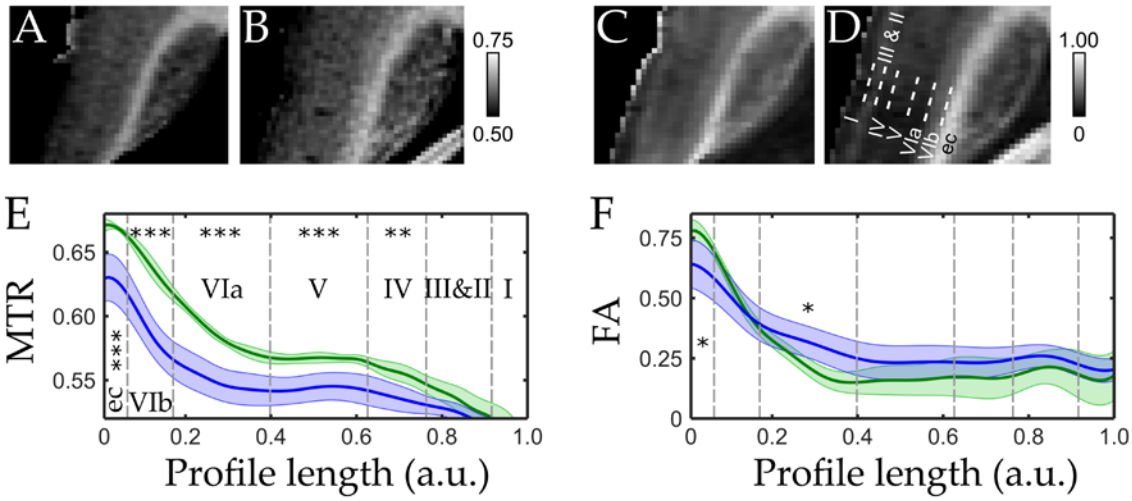

Figure 7. Ex vivo MTR and FA profile analysis of the barrel cortex (**III**). (A, B) MTR and (C, D) FA maps of representative ipsilateral cortices of TBI and sham operated animals, respectively, and (E, F) the results of the profile analysis of MTR and FA, respectively. The thick lines represent the mean profile and the shaded area displays the standard deviation at each point. *$p < 0.05$, **$p < 0.01$, *** $p < 0.005$.

related to gliosis based on the cell size and organization of the cells (oligodendrocytes tend to form lines) as observed by an expert in histology. Hence, gliosis was situated in the same areas in the barrel cortex as the MTR decrease, and also partly where FA had changed.

In the subcortex, Nissl revealed extensive gliosis throughout the analyzed areas which was also confirmed by the quantitative ROI analysis: ipsilateral TBI had a statistically significant ($p < 0.05$) increase in each ROI in comparison to contralateral TBI. The most caudal analyzed internal capsule had the most extensive gliosis. As in the cortex, these results coincided with decreased MTR in all areas, and also with areas with changes in the DTI metrics. Although not statistically significant, the ipsilateral subcortical areas of the sham animals also seemed to have some gliosis.

Myelin stained sections showed a qualitative decrease in the numbers of myelinated axons in the external capsule and layers VIb-II. The quantitative profile analysis verified these observations in layer VIb. The variability of the myelin profile data was rather strong. Myelin

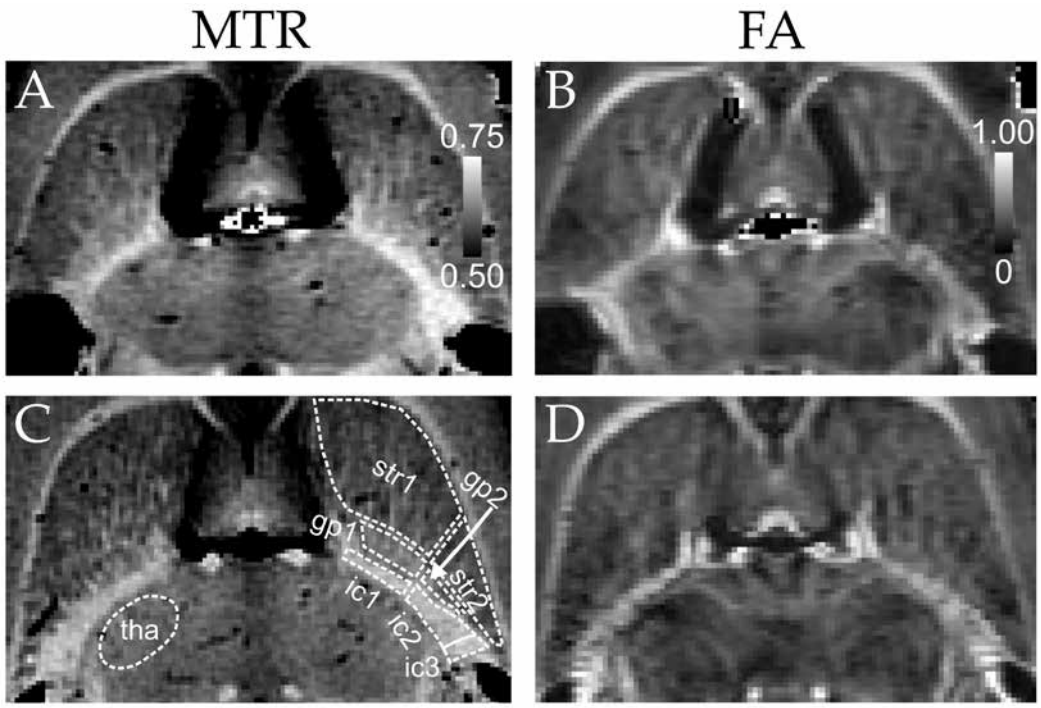

Figure 8. Subcortical areas included in the ROI analysis (**III**). Representative MTR and FA maps of (A, B) a TBI and a (C, D) sham operated animals. ROIs are demonstrated in (C). Abbreviations: str = the striatum, gp = the globus pallidus, ic = the internal capsule and tha = the thalamus.

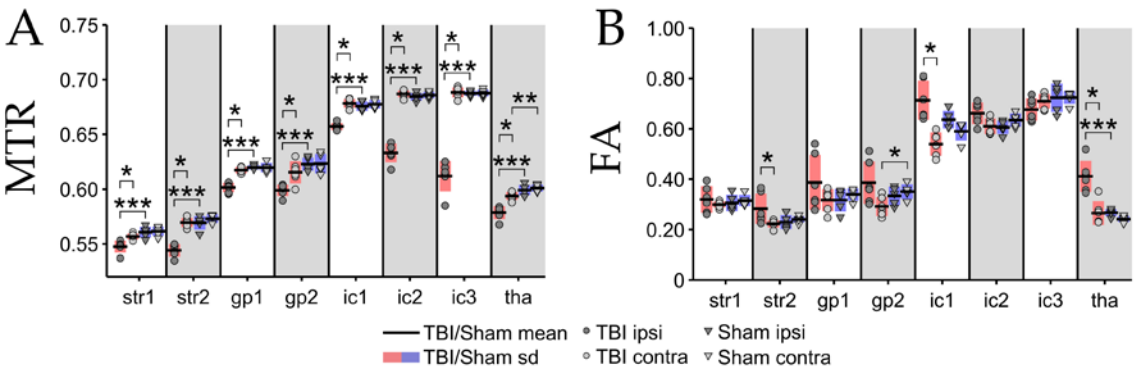

Figure 9. Ex vivo (A) MTR and (B) FA ROI analysis results of the subcortical areas of the TBI and sham operated animals (**III**). *p < 0.05, **p < 0.01, ***p < 0.005.

loss seemed to match well with the decrease in MTR in the barrel cortex. A possible connection to DTI was less evident as the FA change in the external capsule and in layer VIa was in opposite directions.

An extensive loss of myelinated axons was seen in the analyzed ipsilateral subcortical areas of the TBI animals as compared to contralateral and sham animals. The lowest myelin densities were seen in the caudal areas of the internal capsule as confirmed by the quantitative ROI analysis (ipsilateral TBI vs. ipsilateral sham, $p < 0.005$). Other regions did not reveal any statistically significant differences, although qualitatively the difference was clear, matching with the decreased MTR.

Perls' staining showed two types of pathological iron accumulation in the barrel cortex: iron from old bleeds or possible blood brain barrier leakage often inside glial cells, and diffuse iron accumulation in the damaged tissue. These were only seen in TBI animals in the external capsule and layers VIb-V. The semi-quantitative scoring revealed a statistically significant difference between ipsilateral and contralateral barrel cortices of the TBI animals (ipsilateral 1.8 ± 0.8 vs contralateral 0.2 ± 0.4, $p < 0.005$).

There was also a considerable iron accumulation in the analyzed subcortical areas. The iron accumulation was stronger in the ipsilateral subcortical areas of the TBI animals, although there was also some diffuse iron accumulation in the contralateral striatum, globus pallidus and internal capsule. The ipsilateral iron accumulation was worse in the caudal halves of the subcortical areas. The iron was mainly concentrated inside the fiber bundles, displaying both cellular and diffuse accumulation. In thalamus, diffuse iron followed the fiber bundles, whereas the cellular iron deposits were scattered in both GM and WM. The semi-quantitative scoring verified ipsilateral subcortex of the TBI animals to have greater iron accumulation than the contralateral cortex, or the sham operated animals (ipsilateral 2.0 ± 0.9 vs contralateral 0.8 ± 0.4, $p < 0.005$).

Hence, overall, the ipsilateral hemisphere of the TBI animals showed clear gliosis and loss of myelinated axons, and both hemispheres had some pathological iron accumulation. In sham operated animals, mild gliosis was seen in the ipsilateral hemisphere. These three mesoscopic consequences of the TBI pathology were seen as the most likely contributors to the MRI metrics, and based on the results, the connection seems feasible.

Table 6. Pearson correlation between MTR, DTI metrics and histology based on the pooled subcortical ROI analysis results, separately in ipsilateral and contralateral TBI or Sham groups.

		Ipsilateral TBI		**Contralateral TBI**		**Ipsilateral Sham**		**Contralateral Sham**	
		r^2	p	r^2	p	r^2	p	r^2	p
MTR	Nissl	0.318	0.146	0.028	0.689	0.003	0.900	0.039	0.640
	Myelin	**0.937**	**<0.001**	**0.989**	**<0.001**	**0.979**	**<0.001**	**0.990**	**<0.001**
FA	Nissl	**0.706**	**0.009**	0.002	0.917	0.003	0.901	0.028	0.693
	Myelin	**0.589**	**0.026**	**0.833**	**0.002**	**0.779**	**0.004**	**0.810**	**0.002**
AD	Nissl	**0.760**	**0.005**	0.000	0.979	0.000	0.976	0.035	0.656
	Myelin	**0.495**	**0.052**	**0.807**	**0.002**	**0.732**	**0.007**	**0.819**	**0.002**
RD	Nissl	**0.670**	**0.013**	0.008	0.836	0.006	0.858	0.023	0.723
	Myelin	**0.587**	**0.027**	**0.822**	**0.002**	**0.791**	**0.003**	**0.758**	**0.005**

6.3.3 Correlation between MRI and histology

Finally, the contributions of myelin and cell density—including gliosis—to the MRI metrics were assessed using linear correlation for the subcortical ROI analysis results. When the MTR of all ROI results were pooled together and averaged over the animals, an excellent correlation (Pearson $r^2 = 0.94$, $p < 0.001$) was found with the corresponding myelin quantification. Statistically significant but much weaker correlations were found for FA, AD and RD ($r^2 = 0.60$, $p < 0.001$; $r^2 = 0.63$, $p < 0.001$; $r^2 = 0.48$, $p < 0.001$, respectively).

When using all the data, no correlation was found between MRI and Nissl staining. However, when dividing the data into four subgroups of ipsilateral and contralateral TBI and

sham, FA, AD and RD correlated with Nissl in the ipsilateral TBI ($r^2 = 0.71$, $p = 0.009$; $r^2 = 0.76$, $p = 0.005$; $r^2 = 0.67$, $p = 0.013$, respectively), but not in other subgroups. DTI metrics correlated with myelin staining considerably better in subgroups other than ipsilateral TBI. The subgroup correlations are shown in Table 6. MTR did not correlate with Nissl staining at all.

7 Discussion

So far, SWIFT and other similar almost zero TE pulse sequences, have been mainly applied in musculoskeletal imaging where tissues like bone and tendon are problematic for their fast decaying signal. Hence, in this field of imaging, these pulse sequences find obvious applications. On the other hand, almost zero TE sequences have not been used extensively in brain imaging, since the MRI usable signal has been seen to mainly consist of relatively long T_2^* components. The goal of this thesis was to find new applications for SWIFT in brain.

Studies **I** and **II** concentrated on the not-so-intuitive phase contrast of SWIFT to detect brain calcifications since these are fairly strong field perturbers, and further to study the WM-GM phase contrast based on their minute resonance frequency difference. Study **II** also aimed to clarify how SWIFT phase contrast would behave as it has no echoes and it is radial in its nature. In study **III**, the focus switched to SWIFT magnitude contrast as a way of describing mild changes in the brain due to the secondary injuries after a TBI. Since SWIFT is much less affected by a short T_2^* decay than conventional sequences, it was decided to concentrate on MT contrast free of T_2^* weighting. MT SWIFT was then compared to DTI, a very promising brain imaging tool in itself, and finally the MRI results were elucidated with extensive histologic analysis.

7.1 ON SWIFT PHASE CONTRAST (I, II)

The effect of off-resonance signal on MRI signal, and hence FIDs, has been acknowledged from the beginnings of MRI (Kumar et al. 1975, Likes 1981, Brown et al. 1982). However, the actual exploitation of this phenomenon in structural brain imaging was acknowledged only fairly recently (Duyn et al. 2007), and for FID based imaging, there are only a very limited amount of studies of any kind (Carl & Chiang 2012, Zhou et al. 2010) outside this thesis (**I**, **II**). Phase imaging has almost unambiguously been related to GRE-based imaging so that the amount of phase accumulation is related directly to TE.

In GRE, phase due to off-resonant signal accumulates throughout the k-space traversal. This effect can be decomposed into linear shift in image space due to linear phase accumulation in k-space, and a constant phase component defined at TE producing the desired phase contrast. SWIFT is effectively an FID based pulse sequence. Hence, the acquisition always starts at the center of the k-space and the phase of signal due to off-resonance starts from zero, increasing towards higher spatial frequencies. This can be seen to be similar to a full SE acquisition, where phase decreases towards zero at the center of k-space leading to a linear shift in image space. However, in SWIFT, the accumulating phase always has the same sign regardless of the direction of the k-space line. This can be interpreted to cause a shift to opposite directions in opposite spokes in the image space. Hence, the imaginary components ("dispersion spectrums" (Levitt. 2001)) of the inverse Fourier transformed individual spokes do not cancel out each other, leading to a residual imaginary component proportional to the frequency shift. This can be considered as the source for the phase contrast of SWIFT.

Because of the center-out phase accumulation, higher spatial frequencies accumulate more phase. This means that the SWIFT phase is dependent on the spatial frequency content of the structure, or, in other words, the contrast depends on the geometry of the structure. Thus, narrow or point-like structures will have a higher phase than broad, smooth objects with the same off-resonance. This center-out phase accumulation leads to an intrinsic high-pass filtering property so that phase wrapping does not appear as readily GRE, or that larger scale field fluctuations have less of an effect than in a raw GRE phase. This removes the need for the post-processing steps usually needed with GRE (Haacke et al. 2009).

A common analysis for MRI pulse sequences or in any measurement system where linear systems theory can be applied, is the point spread function (PSF) analysis. This provides insights into the way that the pulse sequence modifies the ideal image due to finite sampling, k-space trajectory etc. and also possibly how the off-resonance signal is reflected in the image phase. In the review process of study **II**, PSF was also solved in 3D for post-correlation SWIFT, but the result was complicated and thus not very informative. In addition, since a PSF describes the behavior of an object with the maximal spatial frequency content, a delta function, a PSF analysis was deemed not to be an intuitive descriptor of SWIFT phase contrast. Hence, study **II** was made more descriptive than mathematically rigorous.

An off-resonant delta function is able to exhibit maximal phase in SWIFT. The opposite of this is a constant object covering the entire FOV of which FT is a delta function. Since its FT covers only the center of the k-space, no phase contrast should be seen due to off-resonance. On the other hand, in study **I,** the phase due to a point dipole inside a constant object was studied in theory and in a phantom. One can see that phase contrast is still possible by observing the first two terms of the Taylor series expansion of the off-resonance exponential used in study **I**:

$$e^{-i2\pi\Delta f(\boldsymbol{r})t} = 1 - 4\pi^2\Delta f'(\mathbf{0})\Delta f(\boldsymbol{r})te^{-i2\pi\Delta f(0)t} + \cdots \quad (34)$$

IFT of the first term describes the constant background and the possible phase is induced by the higher order terms. Now, if the off-resonance field $\Delta f(\boldsymbol{r})$ is constant or it is smooth, slowly varying over the object; its first and higher order derivatives are zero or can be approximated to be zero, respectively. Since the dipole field changes initially rapidly and then much slower (inversely proportional to the distance cubed), this explains why a dipole field is seen with a sharper boundary in SWIFT phase than in GRE. This also further demonstrates how large scale field fluctuations are removed by the intrinsic high-pass filtering property.

Since SWIFT, after correlating the raw data with the RF pulse, is similar to UTE and ZTE, it is likely that the phase behavior is similar. Hence, the results of studies **I** and **II** most likely will also apply to these pulse sequences as well. UTE likely suffers more from an off-resonant signal in the form of wrapping, since the readout gradient is raised after the excitation. In comparison to ZTE, the SWIFT phase should be the same, given that same imaging parameters can be used and the correlation process is perfect. Generally in the phase imaging sense, UTE has the benefit of the already implemented acquisition of consecutive echoes.

It should be noted that even though usually a full k-space line is acquired in SE acquisition, it is possible to do a radial implementation where only the first or second half of the echo would be used to form the k-space. In this case, the phase behavior would be very similar to SWIFT, although sensitivity to short T_2^* components would be lost due to a longer TE. For GRE, this kind of built-in-sequence phase behavior cannot be implemented, since phase is always accumulated during the excitation pulse and the prephasing lobe, and this phase is never subsequently nulled.

7.2 IMAGING CALCIFICATIONS WITH A MINIMAL TE (I)

7.2.1 Two types of calcifications detected by SWIFT

SWIFT phase contrast was first used to detect superparamagnetic nanoparticles in rat heart, *ex vivo* and *in vivo* (Zhou et al. 2010). Hence, it was hypothesized that SWIFT phase contrast would detect weakly diamagnetic calcifications formed as a result of a brain insult. In order to reveal the generalizability of SWIFT phase in this application, the contrast was demonstrated in two clinically important animal models of epilepsy: status epilepticus induced by pilocarpine injection and the LFPI TBI model.

Due to the diamagnetic nature of the calcifications compared to water, the calcifications were seen to induce dipole-like fields, even though histology clearly showed that a single calcification in reality consists of many granules. However, the individual granules were so

tightly packed together that their individual dipole fields do not considerably cancel each other out. An important factor was the orientation of the dipole: the sign is reversed for paramagnetic deposits, hence enabling differentiation of calcifications from brain microbleeds that contain an iron-protein complex, hemosiderin (Cordonnier 2011). Microbleeds are encountered in many brain diseases such as TBI (Scheid et al. 2003), ischemia (Cordonnier et al. 2007) and Alzheimer's disease (Cordonnier & van der Flier 2011), and they are often used as indicators of diffuse axonal injuries in MRI (Scheid et al. 2003).

Although almost all of the detected calcifications were seen as signal voids surrounded by signal "pile-up" in SWIFT magnitude images, the pilocarpine-treated animals also showed hyperintense calcifications. This hyperintensity was related to the T_1 shortening near the surface of the calcification as discussed in section 3.1.3. Importantly, the Alizarin staining revealed that the hypointense calcifications were composed of clearly bigger granules than the hyperintense calcifications. Since they have the same volume, the calcification composed of smaller granules has an overall larger surface area and thus also the calcification surface T_1 shortening effect is stronger. In combination with less displaced tissue or fluid in the midst of the small calcification granules, hyperintense magnitude contrast is seen without the signal void. Once the granules are large enough, the T_1 shortening effect decreases due to decreasing calcification surface area and also the intravoxel proton density decreases in the area of the growing calcifications, and finally the signal is displaced by the dipole-like field. Even though the brains were scanned only at a single time point, it was hypothesized that the hyperintense calcifications would evolve towards the hypointense calcifications. This type of evolution of the calcification has been shown previously after stroke (Mäkinen et al. 2007).

An important aspect of the hyperintense/hypointense calcifications was that clearly stronger gliosis was shown to surround the hyperintense calcifications, whereas in the older calcifications, gliosis was weaker as shown also by other studies (Gayoso et al. 2003, Nitsch & Scotti 1992, Oliveira et al. 2003). Intense gliosis is an indicator of a recent injury and the early stage of the calcification which means that it might serve as a marker of disease progression.

The calcification size was measured from SWIFT magnitude images and correlated with the size measured from the Alizarin stained sections. Considering the fact that the resolution of the two methods is very different, the correlations of hyperintense and hypointense calcifications with histology were reasonably good. SWIFT magnitude showed hyperintense calcifications as larger than their hypointense counterparts in comparison to histology. This was related to the surrounding gliosis which conferred a larger appearance on these structures. To be more precise, the surrounding of the detected macroscopic calcification is occupied not only by the glial cells, but likely also by calcium precipitates even smaller than those shown in Figure 3A for the hyperintense calcifications. The formation of calcifications in aqueous solutions has been shown to be biphasic (Barat et al. 2011): the first step produces amorphous calcium phosphate crystals, while the second steps leads to the formation of the more stable hydroxyapatite. As very small calcium deposits are not captured in the histologic quantitation, the size discrepancy between MRI and histologic analysis is enhanced. For the hypointense calcifications, the signal void—the marker for hypointense calcification size—was likely exaggerated by the signal shift due to the dipole-like field. Thus, it is possible that the more tightly packed calcifications covering the same volume as a loosely packed calcification, will appear larger, since it has a stronger dipole field.

The discrepancy between MRI and histology is likely mainly related to methodological differences as well as the resolution. Histological measure has the opportunity for microscopic precision, but at the same time, because of the granular shape of the calcifications, it is difficult to decide where the exact border of the calcification is and which parts of the calcification belong to the corresponding feature seen separately by MRI. In addition, although histology is precise on the plane of the section, this precision is largely lost perpendicular to the plane, since 1-in-5 30 μm sections are used. In other words, 120 μm out of 150 μm is left unknown for one staining.

The major parameter controlling the contrast of the calcifications was SW, or more precisely the pixel frequency resolution, SW/pixel. The higher the SW/pixel, the smaller is the signal shift because of the dipole and hence the more precise is the signal void as a measure of the calcification size. With respect to the magnitude image, a high SW/pixel is desirable as long SNR is adequate. On the other hand, the higher the SW/pixel, the shorter is the acquisition time and the less time there is for phase accumulation because of the dipole. For detection and separation of the calcifications or microbleeds using phase contrast, as long as the dipoles themselves can be detected, higher SW/pixel can also be beneficial because it effectively suppresses the phase contrast background from the brain tissue itself. Hence, the application of SWIFT to detect calcification and/or microbleeds becomes a compromise.

In this work, SW/pixel of 122 Hz (SW = 31250 Hz) was used *in vivo* and 244 Hz (SW = 62500 Hz) *ex vivo*. At the time, these were considered as a good compromise, however, with the improvements of the SWIFT pulse sequence and the reconstruction procedure that followed, SW/pixel could likely be increased. The practical upper limit of normal gapped SWIFT has been 488 Hz after which the ring down of most coils starts to contaminate the signal. Very high SWs can be achieved with multiband SWIFT (Idiyatullin et al. 2015).

7.2.2 Comparison to other methods

The closest work to SWIFT calcification imaging has been using UTE for carotid plaque calcification imaging (Du et al. 2011a). T_1 and T_2^* of intra-calcification water as short as 94 ms and 0.31 ms, respectively, were measured. This work used only magnitude contrast and long T_2^* components were suppressed by applying an 8.6 ms adiabatic inversion. The calcification was imaged with a relatively high SW of 125 kHz and the calcification covered multiple pixels. Since no signal voids were reported, the calcification is likely similar in structure as the hyperintense calcifications observed in study **I**. Without the inversion pulse, in normal UTE, the contrast was negative, which is likely related to the low water content of the carotid calcification (Du et al. 2011a). Otherwise, in a comparison to UTE, given the same SW/pixel in SWIFT acquisition and at the top of the UTE readout ramp, SWIFT does benefit from not having to ramp the readout gradient, leading to less blurring and also less signal loss due to short T_2^*. SWIFT also uses broader excitation bandwidths in comparison to 2D UTE and hence likely all the detectable spins in the vicinity of the calcification are excited. For the benefit of UTE, higher maximum SW/pixel can be achieved.

In comparison to GRE magnitude and phase contrast, the main benefits of SWIFT are very little signal loss due to T_2^* decay and broadband excitation. In addition, in GRE, increasing the contrast of a calcification implies increasing the TE and thus decreasing SNR. In SWIFT, contrast increase mainly requires decreasing SW/pixel, leading to an SNR increase. However, as with UTE, GRE can achieve high SWs, which are only restricted by the gradient performance. Finally, although a more extensive signal loss due to T_2^* decay can be a drawback for GRE, it may also be beneficial in the sense that there is less short T_2^* induced blur. For this reason, the calcification may appear sharper in magnitude images.

SWI (Haacke et al. 2004) may be more intuitive in visualization over only GRE magnitude or phase, as the effect of the calcification or some other field perturber is overlaid on the magnitude image that often has better contrast than the phase image, and also the sign of the susceptibility difference is reflected in the image. However, for methods based on phase imaging, the greatest problem can be the non-locality of the signal that is also used in SWIFT calcification detection. In the case of multiple calcifications and/or hemorrhages closely together, it may become difficult to separate the individual components and the sign of the susceptibility. The non-locality can also exaggerate the size of the calcification, as discussed before. In this case, QSM becomes beneficial, since the non-locality is removed and objects that give no signal are visualized by their susceptibility. Given that the post-processing chain of QSM is easily used, the process of removing unreliable phase values e.g. by cropping (Schweser et al. 2010), the image quality is not compromised, and T_2^* induced signal loss is not too severe,

QSM may be the preferred method. However, if these conditions do not apply, then SWIFT phase imaging can be superior.

7.3 PHASE IMAGING OF SMALL OFF-RESONANCES WITH A MINIMAL TE (II)

Since detecting relatively strong field perturbers such as iron nanoparticles and calcifications using SWIFT phase contrast was feasible, the next logical step was to examine whether WM-GM phase contrast would also be possible. Initial hints of WM-GM contrast were seen already in study **I**, but there, the contrast was relatively weak. In order to evaluate and demonstrate SWIFT phase contrast in brain, a series of experiments were conducted in brain tissue along with a phantom and simulations.

7.3.1 Unconventional phase contrast behavior of SWIFT

The T_2^* phantom experiment and matching simulations showed how SWIFT phase increased with increasing off-resonance, increasing acquisition time, smaller object size and also, in this case, with shortening T_2^*. Not surprisingly, the phase increase with increasing off-resonance was approximately linear, though this was seen to change with a higher off-resonance because of the signal shift. Similarly, the phase increase because of increasing acquisition time was assessed as linear. In both cases, each spatial frequency has the same relative phase increase due to increased off-resonance or acquisition time. The phase increase in smaller objects is explained by the increasing spatial frequency content: a smaller and smaller object contains more and more high spatial frequencies that also have the highest phase accumulation. These experiments demonstrated the importance of the object geometry on SWIFT phase contrast.

The intuitive expectation for phase with increasing transverse relaxation would be decreased phase contrast. However, in this case, the average phase of the ROI increases, since the increasing T_2^* blur shifts the strong phase at the edge of the $MnCl_2$ tube/simulated cylinder to the center. The same phenomena can be seen initially in the "WM stripe" simulation, but eventually phase decreases once the T_2^* decay starts to dominate. These experiments and simulations show the feasibility of having phase contrast, even with relatively low T_2^* values.

Finally, a virtual phantom was used to demonstrate how SWIFT phase contrast can depend on the magnitude contrast. The phantom was composed of a narrow, straight "WM" strip surrounded by "GM". The direction of the phase accumulation was shown to reverse when the magnitude contrast of the "WM strip" with constant WM off-resonance, but increasing global off-resonance, was reversed. This happens because of the imaginary tails outside the structures themselves, strongest at the structure border. This tail extending outside the object exists because the "dispersion spectrum" of the object is non-zero as a result of off-resonance, as explained in section 7.1. When the "WM strip" simulation is shifted globally off-resonance, two imaginary components compete in "WM": the imaginary tail of "GM" and imaginary component of "WM" inside the structure. The component which has the higher amplitude or a higher magnitude signal is the dominant component for the phase contrast. Thus when "GM" magnitude is less than "WM" magnitude, off-resonant "WM" dominates the phase inside itself and in "GM" near the border of the structures, and correspondingly when "GM" magnitude is higher, the "GM" dominates the phase. The same effect would be seen even if there was no initial frequency difference.

Overall, these results display the additional complexities of SWIFT phase contrast introduced by the center-out acquisition scheme. It should be noted that Cartesian GRE is not completely immune to object geometry and T_2^* decay either, in the sense of phase. Given that T_2^* is short in comparison to the acquisition time, the components of the second half of the k-space can have considerably different amplitudes than in the first half. This leads to a residual imaginary component in image space, even if the object is not in off-resonance (Haacke et al. 1999). Furthermore, since this amplitude difference is stronger for higher and higher spatial frequencies, the strength of the effect depends on the geometry of the object.

7.3.2 SWIFT phase contrast in brain is similar to GRE but not the same

Orientation dependence of the WM-GM contrast has been one of the key features of GRE phase imaging and hence it was also studied with SWIFT. An excellent linear correlation was found in a rat brain between SWIFT phase and GRE measured frequency in different orientations to B_0. In the light of the phantom and simulation experiments, this was not a surprise: SWIFT phase is linearly proportional to the frequency shift. This experiment also verified that the SWIFT phase mainly originates from the same components as the GRE phase. This can be considered as a minor disappointment, but it also shows that even though the SWIFT phase contrast behavior can be complicated, it can also still be interpreted similarly to GRE phase contrast.

It was further shown in the perfused rat brain how lengthening the acquisition time could enable stronger phase contrast. The effect of structure geometry was likely seen as a discrepancy between highest phase accumulation in SWIFT and highest MGRE3D measured frequency in the WM structures.

In order to demonstrate the effect of short T_2^* components on SWIFT phase contrast, an MT magnetization preparation was employed. This suppressed homogeneously broadened short T_2 components, although it naturally also decreased the signal of free water pool. The increased phase and increased non-linearity in the phase accumulation was related to suppression of the signal from myelin water (Mackay et al. 1994) that is known to be more affected by MT (Stanisz et al. 1999, Vavasour et al. 2000, Sati et al. 2013). It has been shown that myelin water has a larger, opposite signed frequency shift compared to the free water pool, although the myelin water pool itself is smaller (Wharton & Bowtell 2012b, van Gelderen et al. 2012, Sati et al. 2012, Sati et al. 2013). When this component was removed, the phase accumulation was increased in the WM structures. For SWIFT, this effect is weaker with longer acquisition times, since the phase accumulation is concentrated on the lower spatial frequencies due to faster T_2^* decay relative to the acquisition time. This was also confirmed in the simple two-pool "WM strip" simulation. Furthermore, as discussed before in the previous section, large scale off-resonance and/or changing magnitude contrast may have affected the change in phase accumulation. In this sense, scanner drift could be an issue, however, this was taken into account as explained in section 5.4.3.

The assessment of the human brain sample demonstrated that SWIFT phase component does have contrast even when the relative width of the WM structure is wide. The concern was that once a structure become wide and is mainly composed of low spatial frequencies, also the contrast will disappear. However, at high resolution, the small details of a structure become visible, leading to contrast. It could be that at an intermediate resolution, these fine details are averaged out by partial voluming, and SWIFT phase contrast would be decreased.

The final brain experiment of study **II** was *in vivo* imaging of the rat brain. Although contrast of the main WM structures was seen, it was weaker than that in the *ex vivo* experiments. The reasons for this were the higher SW/pixel (122 Hz vs. highest *ex vivo* 81 Hz), the much lower scan time (1 h 7 min vs. *ex vivo* 8 h) and the use of the surface coil. It was essential to use a higher SW/pixel in order to avoid artifacts because of bulk susceptibility differences, especially at the high field of 16.4 T. For *in vivo* imaging, very long scan times are naturally not feasible, though extending it to approximately two hours would not be unheard of in small animal imaging. The adoption of the surface transceiver coil enables high SNR at the cortical level, but less when probing deeper into the brain's different WM structures, because of the lower flip angles and lower detection sensitivity.

7.3.3 Is SWIFT phase imaging useful? (I, II)

In the sense that GRE is a very simple pulse sequence with easy reconstruction and well established theoretical basis, one has to pose the question whether SWIFT phase contrast could really be more useful. As a pulse sequence, even though SWIFT is rather non-conventional because of the gapped HS pulses, it is also very simple in its repetition of this same scheme. The understanding of SWIFT has greatly increased during the time that this thesis was being

completed. On the image reconstruction side, for SWIFT, major advances occurred, and there is a solid theoretical basis in the literature. In that respect, image reconstruction for non-Cartesian imaging is not a challenge. These improvements have led to dramatic improvements in SWIFT image quality. This can be seen by comparing the *ex vivo* images obtained in study **I** to those from studies **II** and **III**. Hence, the perceived complexity of the SWIFT pulse sequence itself is not an issue.

Although the idea of phase accumulation during the acquisition is rather simple, this makes the phase contrast behavior of SWIFT more complicated than with GRE. However, the properties of the FT still apply and are very useful in designing a SWIFT phase experiment and in interpreting the data. On the other hand, due to the lower sensitivity, in the form that SWIFT is now, it may not be the preferred method over GRE in brain structure phase imaging. In study **II**, although impressive SWIFT phase images were taken, the SNR was in the range of 200 which is not easily achieved *in vivo*, at least in small animal imaging.

Only in the sense of SNR, in human imaging adequate signal levels may be achieved through increased voxel size, though also noise is increased with a larger volume of the RF coil. During this thesis project, initial attempts at human SWIFT phase imaging were made using the author's brain. Some contrast was seen, but clearly more work would be needed before this approach could be utilized. One likely problem was the phase of the B_1-field, which becomes a significant factor at the human scale. In addition, in retrospect, the resolution was likely too low to produce a significant amount of high spatial frequencies. One way to further increase the phase contrast may be to develop schemes combining gradient and RF-pulse frequency modulation (Zhang et al. 2015), so that phase accumulation is weighted differently for different ranges of spatial frequencies.

An important application of GRE phase imaging is the ability to calculate field maps. A considerable effort was made to utilize SWIFT for field mapping during this thesis project. In the end, all the problems condensed down to the ill-posed behavior of off-resonance phase at the center of k-space. One potential option for overcoming this shortcoming would be to implement echoes for SWIFT, although they would have impaired short T_2^* sensitivity.

At the present time, SWIFT phase contrast may find its most valuable applications in imaging strong field perturbers such as the calcifications examined in study **I**. In these types of scenarios, SWIFT benefits from not losing any signal due to increased T_2^* decay, and the parameters can be set to minimize the phase background and maximize the conspicuity of the dipole.

7.4 MT SWIFT MORE CONSISTENT THAN DTI IMAGING SUBTLE CHANGES AFTER TBI (III)

Study **III** compared two clinically advanced methods, MT and DTI, in imaging mild changes of brain because of the secondary injuries of TBI. An extensive comparison was made to the histological findings MT SWIFT was shown to be more consistent than DTI in detecting tissue alterations due to pathology throughout the thalamocortical pathway of the barrel field of the primary somatosensory cortex.

7.4.1 Decreased MTR after TBI mainly related to loss of myelinated fibers

As far as the author is aware, no other similar in depth studies of the thalamocortical pathway have been conducted with MT, DTI or other MRI methods to study TBI. The perilesional cortices of animals evaluated with the same model have been examined at a chronic time point (Immonen et al. 2009), however, study **III** concentrated on the more subtle damage outside this area.

The *ex vivo* MTR decreased in the external capsule and in layers VIb-IV of the barrel cortex, and all of these regions exhibited demyelination, as observed by histology. Histology also revealed mild gliosis and iron accumulation in the cortex that could both affect MTR through

changed T_1 (Helms et al. 2010). However, the profile analysis of the moderately T_1 weighted MT SWIFT reference images detected no significant changes. In addition, no change was seen in the moderately T_2 weighted DTI b0-images, eliminating the possibility of edema. Based on these findings, it was concluded that MTR in the cortex was mostly reflecting loss of myelinated fibers. Similar findings of the cortex have been made in humans after TBI (Kumar et al. 2003). *Ex vivo* MTR was also slightly decreased on the contralateral side of the TBI animals. Although the histological techniques used here revealed no corresponding change, it is still possible that the injury can spread also to the side not suffering any direct impact. *In vivo* MTR did not detect any decreases in layers V-I, or in the contralateral hemisphere. This is possibly related to the lower SNR.

The *ex vivo* ROI analysis results showed consistently decreased MTR in all of the subcortical areas. The *In vivo* results agreed with *ex vivo* findings that the caudal internal capsule had the largest change in MTR, although other ROIs showed no statistically significant differences, *in vivo*. According to the histology, the caudal internal capsule also had the highest degree of demyelination, gliosis and iron accumulation. The ipsilateral internal capsule of the sham operated animals likewise showed some signs of gliosis (qualitatively), but no iron accumulation or demyelination, and importantly no MTR change. However, SWIFT T_1 weighted images did detect a signal increase. Hence, the MTR decrease in the ipsilateral caudal internal capsule of the TBI animals is mostly reflecting demyelination, with some T_1 shortening from iron accumulation. No correlation between group averaged MTR and Nissl quantitation, or gliosis, and the excellent correlation between group averaged MTR and myelin quantitation further demonstrated how the MTR had changed mainly because of demyelination also in other subcortical areas and in the cortex.

7.4.2 DTI findings are more challenging to interpret

The increase in RD has been related to demyelination (Song et al. 2005, Boretius et al. 2012, Song et al. 2002, Ou et al. 2009, Janve et al. 2013) and decreased AD to axonal damage (MacDonald et al. 1986, DeBoy et al. 2007, Sun et al. 2007, Wu et al. 2007) in multiple disease models. The combination of these two was likely the reason for the decreased FA in the ipsilateral external capsule of the TBI animals. Crossing fibers were not thought to be the reason for the orientationally homogeneous external capsule as it is unlikely that there would a major change in the direction of part of the fibers. As gliosis was seen in the external capsule, astrocytic processes may have exerted an effect (Budde et al. 2011). Another important factor may have been partial voluming, since the external capsule becomes very thin after TBI due to tissue atrophy. Partial voluming would mix high FA external capsule with the surrounding lower FA areas.

The second area which underwent a statistically significant change in the profile analysis of DTI was the decreased FA in layer VIa. Since this area had no large amounts of gliosis or iron accumulation, this may have represented a case for changed proportions of fibers with different orientations as seen qualitatively in the myelin stained sections. Based on histology, layer VIb had loss of myelinated axons, gliosis and iron accumulation, yet no change in DTI was seen. Here it seems that these changes counteracted each other, or possibly there was a similar loss of myelinated fibers of all orientations (Wheeler-Kingshott & Cercignani 2009).

DTI changes in the subcortical areas were much more varied than MTR. Both the striatum and globus pallidus consist of fiber bundles with very uniform directionality, surrounded by GM or some individual myelinated fibers, respectively. In both areas, the loss of myelinated fibers was seen as thinner bundles. As such, increased partial voluming would decrease FA and AD. However, there were statistically significant increases in FA and AD in the caudal striatum and increased AD in the caudal globus pallidus. Both areas displayed evidence of iron accumulation within the bundles, and hence these increases may have been related to iron. Since iron can cause an SNR decrease, it has been shown to artifactually increase FA and AD (Rulseh et al. 2013). Iron accumulation has also been proposed as a reason for increasing FA in

GM (Pfefferbaum et al. 2010) with age, and the coupling between diffusion gradients and iron induced field gradients has been utilized for iron quantitation using DWI (Fujiwara et al. 2014), further demonstrating the putative effect of iron on diffusion imaging. In addition, it may also be that the astrocytic processes were aligned with the fiber bundles affecting FA and AD (Budde et al. 2011).

The most caudal internal capsule and rostral internal capsule showed opposite DTI behavior with increased RD and unchanged FA in the former, and decreased RD and increased FA in the latter structure. In the present results, the internal capsule had the highest FA of the analyzed subcortical structures. The individual bundles of the internal capsule have parallel fiber directions, but the bundles themselves have different directions. Hence, with high enough resolution to allow sufficiently little partial voluming, the internal capsule is shown as a high FA structure. Thus, the further increased FA in the rostral internal capsule is not likely to be related to changed proportions in the populations of fibers travelling in different directions. The rostral internal capsule showed gliosis, but less iron accumulation and less extensive myelin loss than the caudal part. Hence it may again be that the astrocytic processes have aligned with the bundles in the rostral part, leading to the increased FA. The most caudal internal capsule showed evidence of gliosis, iron and demyelination, but with increased RD as the only significant change in DTI metrics, and therefore loss of myelinated fibers was likely the dominant component.

The thalamus showed increased FA, possibly due to its rather high iron content, although myelinated fiber loss and gliosis were also detected. As seen in the TBI animals of study **I** at the same time point, there was calcification in the thalamus. This may have had an effect on the ROI analysis results, however, the ROI was not directly in the area where the calcification had been detected before.

7.4.3 Comparison of MT and DTI

The results of the MTR ROI analysis correlated much better with the corresponding myelin quantitation than any of the DTI metric results. In addition, DTI metrics correlated with Nissl staining in the ipsilateral cortex of the TBI animals, whereas MTR showed no correlation at all. This further demonstrated how DTI was more affected by gliosis than MTR, at least in this experimental setting. This was slightly surprising, since MTR has been suggested to be sensitive to gliosis via a T_1 increase (Dousset et al. 1992), but this may have been due to edema associated with the gliosis (Grossman et al. 1987). Since here there were no changes in the T_2 weighted DTI b0 images in the cortex and very mild changes in the subcortex, any possible edema had likely subsided. It is also surprising in the sense that if there is an increased cell content, then there should be an increase in the macromolecular content, which would intuitively point to increased MTR. However, it may be that the glial cells do not possess efficient exchange sites as myelin (Koenig 1991, Brown & Koenig 1992). As far as is known, the MT of glial cells has not been studied in any detail.

There are no studies comparing MTR and DTI in TBI models. However, they have been compared in other disease models with demyelination and gliosis. MTR and DTI were examined in corpus callosum in a model combining demyelinating cuprizone diet and inflammation and axonal damage leading to experimental autoimmune encephalomyelitis (EAE) (Boretius et al. 2012). These workers found evidence of attenuated MTR after curprizone diet, as expected, and more so after the development of EAE which was related to the decreased myelin density due to axonal swelling and edema. Even though these are likely present at an acute time point after TBI, in the chronic time point of this present study, neither of these features were detected. AD was shown to increase only after axonal damage caused by EAE, in line with the literature, whereas RD was shown to decrease after EAE, at first being elevated due to the myelin loss from the curprizone diet. The reported behavior of RD slightly contradicts the present results where RD in the caudal internal capsule was elevated even in the presence of inflammation. However, this is likely related to the different types of inflammation.

There is another difference; Boretius et al. reported decreased T_1 after both steps, whereas the present results indicated the opposite, due to iron accumulation which was not described in the other work.

Quantitative MT (qMT) methods model the MT phenomena with two or more pools with their own relaxation rates and exchange rates of magnetization between pools (Sled & Pike 2001, Ceckler et al. 2001). These methods describe the MT effect in a more accurate way than MTR, however they are also more complicated and more time consuming. In a qMT study (Thiessen et al. 2013), it was found that MTR, FA, AD and RD could not reveal changes in the cortex in a cuprizone model, whereas qMT did detect a change. In comparison to the present results, this negative result for MTR was likely related to the effect of the cuprizone model itself in the cortex, and having only a single ROI in the cortex and likely lower SNR than in study **III**. Both of these last two points could well mask any possible changes. With a so-called cross relaxation imaging qMT method, the bound pool fraction (BPF) was shown to correlate with FA and RD in the GM, but not in the WM (Underhill et al. 2009). This was related to the fact that DTI is more sensitive to the directional coherence of the fibers than it is to myelin density, whereas bound pool fractions are indifferent of the fiber direction. In GM, where fiber direction can be very heterogeneous, this sensitivity is less of a factor, instead the DTI metrics may reflect more the different densities of myelinated fibers, leading to better correlation with BPF. Another study with the same method involving cross-relaxation imaging, similarly found a very weak correlation between BPF and FA in WM, however, a better correlation was found in corpus callosum exclusively, which is a very coherent structure in the sense of its fiber direction (Stikov et al. 2011). The correlation also varied in different parts of the corpus callosum. This correlation was related to different degrees of volume occupied by the myelinated fibers. Together these two studies show how DTI reflects the myelin content of the tissue to some degree, but MT methods are better in this sense. Even though MTR is less specific than BPF, it does contain the same information.

It has also been shown that MTR does not correlate with myelin content in healthy rat brains (Underhill et al. 2011), because of its limited dynamic range. However, BPF did detect a correlation with the myelin content, and MTR correlated with BPF. MTR correlated well with myelin content in study **III**, although our analysis also contained the thalamus and striatum which both contain GM. This increases the dynamic range on the structure side and likely improves the possibility to detect a correlation, while it is clear from the results that MTR would correlate also with pure WM structures.

7.4.4 Short T2* imaging, MT and SWIFT

In study **II,** it was shown that MTR was higher using SWIFT than with MGRE3D in perfused rat brain with as equal parameters as possible. The MRI detectable myelin specific signal has been shown with spectroscopic methods (Horch et al. 2011) and has now likely been visualized with UTE (Wilhelm et al. 2012, Du et al. 2014). Hence, there is no doubt that this signal is also detected by SWIFT. As mentioned before, long T_2^* suppression was explored for SWIFT during this thesis (Lehto et al. 2010, Larson et al. 2006), but deemed to be contaminated by MT. In this scheme, a long adiabatic inversion pulse is employed. Short T_2^* components will decay during the pulse and will not experience an inversion, whereas long T_2^* components will be inverted. With the optimal choice of inversion time, long T_2^* components can be nullified. In retrospect, since this scheme is based on inversion recovery and thus repeated with relatively long delays, it is likely that the MT contribution was small. In contrast to the 2D UTE, several acquisitions were made at the inversion time to save total scan time, but it is unlikely that this would have made a considerably difference for the short T_2^* purity of the signal. However, as for SWIFT frequency mapping, implementing echoes would have been essential for demonstrating the short T_2^* nature of the signal.

Since for most of the time, SWIFT TR is approximately the same as the length of the gapped HS pulse, the possibility of intrinsic MT contrast is worth considering. In the SWIFT

implementation used in studies **II** and **III**, the duty cycle of the pulse was only 25 %. The rest of the time was spent on acquisition waiting for coil ringdown and waiting for transmit/receive gating. In addition, the gapped pulse consisted only of the first half of the acquisition. Hence, the amount of RF pulsing was comparable to that used in short TR gradient recalled echo. However, the frequency sweep of the HS pulses simultaneously with the readout gradient changes the situation slightly. At the center of the FOV, the isochromat experiences the same off-resonance saturation of the gapped pulse on every TR, sweeping from –SW/2 to SW/2. At the edge of the FOV, the off-resonance saturation for the isochromat varies between sweeps from 0 to SW and from –SW/2 to SW/2, depending on the direction of the readout gradient. The off-resonance saturation for other locations varies between these two cases depending on the distance to the center of the FOV. Additionally, the intrinsic MT weighting would depend on the pulse SW being used since this governs the off-resonance frequency of the saturation. Thus, maximal intrinsic MT weighting is experienced at the center of the FOV and minimum, varying MT weighting is experienced at the edge of the FOV. This would indicate that the intrinsic MT weighting is spatially dependent. However, this kind of behavior was not noted in the present SWIFT experiments, and the images with actual MT preparations were clearly different in contrast. Hence it can be concluded that the intrinsic MT weighting of SWIFT is not strong, although it should be verified with more detailed quantitative experiments in the future.

7.5 FUTURE PROSPECTS

This thesis has produced the first examples of applications of SWIFT in brain imaging, and also some of the first applications in the family of near zero TE pulse sequences. Before SWIFT phase imaging can become a viable option in the future, good contrast comparable to GRE has to be possible with less SNR and imaging time. As mentioned before, simultaneous modulation of the readout gradient and the frequency sweep of the HS pulse may offer options for enhancing the phase contrast. Furthermore, other steps for improving SNR must be made. In addition, $\boldsymbol{B_1}$-phase mapping or estimation would be very beneficial, given that a coil does not have a homogeneous $\boldsymbol{B_1}$-phase. Otherwise, the SWIFT phase can be easily spoiled, especially at higher magnetic fields and with bigger coils where wavelength begins to play an important role. In addition, it will be necessary to find a way to estimate frequency maps from the SWIFT phase since this would facilitate using SWIFT for the ever-growing QSM.

As it is, at this time, SWIFT phase could already be useful for the detection of calcification or microbleeds in brain, and also for other target areas, such as the breast (Stomper & Margolin 1994), where SWIFT has already been applied in other approaches (Corum et al. 2014). Echoes could be implemented to undertake frequency and short T_2^* mapping. This could be achieved by a GRE (Park et al. 2011) or even with an SE type of implementation (Park & Garwood 2009). Multi-echo acquisition could be accelerated by view sharing of the echoes (Altbach et al. 2002).

One crucial advance to be implemented into animal and human SWIFT imaging would be to develop a coil system with separate excitation and receive coils. A more homogenous exciting $\boldsymbol{B_1}$-field, such as in the *ex vivo* volume coil used in all studies of this thesis, would permit better usage of a MT preparation, but also other more sophisticated magnetization preparations.

MT SWIFT was shown very promising in imaging of TBI. Even though rather simple MTR was successful, the development towards qMT methods would be advisable as they have indeed been shown to be more specific for myelin (Underhill et al. 2011). The benefit of SWIFT would lie in its ability to detect the short T_2^* pool of myelin and to estimate the myelin water signal better than GRE, for example. SWIFT qMT could employ an inversion scheme (Gochberg & Gore 2003) in a Look-Locker manner (Gochberg & Gore 2007).

With respect to detecting the subtle secondary injuries occurring after TBI, even though MTR was shown to perform better than DTI, it is likely desirable to use both MT and DTI methods in conjunction as they provide complementary information. Especially with the appearance of multiple different acceleration techniques for human imaging (Pruessmann et al. 1999, Larkman

et al. 2001, Lustig et al. 2007), both of these methods can be made feasible for implementation in a non-acute situation.

8 References

Acosta-Cabronero, J., Williams, G.B., Cardenas-Blanco, A., Arnold, R.J., Lupson, V. and Nestor, P.J., 2013. In vivo quantitative susceptibility mapping (QSM) in Alzheimer's disease. *PloS One*, vol. 8, no. 11, pp. e81093.

Altbach, M.I., Outwater, E.K., Trouard, T.P., Krupinski, E.A., Theilmann, R.J., Stopeck, A.T., Kono, M. and Gmitro, A.F., 2002. Radial fast spin-echo method for T2-weighted imaging and T2 mapping of the liver. *Journal of Magnetic Resonance Imaging*, vol. 16, no. 2, pp. 179-189.

Andriessen, T.M., Jacobs, B. and Vos, P.E., 2010. Clinical characteristics and pathophysiological mechanisms of focal and diffuse traumatic brain injury. *Journal of Cellular and Molecular Medicine*, vol. 14, no. 10, pp. 2381-2392.

Ansari, M.Q., Chincanchan, C.A. and Armstrong, D.L., 1990. Brain calcification in hypoxic-ischemic lesions: an autopsy review. *Pediatric Neurology*, vol. 6, no. 2, pp. 94-101.

Araki, Y., Furukawa, T., Tsuda, K., Yamamoto, T. and Tsukaguchi, I., 1990. High field MR imaging of the brain in pseudohypoparathyroidism. *Neuroradiology*, vol. 32, no. 4, pp. 325-327.

Arnold, M.M. and Kreel, L., 1991. Asymptomatic cerebral calcification--a previously unrecognized feature. *Postgraduate Medical Journal*, vol. 67, no. 784, pp. 147.

Avrahami, E., Cohn, D., Feibel, M. and Tadmor, R., 1994. MRI demonstration and CT correlation of the brain in patients with idiopathic intracerebral calcification. *Journal of Neurology*, vol. 241, no. 6, pp. 381-384.

Bagley, L.J., McGowan, J.C., Grossman, R.I., Sinson, G., Kotapka, M., Lexa, F.J., Berlin, J.A. and McIntosh, T.K., 2000. Magnetization transfer imaging of traumatic brain injury. *Journal of Magnetic Resonance Imaging*, vol. 11, no. 1, pp. 1-8.

Balcom, B.J., MacGregor, R.P., Beyea, S., Green, D., Armstrong, R. and Bremner, T., 1996. Single-Point Ramped Imaging with T1 Enhancement (SPRITE). *Journal of Magnetic Resonance, Series A*, vol. 123, no. 1, pp. 131-134.

Balla, D.Z., Sanchez-Panchuelo, R.M., Wharton, S.J., Hagberg, G.E., Scheffler, K., Francis, S.T. and Bowtell, R., 2014. Functional quantitative susceptibility mapping (fQSM). *NeuroImage*, vol. 100, pp. 112-124.

Barat, R., Montoya, T., Seco, A. and Ferrer, J., 2011. Modelling biological and chemically induced precipitation of calcium phosphate in enhanced biological phosphorus removal systems. *Water Research*, vol. 45, no. 12, pp. 3744-3752.

Basser, P.J. and Pierpaoli, C., 1996. Microstructural and physiological features of tissues elucidated by quantitative-diffusion-tensor MRI. *Journal of Magnetic Resonance*, vol. 111, pp. 209-219.

Baumann, N. and Pham-Dinh, D., 2001. Biology of oligodendrocyte and myelin in the mammalian central nervous system. *Physiological Reviews*, vol. 81, no. 2, pp. 871-927.

Beatty, P.J., Nishimura, D.G. and Pauly, J.M., 2005. Rapid gridding reconstruction with a minimal oversampling ratio. *Medical Imaging, IEEE Transactions On*, vol. 24, no. 6, pp. 799-808.

Bender, B. and Klose, U., 2010. The in vivo influence of white matter fiber orientation towards B0 on T2* in the human brain. *NMR in Biomedicine*, vol. 23, no. 9, pp. 1071-1076.

Bernstein, M.A., King, K.F. and Zhou, X.J., 2004. *Handbook of MRI pulse sequences.* 1st ed. USA: Academic Press.

Bianciardi, M., van Gelderen, P. and Duyn, J.H., 2014. Investigation of BOLD fMRI resonance frequency shifts and quantitative susceptibility changes at 7 T. *Human Brain Mapping*, vol. 35, no. 5, pp. 2191-2205.

Blakemore, W., 1973. Demyelination of the superior cerebellar peduncle in the mouse induced by cuprizone. *Journal of the Neurological Sciences*, vol. 20, no. 1, pp. 63-72.

Bloch, F., 1946. Nuclear induction. *Physical Review*, vol. 70, no. 7-8, pp. 460.

Boretius, S., Escher, A., Dallenga, T., Wrzos, C., Tammer, R., Brück, W., Nessler, S., Frahm, J. and Stadelmann, C., 2012. Assessment of lesion pathology in a new animal model of MS by multiparametric MRI and DTI. *NeuroImage*, vol. 59, no. 3, pp. 2678-2688.

Bosemani, T., Poretti, A. and Huisman, T.A., 2014. Susceptibility-weighted imaging in pediatric neuroimaging. *Journal of Magnetic Resonance Imaging*, vol. 40, no. 3, pp. 530-544.

Bradley, W.G.,Jr, 1993. MR appearance of hemorrhage in the brain. *Radiology*, vol. 189, no. 1, pp. 15-26.

Brandstack, N., Kurki, T., Tenovuo, O. and Isoniemi, H., 2006. MR imaging of head trauma: visibility of contusions and other intraparenchymal injuries in early and late stage. *Brain Injury*, vol. 20, no. 4, pp. 409-416.

Brant-Zawadzki, M., Davis, P.L., Crooks, L.E., Mills, C., Norman, D., Newton, T.H., Sheldon, P. and Kaufman, L., 1983. NMR Demonstration of Cerebral Abnormalities: Comparison with CT. *Am J Neuroradiol*, vol. 36, no. 6, pp. 117-124.

Brown, R.D. and Koenig, S.H., 1992. 1/T1p and low-field 1/T of tissue water protons arise from magnetization transfer to macromolecular solid-state broadened lines. *Magnetic Resonance in Medicine*, vol. 28, no. 1, pp. 145-152.

Brown, T.R., Kincaid, B.M. and Ugurbil, K., 1982. NMR chemical shift imaging in three dimensions. *Proceedings of the National Academy of Sciences*, vol. 79, no. 11, pp. 3523-3526.

Bruns, J. and Hauser, W.A., 2003. The epidemiology of traumatic brain injury: a review. *Epilepsia*, vol. 44, no. s10, pp. 2-10.

Budde, M.D., Janes, L., Gold, E., Turtzo, L.C. and Frank, J.A., 2011. The contribution of gliosis to diffusion tensor anisotropy and tractography following traumatic brain injury: validation in the rat using Fourier analysis of stained tissue sections. *Brain : A Journal of Neurology*, vol. 134, no. Pt 8, pp. 2248-2260.

Büki, A. and Povlishock, J., 2006. All roads lead to disconnection?–Traumatic axonal injury revisited. *Acta Neurochirurgica*, vol. 148, no. 2, pp. 181-194.

Buonocore, M.H. and Gao, L., 1997. Ghost artifact reduction for echo planar imaging using image phase correction. *Magnetic Resonance in Medicine*, vol. 38, no. 1, pp. 89-100.

Bushberg, J.T. and Boone, J.M., 2011. *The essential physics of medical imaging*. Lippincott Williams & Wilkins.

Caldemeyer, K.S., Mathews, V.P., Edwards-Brown, M.K. and Smith, R.R., 1997. Central nervous system cryptococcosis: parenchymal calcification and large gelatinous pseudocysts. *American Journal of Neuroradiology*, vol. 18, no. 1, pp. 107-109.

Carl, M. and Chiang, J.A., 2012. Investigations of the origin of phase differences seen with ultrashort TE imaging of short T2 meniscal tissue. *Magnetic Resonance in Medicine*, vol. 67, pp. 991-1003.

Carl, M., Bydder, M., Du, J., Takahashi, A. and Han, E., 2010. Optimization of RF excitation to maximize signal and T2 contrast of tissues with rapid transverse relaxation. *Magnetic Resonance in Medicine*, vol. 64, no. 2, pp. 481-490.

Cavanagh, J., Fairbrother, W.J., Palmer III, A.G. and Skelton, N.J., 1995. *Protein NMR spectroscopy: principles and practice*. Academic Press.

Ceckler, T., Maneval, J. and Melkowits, B., 2001. Modeling magnetization transfer using a three-pool model and physically meaningful constraints on the fitting parameters. *Journal of Magnetic Resonance*, vol. 151, no. 1, pp. 9-27.

Cervós-Navarro, J. and Lafuente, J.V., 1991. Traumatic brain injury: structural changes. *Journal of the Neurological Sciences*, vol. 103, pp. 3-14.

Chen, W.C., Foxley, S. and Miller, K.L., 2013. Detecting microstructural properties of white matter based on compartmentalization of magnetic susceptibility. *NeuroImage*, vol. 70, pp. 1-9.

Chen, W., Gauthier, S.A., Gupta, A., Comunale, J., Liu, T., Wang, S., Pei, M., Pitt, D. and Wang, Y., 2014a. Quantitative susceptibility mapping of multiple sclerosis lesions at various ages. *Radiology*, vol. 271, no. 1, pp. 183-192.

Chen, W., Zhu, W., Kovanlikaya, I., Kovanlikaya, A., Liu, T., Wang, S., Salustri, C. and Wang, Y., 2014b. Intracranial calcifications and hemorrhages: characterization with quantitative susceptibility mapping. *Radiology*, vol. 270, no. 2, pp. 496-505.

Chen, W., Zhu, W., Kovanlikaya, I., Kovanlikaya, A., Liu, T., Wang, S., Salustri, C. and Wang, Y., 2014c. Intracranial calcifications and hemorrhages: characterization with quantitative susceptibility mapping. *Radiology*, vol. 270, no. 2, pp. 496-505.

Clarke, B., 2008. Normal bone anatomy and physiology. *Clinical Journal of the American Society of Nephrology*, vol. 3 suppl 3, pp. s131-s139.

Cordonnier, C., Al-Shahi Salman, R. and Wardlaw, J., 2007. Spontaneous brain microbleeds: systematic review, subgroup analyses and standards for study design and reporting. *Brain*, vol. 130, no. 8, pp. 1988-2003.

Cordonnier, C. and van der Flier, W.M., 2011. Brain microbleeds and Alzheimer's disease: innocent observation or key player?. *Brain*, vol. 134, no. 2, pp. 335.

Cordonnier, C., 2011. Brain microbleeds: more evidence, but still a clinical dilemma. *Current Opinion in Neurology*, vol. 24, no. 1, pp. 69-74.

Coronado, V.G., Xu, L., Basavaraju, S.V., McGuire, L.C., Wald, M.M., Faul, M.D., Guzman, B.R. and Hemphill, J.D., 2011. *Surveillance for traumatic brain injury-related deaths: United States, 1997-2007.* US Department of Health and Human Services, Centers for Disease Control and Prevention Atlanta.

Corum, C.A., Benson, J.C., Idiyatullin, D., Snyder, A.L., Snyder, C.J., Hutter, D., Everson, L.I., Eberly, L.E., Nelson, M.T. and Garwood, M., 2014. High-Spatial-and High-Temporal-Resolution Dynamic Contrast-enhanced MR Breast Imaging with Sweep Imaging with Fourier Transformation: A Pilot Study. *Radiology*, vol. 274, no. 2, pp. 540-547.

Corum, C.A., Idiyatullin, D., Snyder, C.J. and Garwood, M., 2015. Gap cycling for SWIFT. *Magnetic Resonance in Medicine*, vol. 73, no. 2, pp. 677-682.

Daghighi, M., Rezaei, V., Zarrintan, S. and Pourfathi, H., 2007. Intracranial physiological calcifications in adults on computed tomography in Tabriz, Iran. *Folia Morphologica*, vol. 66, no. 2, pp. 115-119.

Davis, C.A., Genant, H.,K. and Dunham, J.S., 1986. The effects of bone on proton NMR relaxation times of surrounding liquids. *Investigative Radiology*, vol. 21, no. 6, pp. 472-477.

Davis, P.C., 2007. Head trauma. *American Journal of Neuroradiology*, vol. 28, no. 8, pp. 1619-1621.

de Pasquale, F., Cherubini, A., Péran, P., Caltagirone, C. and Sabatini, U., 2013. Influence of white matter fiber orientation on R2* revealed by MRI segmentation. *Journal of Magnetic Resonance Imaging*, vol. 37, no. 1, pp. 85-91.

DeBoy, C.A., Zhang, J., Dike, S., Shats, I., Jones, M., Reich, D.S., Mori, S., Nguyen, T., Rothstein, B., Miller, R.H., Griffin, J.T., Kerr, D.A. and Calabresi, P.A., 2007. High resolution diffusion tensor imaging of axonal damage in focal inflammatory and demyelinating lesions in rat spinal cord. *Brain : A Journal of Neurology*, vol. 130, no. Pt 8, pp. 2199-2210.

Deistung, A., Schweser, F., Wiestler, B., Abello, M., Roethke, M., Sahm, F., Wick, W., Nagel, A.M., Heiland, S. and Schlemmer, H., 2013. Quantitative susceptibility mapping differentiates between blood depositions and calcifications in patients with glioblastoma. *PloS One*, vol. 8, no. 3, pp. e57924.

Dell, L.A., Brown, M.S., Orrison, W.W., Eckel, C.G. and Matwiyoff, N.A., 1988. Physiologic intracranial calcification with hyperintensity on MR imaging: case report and experimental model. *AJNR.American Journal of Neuroradiology*, vol. 9, no. 6, pp. 1145-1148.

Denk, C., Torres, E.H., MacKay, A. and Rauscher, A., 2011. The influence of white matter fibre orientation on MR signal phase and decay. *NMR in Biomedicine*, vol. 24, no. 3, pp. 246-252.

Dong, X., Wang, Y. and Qin, Z., 2009. Molecular mechanisms of excitotoxicity and their relevance to pathogenesis of neurodegenerative diseases. *Acta Pharmacologica Sinica*, vol. 30, no. 4, pp. 379-387.

Dousset, V., Grossman, R.I., Ramer, K.N., Schnall, M.D., Young, L.H., Gonzalez-Scarano, F., Lavi, E. and Cohen, J.A., 1992. Experimental allergic encephalomyelitis and multiple sclerosis: lesion characterization with magnetization transfer imaging. *Radiology*, vol. 182, no. 2, pp. 483-491.

Du, J., Corbeil, J., Znamirowski, R., Angle, N., Peterson, M., Bydder, G.M. and Kahn, A.M., 2011a. Direct imaging and quantification of carotid plaque calcification. *Magnetic Resonance in Medicine*, vol. 65, no. 4, pp. 1013-1020.

Du, J., Bydder, M., Takahashi, A.M., Carl, M., Chung, C.B. and Bydder, G.M., 2011b. Short T2 contrast with three-dimensional ultrashort echo time imaging. *Magnetic Resonance Imaging*, vol. 29, no. 4, pp. 470-482.

Du, J., Ma, G., Li, S., Carl, M., Szeverenyi, N.M., VandenBerg, S., Corey-Bloom, J. and Bydder, G.M., 2014. Ultrashort echo time (UTE) magnetic resonance imaging of the short T2 components in white matter of the brain using a clinical 3T scanner. *NeuroImage*, vol. 87, pp. 32-41.

Durrant, C., Hertzberg, M. and Kuchel, P., 2006. Magnetic susceptibility: further insights into macroscopic and microscopic fields and the sphere of Lorentz. *Concepts in Magnetic Resonance Part A*, vol. 18, no. 1, pp. 72-95.

Duyn, J.H., Van Gelderen, P., Li, T.Q., De Zwart, J.A., Koretsky, A.P. and Fukunaga, M., 2007. High-field MRI of brain cortical substructure based on signal phase. *Proceedings of the National Academy of Sciences*, vol. 104, no. 28, pp. 11796-11801.

Duyn, J.H., 2014. Frequency shifts in the myelin water compartment. *Magnetic Resonance in Medicine*, vol. 71, no. 6, pp. 1953-1955.

Duyn, J.H. and Barbara, T.M., 2014. Sphere of lorentz and demagnetization factors in white matter. *Magnetic Resonance in Medicine*, vol. 72, no. 1, pp. 1-3.

Dykes, F.D., Ahmann, P.A. and Lazzara, A., 1982. Cranial ultrasound in the detection of intracranial calcifications. *The Journal of Pediatrics*, vol. 100, no. 3, pp. 406-408.

Eissa, A., Lebel, R.M., Korzan, J.R., Zavodni, A.E., Warren, K.G., Catz, I., Emery, D.J. and Wilman, A.H., 2009. Detecting lesions in multiple sclerosis at 4.7 tesla using phase susceptibility-weighting and T2-weighting. *Journal of Magnetic Resonance Imaging*, vol. 30, no. 4, pp. 737-742.

Eng, J., Ceckler, T.L. and Balaban, R.S., 1991. Quantitative 1H magnetization transfer imaging in vivo. *Magnetic Resonance in Medicine*, vol. 17, no. 2, pp. 304-314.

Ernst, R.R. and Anderson, W., 1966. Application of Fourier transform spectroscopy to magnetic resonance. *Review of Scientific Instruments*, vol. 37, no. 1, pp. 93-102.

Fjær, S., Bø, L., Lundervold, A., Myhr, K., Pavlin, T., Torkildsen, Ø and Wergeland, S., 2013. Deep gray matter demyelination detected by magnetization transfer ratio in the cuprizone model. *PloS One*, vol. 8, no. 12, pp. e84162.

Friedland, R.P., Luxenberg, J.S. and Koss, E., 1990. A quantitative study of intracranial calcification in dementia of the Alzheimer type. *International Psychogeriatrics*, vol. 2, no. 01, pp. 37-43.

Fujiwara, S., Uhrig, L., Amadon, A., Jarraya, B. and Le Bihan, D., 2014. Quantification of iron in the non-human primate brain with diffusion-weighted magnetic resonance imaging. *NeuroImage*, vol. 102, pp. 789-797.

Fukunaga, M., Li, T.Q., van Gelderen, P., de Zwart, J.A., Shmueli, K., Yao, B., Lee, J., Maric, D., Aronova, M.A., Zhang, G., Leapman, R.D., Schenck, J.F., Merkle, H. and Duyn, J.H., 2010. Layer-specific variation of iron content in cerebral cortex as a source of MRI contrast. *Proceedings of the National Academy of Sciences*, vol. 107, no. 8, pp. 3834-3839.

Gadian, D.G., 1995. *NMR and its applications to living systems.* 2nd ed. United States: Oxford Univerisity Press.

Galloway, N.R., Tong, K.A., Ashwal, S., Oyoyo, U. and Obenaus, A., 2008. Diffusion-weighted imaging improves outcome prediction in pediatric traumatic brain injury. *Journal of Neurotrauma*, vol. 25, no. 10, pp. 1153-1162.

Garwood, M. and Delabarre, L., 2001. The return of the frequency sweep: designing adiabatic pulses for contemporary NMR. *Journal of Magnetic Resonance*, vol. 153, no. 2, pp. 155-177.

Gayoso, M.J., Al-Majdalawi, A., Garrosa, M., Calvo, B. and Diaz-Flores, L., 2003. Selective calcification of rat brain lesions caused by systemic administration of kainic acid. *Histology and Histopathology*, vol. 18, no. 3, pp. 855-869.

Ghajar, J., 2000. Traumatic brain injury. *The Lancet*, vol. 356, no. 9233, pp. 923-929.

Glasel, J.A. and Lee, K., 1974. Interpretation of water nuclear magnetic resonance relaxation times in heterogeneous systems. *Journal of the American Chemical Society*, vol. 96, no. 4, pp. 970-978.

Glover, G.H., Pauly, J.M. and Bradshaw, K.M., 1992. Boron-11 imaging with a three-dimensional reconstruction method. *Journal of Magnetic Resonance Imaging*, vol. 2, no. 1, pp. 47-52.

Gochberg, D.F. and Gore, J.C., 2007. Quantitative magnetization transfer imaging via selective inversion recovery with short repetition times. *Magnetic Resonance in Medicine*, vol. 57, no. 2, pp. 437-441.

Gochberg, D.F. and Gore, J.C., 2003. Quantitative imaging of magnetization transfer using an inversion recovery sequence. *Magnetic Resonance in Medicine*, vol. 49, no. 3, pp. 501-505.

Goffin, K., Nissinen, J., Van Laere, K. and Pitkänen, A., 2007. Cyclicity of spontaneous recurrent seizures in pilocarpine model of temporal lobe epilepsy in rat. *Experimental Neurology*, vol. 205, no. 2, pp. 501-505.

Graham, S. and Henkelman, R.M., 1997. Understanding pulsed magnetization transfer. *Journal of Magnetic Resonance Imaging*, vol. 7, no. 5, pp. 903-912.

Grant, E., Hoerder-Suabedissen, A. and Molnar, Z., 2012. Development of the corticothalamic projections. *Frontiers in Neuroscience*, vol. 6, no. 53.

Greve, M.W. and Zink, B.J., 2009. Pathophysiology of traumatic brain injury. *Mount Sinai Journal of Medicine: A Journal of Translational and Personalized Medicine*, vol. 76, no. 2, pp. 97-104.

Grodzki, D.M., Jakob, P.M. and Heismann, B., 2012. Ultrashort echo time imaging using pointwise encoding time reduction with radial acquisition (PETRA). *Magnetic Resonance in Medicine*, vol. 67, no. 2, pp. 510-518.

Gronemeyer, S.A., Langston, J.W. and Hanna, S.L., 1992. MR imaging detection of calcified intracranial lesions and differentiation from iron-laden lesions. *Journal of Magnetic Resonance Imaging*, vol. 2, no. 3, pp. 271-276.

Grossman, R.I., Lisak, R.P., Macchi, P.J. and Joseph, P.M., 1987. MR of acute experimental allergic encephalomyelitis. *AJNR.American Journal of Neuroradiology*, vol. 8, no. 6, pp. 1045-1048.

Gupta, R.K., Rao, S.B., Jain, R., Pal, L., Kumar, R., Venkatesh, S.K. and Rathore, R.K.S., 2001. Differentiation of calcification from chronic hemorrhage with corrected gradient echo phase imaging. *Journal of Computer Assisted Tomography*, vol. 25, no. 5, pp. 698-704.

Haacke, E.M., Brown, R.W., Cheng, Y.N., Thompson, M.R. and Venkatesan, R., 1999. *Magnetic resonance imaging: physical principles and sequence design*. 1st ed.John Wiley & Sons.

Haacke, E.M., Cheng, N.Y., House, M.J., Liu, Q., Neelavalli, J., Ogg, R.J., Khan, A., Ayaz, M., Kirsch, W. and Obenaus, A., 2005. Imaging iron stores in the brain using magnetic resonance imaging. *Magnetic Resonance Imaging*, vol. 23, no. 1, pp. 1-25.

Haacke, E.M., Mittal, S., Wu, Z., Neelavalli, J. and Cheng, Y.C.N., 2009. Susceptibility-weighted imaging: technical aspects and clinical applications, part 1. *American Journal of Neuroradiology*, vol. 30, no. 1, pp. 19-30.

Haacke, E.M., Xu, Y., Cheng, Y.C.N. and Reichenbach, J.R., 2004. Susceptibility weighted imaging (SWI). *Magnetic Resonance in Medicine*, vol. 52, no. 3, pp. 612-618.

Haase, A., Frahm, J., Matthaei, D., Hänicke, W. and Merboldt, K., 1986. Fast NMR imaging using low flip angle pulses. FLASH imaging. *J Magn Reson*, vol. 67, pp. 258.

Hafner, S., 1994. Fast imaging in liquids and solids with the back-projection low angle shot (BLAST) technique. *Magnetic Resonance Imaging*, vol. 12, no. 7, pp. 1047-1051.

Hahn, E.L., 1950. Spin echoes. *Physical Review*, vol. 80, no. 4, pp. 580.

Han, H., Lang, N. and Pei, X., 2004. Quantitative study of differential diagnosis between acute cerebral hemorrhage and calcification by using spoiled GRE T2 dual echo MRI. *Chinese Journal of Medical Imaging Technology*, vol. 7, pp. 1.

Hanus, F. and Gillis, P., 1984. Relaxation of water adsorbed on the surface of silica powder. *Journal of Magnetic Resonance (1969)*, vol. 59, no. 3, pp. 437-445.

He, X. and Yablonskiy, D.A., 2009. Biophysical mechanisms of phase contrast in gradient echo MRI. *Proceedings of the National Academy of Sciences*, vol. 106, no. 32, pp. 13558-13563.

Helms, G., Dathe, H. and Dechent, P., 2010. Modeling the influence of TR and excitation flip angle on the magnetization transfer ratio (MTR) in human brain obtained from 3D spoiled gradient echo MRI. *Magnetic Resonance in Medicine*, vol. 64, no. 1, pp. 177-185.

Henkelman, R.M., Watts, J.F. and Kucharczyk, W., 1991. High signal intensity in MR images of calcified brain tissue. *Radiology*, vol. 179, no. 1, pp. 199-206.

Henkelman, R.M., Stanisz, G.J. and Graham, S.J., 2001. Magnetization transfer in MRI: a review. *NMR in Biomedicine*, vol. 14, no. 2, pp. 57-64.

Holland, B.A., Kucharczyk, W., Brant-Zawadzki, M., Norman, D., Haas, D.K. and Harper, P.S., 1985. MR imaging of calcified intracranial lesions. *Radiology*, vol. 157, no. 2, pp. 353-356.

Horch, R.A., Gore, J.C. and Does, M.D., 2011. Origins of the ultrashort-T2 1H NMR signals in myelinated nerve: A direct measure of myelin content?. *Magnetic Resonance in Medicine*, vol. 66, no. 1, pp. 24-31.

Idiyatullin, D., Corum, C., Moeller, S. and Garwood, M., 2008. Gapped pulses for frequency-swept MRI. *Journal of Magnetic Resonance*, vol. 193, no. 2, pp. 267-273.

Idiyatullin, D., Corum, C., Moeller, S., Prasad, H.S., Garwood, M. and Nixdorf, D.R., 2011. Dental magnetic resonance imaging: making the invisible visible. *Journal of Endodontics*, vol. 37, no. 6, pp. 745-752.

Idiyatullin, D., Corum, C., Park, J.Y. and Garwood, M., 2006. Fast and quiet MRI using a swept radiofrequency. *Journal of Magnetic Resonance*, vol. 181, no. 2, pp. 342-349.

Idiyatullin, D., Corum, C.A. and Garwood, M., 2015. Multi-Band-SWIFT. *Journal of Magnetic Resonance*, vol. 251, pp. 19-25.

Imaizumi, T., Chiba, M., Honma, T. and Niwa, J., 2003. Detection of hemosiderin deposition by T2*-weighted MRI after subarachnoid hemorrhage. *Stroke; a Journal of Cerebral Circulation*, vol. 34, no. 7, pp. 1693-1698.

Immonen, R.J., Kharatishvili, I., Niskanen, J., Gröhn, H., Pitkänen, A. and Gröhn, O.H., 2009. Distinct MRI pattern in lesional and perilesional area after traumatic brain injury in rat—11 months follow-up. *Experimental Neurology*, vol. 215, no. 1, pp. 29-40.

Iuvone, L., Mariotti, P., Colosimo, C., Guzzetta, F., Ruggiero, A. and Riccardi, R., 2002. Long-term cognitive outcome, brain computed tomography scan, and magnetic resonance imaging in children cured for acute lymphoblastic leukemia. *Cancer*, vol. 95, no. 12, pp. 2562-2570.

Jackson, J.I., Meyer, C.H., Nishimura, D.G. and Macovski, A., 1991. Selection of a convolution function for Fourier inversion using gridding
. *Medical Imaging, IEEE Transactions On*, vol. 10, no. 3, pp. 473-478.

Janve, V.A., Zu, Z., Yao, S., Li, K., Zhang, F.L., Wilson, K.J., Ou, X., Does, M.D., Subramaniam, S. and Gochberg, D.F., 2013. The radial diffusivity and magnetization transfer pool size ratio are sensitive markers for demyelination in a rat model of type III multiple sclerosis (MS) lesions. *NeuroImage*, vol. 74, pp. 298-305.

Jenkinson, M., Bannister, P., Brady, M. and Smith, S., 2002. Improved optimization for the robust and accurate linear registration and motion correction of brain images. *NeuroImage*, vol. 17, no. 2, pp. 825-841.

Jenkinson, M., Beckmann, C.F., Behrens, T.E., Woolrich, M.W. and Smith, S.M., 2012. Fsl. *NeuroImage*, vol. 62, no. 2, pp. 782-790.

Jenkinson, M. and Smith, S., 2001. A global optimisation method for robust affine registration of brain images. *Medical Image Analysis*, vol. 5, no. 2, pp. 143-156.

Johnson, K.O. and Pipe, J.G., 2009. Convolution kernel design and efficient algorithm for sampling density correction. *Magnetic Resonance in Medicine*, vol. 61, no. 2, pp. 439-447.

Jones, D.K., 2010. *Diffusion tensor imaging*. 1st ed. New York: Oxford University Press.

Jones, D.K., 2004. The effect of gradient sampling schemes on measures derived from diffusion tensor MRI: a Monte Carlo study. *Magnetic Resonance in Medicine*, vol. 51, no. 4, pp. 807-815.

Jones, D.K., Knösche, T.R. and Turner, R., 2013. White matter integrity, fiber count, and other fallacies: the do's and don'ts of diffusion MRI. *NeuroImage*, vol. 73, pp. 239-254.

Kabadi, S.V., Hilton, G.D., Stoica, B.A., Zapple, D.N. and Faden, A.I., 2010. Fluid-percussion-induced traumatic brain injury model in rats. *Nature Protocols*, vol. 5, no. 9, pp. 1552-1563.

Kato, H., Izumiyama, M., Izumiyama, K., Takahashi, A. and Itoyama, Y., 2002. Silent cerebral microbleeds on T2*-weighted MRI: correlation with stroke subtype, stroke recurrence, and leukoaraiosis. *Stroke*, vol. 33, no. 6, pp. 1536-1540.

Keller, A., Westenberger, A., Sobrido, M.J., García-Murias, M., Domingo, A., Sears, R.L., Lemos, R.R., Ordoñez-Ugalde, A., Nicolas, G. and da Cunha, José E Gomes, 2013. Mutations in the gene encoding PDGF-B cause brain calcifications in humans and mice. *Nature Genetics*, vol. 45, no. 9, pp. 1077-1082.

Kendi, A.T.K., Khariwala, S.S., Zhang, J., Idiyatullin, D.S., Corum, C.A., Michaeli, S., Pambuccian, S.E., Garwood, M. and Yueh, B., 2011. Transformation in mandibular imaging with sweep imaging with fourier transform magnetic resonance imaging. *Archives of Otolaryngology–Head & Neck Surgery*, vol. 137, no. 9, pp. 916-919.

Kharatishvili, I., Nissinen, J.P., McIntosh, T.K. and Pitkänen, A., 2006. A model of posttraumatic epilepsy induced by lateral fluid-percussion brain injury in rats. *Neuroscience*, vol. 140, no. 2, pp. 685-697.

Kimura, H., Meaney, D.F., McGowan, J.C., Grossman, R.I., Lenkinski, R.E., Ross, D.T., McIntosh, T.K., Gennarelli, T.A. and Smith, D.H., 1996. Magnetization transfer imaging of diffuse axonal injury following experimental brain injury in the pig: characterization by magnetization transfer ratio with histopathologic correlation. *Journal of Computer Assisted Tomography*, vol. 20, no. 4, pp. 540-546.

Kinnunen, K.M., Greenwood, R., Powell, J.H., Leech, R., Hawkins, P.C., Bonnelle, V., Patel, M.C., Counsell, S.J. and Sharp, D.J., 2011. White matter damage and cognitive impairment after traumatic brain injury. *Brain : A Journal of Neurology*, vol. 134, no. 2, pp. 449-463.

Kinoshita, T., Okudera, T., Tamura, H., Ogawa, T. and Hatazawa, J., 2000. Assessment of lacunar hemorrhage associated with hypertensive stroke by echo-planar gradient-echo T2*-weighted MRI. *Stroke; a Journal of Cerebral Circulation*, vol. 31, no. 7, pp. 1646-1650.

Kjos, B.O., Brant-Zawadzki, M., Kucharczyk, W., Kelly, W.M., Norman, D. and Newton, T.H., 1985. Cystic intracranial lesions: magnetic resonance imaging. *Radiology*, vol. 155, no. 2, pp. 363-369.

Kobayashi, N., Idiyatullin, D., Corum, C., Weber, J., Garwood, M. and Sachdev, D., 2014. SWIFT MRI enhances detection of breast cancer metastasis to the lung. *Magnetic Resonance in Medicine*, vol. 73, no. 5, pp. 1812-1819.

Kochunov, P., Jahanshad, N., Marcus, D., Winkler, A., Sprooten, E., Nichols, T.E., Wright, S.N., Hong, L.E., Patel, B. and Behrens, T., 2015. Heritability of fractional anisotropy in human white matter: A comparison of Human Connectome Project and ENIGMA-DTI data. *NeuroImage*, vol. 111, pp. 300-311.

Koenig, S.H., 1991. Cholesterol of myelin is the determinant of gray-white contrast in MRI of brain. *Magnetic Resonance in Medicine*, vol. 20, no. 2, pp. 285-291.

Kraus, M.F., Susmaras, T., Caughlin, B.P., Walker, C.J., Sweeney, J.A. and Little, D.M., 2007. White matter integrity and cognition in chronic traumatic brain injury: a diffusion tensor imaging study. *Brain*, vol. 130, no. 10, pp. 2508-2519.

Kuethe, D.O., Adolphi, N.L. and Fukushima, E., 2007. Short data-acquisition times improve projection images of lung tissue. *Magnetic Resonance in Medicine*, vol. 57, no. 6, pp. 1058-1064.

Kumar, A., Welti, D. and Ernst, R.R., 1975. NMR Fourier zeugmatography. *Journal of Magnetic Resonance*, vol. 213, no. 2, pp. 495-509.

Kumar, R., Gupta, R.K., Rao, S.B., Chawla, S., Husain, M. and Rathore, R.K., 2003. Magnetization transfer and T2 quantitation in normal appearing cortical gray matter and white matter adjacent to focal abnormality in patients with traumatic brain injury. *Magnetic Resonance Imaging*, vol. 21, no. 8, pp. 893-899.

Lafreniere, G.F., Peredery, O. and Persinger, M.A., 1992. Progressive accumulation of large aggregates of calcium-containing polysaccharides and basophilic debris within specific thalamic nuclei after lithium/pilocarpine-induced seizures. *Brain Research Bulletin*, vol. 28, no. 5, pp. 825-830.

Lago, E., Baldisserotto, M., Hoefel Filho, J., Santiago, D. and Jungblut, R., 2007. Agreement between ultrasonography and computed tomography in detecting intracranial calcifications in congenital toxoplasmosis. *Clinical Radiology*, vol. 62, no. 10, pp. 1004-1011.

Laitinen, T., Sierra, A., Bolkvadze, T., Pitkänen, A. and Gröhn, O., 2015. Diffusion tensor imaging detects chronic microstructural changes in white and gray matter after traumatic brain injury in rat. *Frontiers in Neuroscience*, vol. 9, no. 128.

Laitinen, T., Sierra, A., Pitkänen, A. and Gröhn, O., 2010. Diffusion tensor MRI of axonal plasticity in the rat hippocampus. *NeuroImage*, vol. 51, no. 2, pp. 521-530.

Langkammer, C., Liu, T., Khalil, M., Enzinger, C., Jehna, M., Fuchs, S., Fazekas, F., Wang, Y. and Ropele, S., 2013. Quantitative susceptibility mapping in multiple sclerosis. *Radiology*, vol. 267, no. 2, pp. 551-559.

Langkammer, C., Schweser, F., Krebs, N., Deistung, A., Goessler, W., Scheurer, E., Sommer, K., Reishofer, G., Yen, K. and Fazekas, F., 2012. Quantitative susceptibility mapping (QSM) as a means to measure brain iron? A post mortem validation study. *NeuroImage*, vol. 62, no. 3, pp. 1593-1599.

Larkman, D.J., Hajnal, J.V., Herlihy, A.H., Coutts, G.A., Young, I.R. and Ehnholm, G., 2001. Use of multicoil arrays for separation of signal from multiple slices simultaneously excited. *Journal of Magnetic Resonance Imaging*, vol. 13, no. 2, pp. 313-317.

Larson, P.E.Z., Conolly, S.M., Pauly, J.M. and Nishimura, D.G., 2007. Using adiabatic inversion pulses for long-T2 suppression in ultrashort echo time (UTE) imaging. *Magnetic Resonance in Medicine*, vol. 58, no. 5, pp. 952-961.

Larson, P.E.Z., Gurney, P.T., Nayak, K., Gold, G.E., Pauly, J.M. and Nishimura, D.G., 2006. Designing long-T 2 suppression pulses for ultrashort echo time imaging. *Magnetic Resonance in Medicine*, vol. 56, no. 1, pp. 94-103.

Lauterbur, P.C., 1973. Image formation by induced local interactions: examples employing nuclear magnetic resonance. *Nature*, vol. 242, no. 5394, pp. 190-191.

Le Bihan, D., Breton, E., Lallemand, D., Grenier, P., Cabanis, E. and Laval-Jeantet, M., 1986. MR imaging of intravoxel incoherent motions: application to diffusion and perfusion in neurologic disorders. *Radiology*, vol. 161, no. 2, pp. 401-407.

Lee, H., Wintermark, M., Gean, A.D., Ghajar, J., Manley, G.T. and Mukherjee, P., 2008. Focal lesions in acute mild traumatic brain injury and neurocognitive outcome: CT versus 3T MRI. *Journal of Neurotrauma*, vol. 25, no. 9, pp. 1049-1056.

Lee, J., Shmueli, K., Fukunaga, M., van Gelderen, P., Merkle, H., Silva, A.C. and Duyn, J.H., 2010a. Sensitivity of MRI resonance frequency to the orientation of brain tissue microstructure. *Proceedings of the National Academy of Sciences*, vol. 107, no. 11, pp. 5130-5135.

Lee, J., Fukunaga, M. and Duyn, J.H., 2011a. Improving contrast to noise ratio of resonance frequency contrast images (phase images) using balanced steady-state free precession. *NeuroImage*, vol. 54, no. 4, pp. 2779-2788.

Lee, J., Hirano, Y., Fukunaga, M., Silva, A.C. and Duyn, J.H., 2010b. On the contribution of deoxy-hemoglobin to MRI gray–white matter phase contrast at high field. *NeuroImage*, vol. 49, no. 1, pp. 193-198.

Lee, J., Shmueli, K., Kang, B., Yao, B., Fukunaga, M., van Gelderen, P., Palumbo, S., Bosetti, F., Silva, A.C. and Duyn, J.H., 2012. The contribution of myelin to magnetic susceptibility-weighted contrasts in high-field MRI of the brain. *NeuroImage*, vol. 59, no. 4, pp. 3967-3975.

Lee, J., van Gelderen, P., Kuo, L., Merkle, H., Silva, A.C. and Duyn, J.H., 2011b. T_2*-based fiber orientation mapping. *NeuroImage*, vol. 57, no. 1, pp. 225-234.

Lehto, L.J., I. Djaudat, C.A. Corum, M. Garwood and O.H. Gröhn. MRI detection of short T2 component in brain by SWIFT.*Proceedings of the 18th Annual Meeting of ISMRM*. Stockholm, Sweden, 2010.

Leunissen, I., Coxon, J.P., Caeyenberghs, K., Michiels, K., Sunaert, S. and Swinnen, S.P., 2014. Task switching in traumatic brain injury relates to cortico-subcortical integrity. *Human Brain Mapping*, vol. 35, no. 5, pp. 2459-2469.

Leutritz, T., Hilfert, L., Smalla, K., Speck, O. and Zhong, K., 2013. Accurate quantification of water–macromolecule exchange induced frequency shift: Effects of reference substance. *Magnetic Resonance in Medicine*, vol. 69, no. 1, pp. 263-268.

Levin, J.J., 1926. Intracerebral calcification. *British Journal of Surgery*, vol. 14, no. 54, pp. 215-223.

Levitt, M.H., 2001. *Spin Dynamics - Basics of Nuclear Magnetic Resonance.* 1st ed. England: Wiley.

Li, J., Li, X., Feng, D. and Gu, L., 2011. Quantitative evaluation of microscopic injury with diffusion tensor imaging in a rat model of diffuse axonal injury. *European Journal of Neuroscience*, vol. 33, no. 5, pp. 933-945.

Li, W., J. Long, L. Watts, Q. Shen and T.Q. Duong. Longitudinal changes of white matter following mild traumatic brain injury by diffusion, T2 and susceptibility MRI*Proceedings of the 23rd Annual Meeting of ISMRM*. Toronto, 2015.

Li, W., Wu, B., Avram, A.V. and Liu, C., 2012. Magnetic susceptibility anisotropy of human brain in vivo and its molecular underpinnings. *NeuroImage*, vol. 59, no. 3, pp. 2088-2097.

Lievens, J., Bernal, F., Forni, C., Mahy, N. and Goff, K., 2000. Characterization of striatal lesions produced by glutamate uptake alteration: cell death, reactive gliosis, and changes in GLT1 and GADD45 mRNA expression. *Glia*, vol. 29, no. 3, pp. 222-232.

Likes, R.S., 1981. *Moving Gradient Zeugmatography*.

Lim, I.A.L., Li, X., Jones, C.K., Farrell, J.A., Vikram, D.S. and van Zijl, P.C., 2014. Quantitative magnetic susceptibility mapping without phase unwrapping using WASSR. *NeuroImage*, vol. 86, pp. 265-279.

Lin, W., Guo, J., Rosen, M.A. and Song, H.K., 2008. Respiratory motion-compensated radial dynamic contrast-enhanced (DCE)-MRI of chest and abdominal lesions. *Magnetic Resonance in Medicine*, vol. 60, no. 5, pp. 1135-1146.

Liu, C., Li, W., Johnson, G.A. and Wu, B., 2011. High-field (9.4 T) MRI of brain dysmyelination by quantitative mapping of magnetic susceptibility. *NeuroImage*, vol. 56, no. 3, pp. 930-938.

Liu, T., Surapaneni, K., Lou, M., Cheng, L., Spincemaille, P. and Wang, Y., 2012. Cerebral microbleeds: burden assessment by using quantitative susceptibility mapping. *Radiology*, vol. 262, no. 1, pp. 269-278.

Löbel, U., Sedlacik, J., Sabin, N.D., Kocak, M., Broniscer, A., Hillenbrand, C.M. and Patay, Z., 2010. Three-dimensional susceptibility-weighted imaging and two-dimensional T2*-weighted gradient-echo imaging of intratumoral hemorrhages in pediatric diffuse intrinsic pontine glioma. *Neuroradiology*, vol. 52, no. 12, pp. 1167-1177.

Lodygensky, G.A., Marques, J.P., Maddage, R., Perroud, E., Sizonenko, S.V., Hüppi, P.S. and Gruetter, R., 2012. In vivo assessment of myelination by phase imaging at high magnetic field. *NeuroImage*, vol. 59, no. 3, pp. 1979-1987.

Lounila, J., Ala-Korpela, M., Jokisaari, J., Savolainen, M. and Kesäniemi, Y., 1994. Effects of orientational order and particle size on the NMR line positions of lipoproteins. *Physical Review Letters*, vol. 72, no. 25, pp. 4049.

Luhach, I., Idiyatullin, D., Lynch, C.C., Corum, C., Martinez, G.V., Garwood, M. and Gillies, R.J., 2014. Rapid ex vivo imaging of PAIII prostate to bone tumor with SWIFT-MRI. *Magnetic Resonance in Medicine*, vol. 72, no. 3, pp. 858-863.

Luo, J., He, X., d'Avignon, D.A., Ackerman, J.J.H. and Yablonskiy, D.A., 2010. Protein-induced water 1H MR frequency shifts: Contributions from magnetic susceptibility and exchange effects. *Journal of Magnetic Resonance*, vol. 202, pp. 102-108.

Luo, J., He, X. and Yablonskiy, D., 2014. Magnetic susceptibility induced white matter MR signal frequency shifts—experimental comparison between Lorentzian sphere and generalized Lorentzian approaches. *Magnetic Resonance in Medicine*, vol. 71, no. 3, pp. 1251-1263.

Lustig, M., Donoho, D. and Pauly, J.M., 2007. Sparse MRI: The application of compressed sensing for rapid MR imaging. *Magnetic Resonance in Medicine*, vol. 58, no. 6, pp. 1182-1195.

Maas, A.I., Stocchetti, N. and Bullock, R., 2008. Moderate and severe traumatic brain injury in adults. *The Lancet Neurology*, vol. 7, no. 8, pp. 728-741.

Mac Donald, C., Dikranian, K., Song, S., Bayly, P., Holtzman, D. and Brody, D., 2007a. Detection of traumatic axonal injury with diffusion tensor imaging in a mouse model of traumatic brain injury. *Experimental Neurology*, vol. 205, no. 1, pp. 116-131.

Mac Donald, C.L., Dikranian, K., Bayly, P., Holtzman, D. and Brody, D., 2007b. Diffusion tensor imaging reliably detects experimental traumatic axonal injury and indicates approximate time of injury. *The Journal of Neuroscience*, vol. 27, no. 44, pp. 11869-11876.

MacDonald, H.L., Bell, B.A., Smith, M.A., Kean, D.M., Tocher, J.L., Douglas, R.H.B., Miller, J.D. and Best, J.J.K., 1986. Correlation of human NMR T1 values measured in vivo and brain water content. *British Journal of Radiology*, vol. 59, no. 700, pp. 355-357.

Macedo, C.E., Angst, M., Guiberteau, T., Brasse, D., O'Brien, T.J. and Sandner, G., 2010. Acoustic hypersensitivity in adult rats after neonatal ventral hippocampus lesions. *Behavioural Brain Research*, vol. 207, no. 1, pp. 161-168.

Mackay, A., Whittall, K., Adler, J., Li, D., Paty, D. and Graeb, D., 1994. In vivo visualization of myelin water in brain by magnetic resonance. *Magnetic Resonance in Medicine*, vol. 31, no. 6, pp. 673-677.

Mäkinen, S., Van Groen, T., Clarke, J., Thornell, A., Corbett, D., Hiltunen, M., Soininen, H. and Jolkkonen, J., 2007. Coaccumulation of calcium and β-amyloid in the thalamus after transient middle cerebral artery occlusion in rats. *Journal of Cerebral Blood Flow & Metabolism*, vol. 28, no. 2, pp. 263-268.

Mamere, A.E., Saraiva, L.A., Matos, A.L., Carneiro, A.A. and Santos, A.C., 2009. Evaluation of delayed neuronal and axonal damage secondary to moderate and severe traumatic brain injury using quantitative MR imaging techniques. *American Journal of Neuroradiology*, vol. 30, no. 5, pp. 947-952.

Mansfield, P. and Maudsley, A., 1977. Planar spin imaging by NMR. *Journal of Magnetic Resonance (1969)*, vol. 27, no. 1, pp. 101-119.

Marjanska, M., Waks, M., Snyder, C.J. and Vaughan, J.T., 2008. Multinuclear NMR investigation of probe construction materials at 9.4 T. *Magnetic Resonance in Medicine*, vol. 59, no. 4, pp. 936-938.

Marques, J.P. and Bowtell, R., 2005. Application of a Fourier-based method for rapid calculation of field inhomogeneity due to spatial variation of magnetic susceptibility. *Concepts in Magnetic Resonance Part B: Magnetic Resonance Engineering*, vol. 25, no. 1, pp. 65-78.

Marques, J.P., Maddage, R., Mlynarik, V. and Gruetter, R., 2009. On the origin of the MR image phase contrast: an in vivo MR microscopy study of the rat brain at 14.1 T. *NeuroImage*, vol. 46, no. 2, pp. 345-352.

Marshall, L.F., Gautille, T., Klauber, M.R., Eisenberg, H.M., Jane, J.A., Luerssen, T.G., Marmarou, A. and Foulkes, M.A., 1991. The outcome of severe closed head injury. *Special Supplements*, vol. 75, no. 1s, pp. s28-s36.

McGowan, J.C., Berman, J.I., Ford, J.C., Lavi, E. and Hackney, D.B., 2000a. Characterization of experimental spinal cord injury with magnetization transfer ratio histograms. *Journal of Magnetic Resonance Imaging*, vol. 12, no. 2, pp. 247-254.

McGowan, J.C., McCormack, T.M., Grossman, R.I., Mendonça, R., Chen, X., Berlin, J.A., Meaney, D.F., Xu, B., Cecil, K.M. and McIntosh, T.K., 1999. Diffuse axonal pathology detected

with magnetization transfer imaging following brain injury in the pig. *Magnetic Resonance in Medicine*, vol. 41, no. 4, pp. 727-733.

McGowan, J.C., Yang, J.H., Plotkin, R.C., Grossman, R.I., Umile, E.M., Cecil, K.M. and Bagley, L.J., 2000b. Magnetization transfer imaging in the detection of injury associated with mild head trauma. *American Journal of Neuroradiology*, vol. 21, no. 5, pp. 875-880.

McIntosh, T., Vink, R., Noble, L., Yamakami, I., Fernyak, S., Soares, H. and Faden, A., 1989. Traumatic brain injury in the rat: characterization of a lateral fluid-percussion model. *Neuroscience*, vol. 28, no. 1, pp. 233-244.

McMillan, T.M. and Herbert, C.M., 2004. Further recovery in a potential treatment withdrawal case 10 years after brain injury. *Brain Injury*, vol. 18, no. 9, pp. 935-940.

Melville, D., Qian, J., Millet, D., Nelson, C., Pilcher, W., Powers, J.M. and Shrier, D.A., 1999. Fibro-osseous lesions involving the brain: MRI. *Neuroradiology*, vol. 41, no. 1, pp. 18-21.

Miguel, O.B., Gossuin, Y., Morales, M., Gillis, P., Muller, R. and Veintemillas-Verdaguer, S., 2007. Comparative analysis of the 1 H NMR relaxation enhancement produced by iron oxide and core-shell iron–iron oxide nanoparticles. *Magnetic Resonance Imaging*, vol. 25, no. 10, pp. 1437-1441.

Mittal, S., Wu, Z., Neelavalli, J. and Haacke, E.M., 2009. Susceptibility-weighted imaging: technical aspects and clinical applications, part 2. *American Journal of Neuroradiology*, vol. 30, no. 2, pp. 232.

Murphy, J.T., 1928. Intracranial Calcifications 1. *Radiology*, vol. 11, no. 3, pp. 213-216.

Nandigam, R.N., Viswanathan, A., Delgado, P., Skehan, M.E., Smith, E.E., Rosand, J., Greenberg, S.M. and Dickerson, B.C., 2009. MR imaging detection of cerebral microbleeds: effect of susceptibility-weighted imaging, section thickness, and field strength. *American Journal of Neuroradiology*, vol. 30, no. 2, pp. 338-343.

Nishimura, D.G., 2010. *Principles of Magnetic Resonance Imaging*. 1.1st ed.

Nissi, M.J., Lehto, L.J., Corum, C.A., Idiyatullin, D., Ellermann, J.M., Gröhn, O.H. and Nieminen, M.T., 2014. Measurement of T1 relaxation time of osteochondral specimens using VFA-SWIFT. *Magnetic Resonance in Medicine*, vol. 74, no. 1, pp. 175-184.

Nitsch, C. and Scotti, A.L., 1992. Ibotenic acid-induced calcium deposits in rat substantia nigra. Ultrastructure of their time-dependent formation. *Acta Neuropathologica*, vol. 85, no. 1, pp. 55-70.

Noll, D.C., Nishimura, D.G. and Macovski, A., 1991. Homodyne detection in magnetic resonance imaging. *Medical Imaging, IEEE Transactions On*, vol. 10, no. 2, pp. 154-163.

Norman, D., Diamond, C. and Boyd, D., 1978. Relative detectability of intracranial calcifications on computed tomography and skull radiography. *Journal of Computer Assisted Tomography*, vol. 2, no. 1, pp. 61-64.

Nute, J.L., Le Roux, L., Chandler, A.G., Baladandayuthapani, V., Schellingerhout, D. and Cody, D.D., 2015. Differentiation of low-attenuation intracranial hemorrhage and calcification using dual-energy computed tomography in a phantom system. *Investigative Radiology*, vol. 50, no. 1, pp. 9-16.

Ogg, R.J., Langston, J.W., Haacke, E.M., Steen, R.G. and Taylor, J.S., 1999. The correlation between phase shifts in gradient-echo MR images and regional brain iron concentration. *Magnetic Resonance Imaging*, vol. 17, no. 8, pp. 1141-1148.

Okuchi, K., Hiramatsu, K., Morimoto, T., Tsunoda, S., Sakaki, T. and Iwasaki, S., 1992. Astrocytoma with widespread calcification along axonal fibres. *Neuroradiology*, vol. 34, no. 4, pp. 328-330.

Oliveira, A., Hodges, H. and Rezaie, P., 2003. Excitotoxic lesioning of the rat basal forebrain with S-AMPA: consequent mineralization and associated glial response. *Experimental Neurology*, vol. 179, no. 2, pp. 127-138.

Oot, R.F., New, P.F., Pile-Spellman, J., Rosen, B.R., Shoukimas, G.M. and Davis, K.R., 1986. The detection of intracranial calcifications by MR. *American Journal of Neuroradiology*, vol. 7, no. 5, pp. 801-809.

Osteen, C.L., Moore, A.H., Prins, M.L. and Hovda, D.A., 2001. Age-dependency of 45calcium accumulation following lateral fluid percussion: acute and delayed patterns. *Journal of Neurotrauma*, vol. 18, no. 2, pp. 141-162.

Ou, X., Sun, S., Liang, H., Song, S. and Gochberg, D.F., 2009. The MT pool size ratio and the DTI radial diffusivity may reflect the myelination in shiverer and control mice. *NMR in Biomedicine*, vol. 22, no. 5, pp. 480-487.

Parisi, J., Place, C. and Nag, S., 1988. Calcification in a recent cerebral infarct--radiologic and pathologic correlation. *The Canadian Journal of Neurological Sciences.Le Journal Canadien Des Sciences Neurologiques*, vol. 15, no. 2, pp. 152-155.

Park, J.Y., DelaBarre, L. and Garwood, M., 2006. Improved gradient-echo 3D magnetic resonance imaging using pseudo-echoes created by frequency-swept pulses. *Magnetic Resonance in Medicine*, vol. 55, no. 4, pp. 848-857.

Park, J.Y. and Garwood, M., 2009. Spin-echo MRI using $\pi/2$ and π hyperbolic secant pulses. *Magnetic Resonance in Medicine*, vol. 61, no. 1, pp. 175-187.

Park, J.Y., Moeller, S., Goerke, U., Auerbach, E., Chamberlain, R., Ellermann, J. and Garwood, M., 2011. Short echo-time 3D radial gradient-echo MRI using concurrent dephasing and excitation. *Magnetic Resonance in Medicine*, vol. 67, no. 2, pp. 428-436.

Pauly, J., S. Conolly, D. Nishimura and A. Macovski. Slice-selective excitation for very short T2 species*Proceedings of SMRM*, 1989a.

Pauly, J., Nishimura, D. and Macovski, A., 1989b. A k-space analysis of small-tip-angle excitation. *Journal of Magnetic Resonance*, vol. 81, no. 1, pp. 43-56.

Petegnief, V., Saura, J., Dewar, D., Cummins, D., Dragunow, M. and Mahy, N., 1999. Long-term effects of α-amino-3-hydroxy-5-methyl-4-isoxazole propionate and 6-nitro-7-sulphamoylbenzo (f) quinoxaline-2, 3-dione in the rat basal ganglia: calcification, changes in glutamate receptors and glial reactions. *Neuroscience*, vol. 94, no. 1, pp. 105-115.

Pfefferbaum, A., Adalsteinsson, E., Rohlfing, T. and Sullivan, E.V., 2010. Diffusion tensor imaging of deep gray matter brain structures: effects of age and iron concentration. *Neurobiology of Aging*, vol. 31, no. 3, pp. 482-493.

Pierce, J.E.S., Smith, D.H., Trojanowski, J.Q. and McIntosh, T.K., 1998. Enduring cognitive, neurobehavioral and histopathological changes persist for up to one year following severe experimental brain injury in rats. *Neuroscience*, vol. 87, no. 2, pp. 359-369.

Pinton, G., Aubry, J., Bossy, E., Muller, M., Pernot, M. and Tanter, M., 2012. Attenuation, scattering, and absorption of ultrasound in the skull bone. *Medical Physics*, vol. 39, no. 1, pp. 299-307.

Provenzale, J.M., 2010. Imaging of traumatic brain injury: a review of the recent medical literature. *American Journal of Roentgenology*, vol. 194, no. 1, pp. 16-19.

Pruessmann, K.P., Weiger, M., Scheidegger, M.B. and Boesiger, P., 1999. SENSE: sensitivity encoding for fast MRI. *Magnetic Resonance in Medicine*, vol. 42, no. 5, pp. 952-962.

Rahmer, J., Bornert, P., Groen, J. and Bos, C., 2006. Three-dimensional radial ultrashort echo-time imaging with T 2 adapted sampling. *Magnetic Resonance in Medicine*, vol. 55, no. 5, pp. 1075-1082.

Ramonet, D., de Yebra, L., Fredriksson, K., Bernal, F., Ribalta, T. and Mahy, N., 2006. Similar calcification process in acute and chronic human brain pathologies. *Journal of Neuroscience Research*, vol. 83, no. 1, pp. 147-156.

Rasche, V., Boer, R.W.D., Holz, D. and Proksa, R., 1995. Continuous radial data acquisition for dynamic MRI. *Magnetic Resonance in Medicine*, vol. 34, no. 5, pp. 754-761.

Rautiainen, J., Lehto, L.J., Tiitu, V., Kiekara, O., Pulkkinen, H., Brünott, A., van Weeren, R., Brommer, H., Brama, P.A. and Ellermann, J., 2013. Osteochondral repair: evaluation with sweep imaging with fourier transform in an equine model. *Radiology*, vol. 269, no. 1, pp. 113-121.

Robson, M.D., Gatehouse, P.D., Bydder, M. and Bydder, G.M., 2003. Magnetic resonance: an introduction to ultrashort TE (UTE) imaging. *J Comput Assist Tomogr*, vol. 27, no. 6, pp. 825-846.

Rudko, D.A., Klassen, L.M., de Chickera, S.N., Gati, J.S., Dekaban, G.A. and Menon, R.S., 2014. Origins of orientation dependence in gray and white matter. *Proceedings of the National Academy of Sciences*, vol. 111, no. 1, pp. 159-167.

Rulseh, A.M., Keller, J., Tintěra, J., Kožíšek, M. and Vymazal, J., 2013. Chasing shadows: what determines DTI metrics in gray matter regions? An in vitro and in vivo study. *Journal of Magnetic Resonance Imaging*, vol. 38, no. 5, pp. 1103-1110.

Saini, J., Kesavadas, C., Thomas, B., Kapilamoorthy, T.R., Gupta, A.K., Radhakrishnan, A. and Radhakrishnan, K., 2009. Susceptibility weighted imaging in the diagnostic evaluation of patients with intractable epilepsy. *Epilepsia*, vol. 50, no. 6, pp. 1462-1473.

Salomir, R., de Senneville, B.D. and Moonen, C.T., 2003. A fast calculation method for magnetic field inhomogeneity due to an arbitrary distribution of bulk susceptibility. *Concepts in Magnetic Resonance Part B: Magnetic Resonance Engineering*, vol. 19, no. 1, pp. 26-34.

Sandner, G., Angst, M.J., Guiberteau, T., Guignard, B. and Brasse, D., 2010. MRI and X-ray scanning images of the brain of 3-, 6-and 9-month-old rats with bilateral neonatal ventral hippocampus lesions. *NeuroImage*, vol. 53, no. 1, pp. 44-50.

Santin, M.D., A. Petiet, E. Laffrat, S. Lehéricy, C. François and S. Hunot. Quantitative Susceptibility Mapping of the Squirrel Monkey at 3T and 11.7T: Application to a Model of Parkinson's Disease*Proceedings of the 23rd Annual Meeting of ISMRM*. Toronto, 2015.

Sati, P., Gelderen, P.v., Silva, A.C., Reich, D.S., Merkle, H., de Zwart, J.A. and Duyn, J.H., 2013. Micro-compartment specific T2* relaxation in the brain. *NeuroImage*, vol. 15, pp. 268-278.

Sati, P., Silva, A.C., van Gelderen, P., Gaitan, M.I., Wohler, J.E., Jacobson, S., Duyn, J.H. and Reich, D.S., 2012. In vivo quantification of T_2* anisotropy in white matter fibers in marmoset monkeys. *NeuroImage*, vol. 59, no. 2, pp. 979-985.

Sattler, R. and Tymianski, M., 2000. Molecular mechanisms of calcium-dependent excitotoxicity. *Journal of Molecular Medicine*, vol. 78, no. 1, pp. 3-13.

Scheid, R., Preul, C., Gruber, O., Wiggins, C. and Von Cramon, D.Y., 2003. Diffuse axonal injury associated with chronic traumatic brain injury: evidence from T2*-weighted gradient-echo imaging at 3 T. *American Journal of Neuroradiology*, vol. 24, no. 6, pp. 1049-1056.

Schweser, F., Deistung, A., Lehr, B.W. and Reichenbach, J.R., 2010. Differentiation between diamagnetic and paramagnetic cerebral lesions based on magnetic susceptibility mapping. *Medical Physics*, vol. 37, no. 10, pp. 5165-5178.

Schweser, F., Deistung, A., Lehr, B.W. and Reichenbach, J.R., 2011. Quantitative imaging of intrinsic magnetic tissue properties using MRI signal phase: an approach to in vivo brain iron metabolism?. *NeuroImage*, vol. 54, no. 4, pp. 2789-2807.

Sedghizadeh, P., Nguyen, M. and Enciso, R., 2014. Intracranial physiological calcifications evaluated with cone beam CT. *Dentomaxillofacial Radiology*, vol. 41, pp. 675-678.

Seehaus, A., Roebroeck, A., Bastiani, M., Fonseca, L., Bratzke, H., Lori, N., Vilanova, A., Goebel, R. and Galuske, R., 2015. Histological validation of high-resolution DTI in human post mortem tissue. *Frontiers in Neuroanatomy*, vol. 9, no. 98.

Sharp, D.J., Scott, G. and Leech, R., 2014. Network dysfunction after traumatic brain injury. *Nature Reviews Neurology*, vol. 10, no. 3, pp. 156-166.

Shimizu, A., Ikeguchi, M. and Sugai, S., 1994. Appropriateness of DSS and TSP as internal references for 1H NMR studies of molten globule proteins in aqueous media. *Journal of Biomolecular NMR*, vol. 4, no. 6, pp. 859-862.

Shirotani, T., Shima, K., Iwata, M., Kita, H. and Chigasaki, H., 1994. Calcium accumulation following middle cerebral artery occlusion in stroke-prone spontaneously hypertensive rats. *Journal of Cerebral Blood Flow and Metabolism*, vol. 14, no. 5, pp. 831-836.

Shmueli, K., de Zwart, J.A., van Gelderen, P., Li, T.Q., Dodd, S.J. and Duyn, J.H., 2009. Magnetic susceptibility mapping of brain tissue in vivo using MRI phase data. *Magnetic Resonance in Medicine*, vol. 62, no. 6, pp. 1510-1522.

Shmueli, K., Dodd, S.J., Li, T.Q. and Duyn, J.H., 2011. The contribution of chemical exchange to MRI frequency shifts in brain tissue. *Magnetic Resonance in Medicine*, vol. 65, no. 1, pp. 35-43.

Sidaros, A., Engberg, A.W., Sidaros, K., Liptrot, M.G., Herning, M., Petersen, P., Paulson, O.B., Jernigan, T.L. and Rostrup, E., 2008. Diffusion tensor imaging during recovery from severe traumatic brain injury and relation to clinical outcome: a longitudinal study. *Brain*, vol. 131, no. 2, pp. 559-572.

Sierra, A., Laitinen, T., Gröhn, O. and Pitkänen, A., 2013. Diffusion tensor imaging of hippocampal network plasticity. *Brain Structure and Function*, vol. 220, no. 2, pp. 781-801.

Sinson, G., Bagley, L.J., Cecil, K.M., Torchia, M., McGowan, J.C., Lenkinski, R.E., McIntosh, T.K. and Grossman, R.I., 2001. Magnetization transfer imaging and proton MR spectroscopy in the evaluation of axonal injury: correlation with clinical outcome after traumatic brain injury. *American Journal of Neuroradiology*, vol. 22, no. 1, pp. 143-151.

Sled, J.G. and Pike, G.B., 2001. Quantitative imaging of magnetization transfer exchange and relaxation properties in vivo using MRI. *Magnetic Resonance in Medicine*, vol. 46, no. 5, pp. 923-931.

Sled, J.G. and Pike, G.B., 2000. Quantitative interpretation of magnetization transfer in spoiled gradient echo MRI sequences. *Journal of Magnetic Resonance*, vol. 145, no. 1, pp. 24-36.

Song, S., Sun, S., Ju, W., Lin, S., Cross, A.H. and Neufeld, A.H., 2003. Diffusion tensor imaging detects and differentiates axon and myelin degeneration in mouse optic nerve after retinal ischemia. *NeuroImage*, vol. 20, no. 3, pp. 1714-1722.

Song, S., Sun, S., Ramsbottom, M.J., Chang, C., Russell, J. and Cross, A.H., 2002. Dysmyelination revealed through MRI as increased radial (but unchanged axial) diffusion of water. *NeuroImage*, vol. 17, no. 3, pp. 1429-1436.

Song, S., Yoshino, J., Le, T.Q., Lin, S., Sun, S., Cross, A.H. and Armstrong, R.C., 2005. Demyelination increases radial diffusivity in corpus callosum of mouse brain. *NeuroImage*, vol. 26, no. 1, pp. 132-140.

Sotak, C.H., 2004. Nuclear magnetic resonance (NMR) measurement of the apparent diffusion coefficient (ADC) of tissue water and its relationship to cell volume changes in pathological states. *Neurochemistry International*, vol. 45, no. 4, pp. 569-582.

Stanisz, G., Kecojevic, A., Bronskill, M. and Henkelman, R., 1999. Characterizing white matter with magnetization transfer and T2. *Magnetic Resonance in Medicine*, vol. 42, no. 6, pp. 1128-1136.

Stejskal, E. and Tanner, J., 1965. Spin diffusion measurements: spin echoes in the presence of a time-dependent field gradient. *The Journal of Chemical Physics*, vol. 42, no. 1, pp. 288-292.

Stikov, N., Perry, L.M., Mezer, A., Rykhlevskaia, E., Wandell, B.A., Pauly, J.M. and Dougherty, R.F., 2011. Bound pool fractions complement diffusion measures to describe white matter micro and macrostructure. *NeuroImage*, vol. 54, no. 2, pp. 1112-1121.

Stomper, P.C. and Margolin, F.R., 1994. Ductal carcinoma in situ: the mammographer's perspective. *AJR.American Journal of Roentgenology*, vol. 162, no. 3, pp. 585-591.

Sun, S., Liang, H., Cross, A.H. and Song, S., 2008. Evolving Wallerian degeneration after transient retinal ischemia in mice characterized by diffusion tensor imaging. *NeuroImage*, vol. 40, no. 1, pp. 1-10.

Sun, S., Liang, H., Schmidt, R.E., Cross, A.H. and Song, S., 2007. Selective vulnerability of cerebral white matter in a murine model of multiple sclerosis detected using diffusion tensor imaging. *Neurobiology of Disease*, vol. 28, no. 1, pp. 30-38.

Takahashi, M., Togao, O., Obara, M., van Cauteren, M., Ohno, Y., Kuro-O, M., Malloy, C., Hsia, C.C. and Dimitrov, I., 2010. Ultra-short echo time (UTE) MR imaging of the lung: Comparison between normal and emphysematous lungs in mutant mice. *Journal of Magnetic Resonance Imaging*, vol. 32, no. 2, pp. 326-333.

Thiessen, J.D., Zhang, Y., Zhang, H., Wang, L., Buist, R., Del Bigio, M.R., Kong, J., Li, X. and Martin, M., 2013. Quantitative MRI and ultrastructural examination of the cuprizone mouse model of demyelination. *NMR in Biomedicine*, vol. 26, no. 11, pp. 1562-1581.

Thompson, H.J., Lifshitz, J., Marklund, N., Grady, M.S., Graham, D.I., Hovda, D.A. and McIntosh, T.K., 2005. Lateral Fluid Percussion Brain Injury: A 15-Year Review and Evaluation. *Journal of Neurotrauma*, vol. 22, no. 1, pp. 42-75.

Traficante, D.D., 1991. Relaxation. Can T2, be longer than T1?. *Concepts in Magnetic Resonance*, vol. 3, no. 3, pp. 171-177.

Tyler, D.J., Robson, M.D., Henkelman, R.M., Young, I.R. and Bydder, G.M., 2007. Magnetic resonance imaging with ultrashort TE (UTE) pulse sequences: technical considerations. *Journal of Magnetic Resonance Imaging*, vol. 25, no. 2, pp. 279-289.

Underhill, H.R., Rostomily, R.C., Mikheev, A.M., Yuan, C. and Yarnykh, V.L., 2011. Fast bound pool fraction imaging of the in vivo rat brain: association with myelin content and validation in the C6 glioma model. *NeuroImage*, vol. 54, no. 3, pp. 2052-2065.

Underhill, H.R., Yuan, C. and Yarnykh, V.L., 2009. Direct quantitative comparison between cross-relaxation imaging and diffusion tensor imaging of the human brain at 3.0 T. *NeuroImage*, vol. 47, no. 4, pp. 1568-1578.

van Gelderen, P., de Zwart, J.A., Lee, J., Sati, P., Reich, D.S. and Duyn, J.H., 2012. Nonexponential T2* decay in white matter. *Magnetic Resonance in Medicine*, vol. 67, no. 1, pp. 110-117.

van Rooden, S., Versluis, M.J., Liem, M.K., Milles, J., Maier, A.B., Oleksik, A.M., Webb, A.G., van Buchem, M.A. and van der Grond, J., 2014. Cortical phase changes in Alzheimer's disease at 7T MRI: A novel imaging marker. *Alzheimer's & Dementia*, vol. 10, no. 1, pp. 19-26.

van Zijl, P. and Yadav, N.N., 2011. Chemical exchange saturation transfer (CEST): what is in a name and what isn't?. *Magnetic Resonance in Medicine*, vol. 65, no. 4, pp. 927-948.

Vavasour, I.M., Whittall, K.P., Li, D.K. and MacKay, A.L., 2000. Different magnetization transfer effects exhibited by the short and long T2 components in human brain. *Magnetic Resonance in Medicine*, vol. 44, no. 6, pp. 860-866.

Vermersch, P., Leys, D., Pruvo, J., Clarisse, J. and Petit, H., 1992. Parkinson's disease and basal ganglia calcifications: prevalence and clinico-radiological correlations. *Clinical Neurology and Neurosurgery*, vol. 94, no. 3, pp. 213-217.

Vernooij, M.W., Ikram, M.A., Wielopolski, P.A., Krestin, G.P., Breteler, M.M. and van der Lugt, A., 2008. Cerebral Microbleeds: Accelerated 3D T2*-weighted GRE MR Imaging versus Conventional 2D T2*-weighted GRE MR Imaging for Detection 1. *Radiology*, vol. 248, no. 1, pp. 272-277.

Vertinsky, A.T., Coenen, V.A., Lang, D.J., Kolind, S., Honey, C.R., Li, D. and Rauscher, A., 2009. Localization of the subthalamic nucleus: optimization with susceptibility-weighted phase MR imaging. *AJNR.American Journal of Neuroradiology*, vol. 30, no. 9, pp. 1717-1724.

Wang, L., Corum, C.A., Idiyatullin, D., Garwood, M. and Zhao, Q., 2013. T1 estimation for aqueous iron oxide nanoparticle suspensions using a variable flip angle SWIFT sequence. *Magnetic Resonance in Medicine*, vol. 70, no. 2, pp. 341-347.

Watanabe, H., Kumon, Y., Ohta, S., Sakaki, S., Matsuda, S. and Sakanaka, M., 1998. Changes in protein synthesis and calcium homeostasis in the thalamus of spontaneously hypertensive rats with focal cerebral ischemia. *Journal of Cerebral Blood Flow & Metabolism*, vol. 18, no. 6, pp. 686-696.

Wehrli, F.W., 2013. Magnetic resonance of calcified tissues. *Journal of Magnetic Resonance*, vol. 229, pp. 35-48.

Weiger, M., Hennel, F. and Pruessmann, K.P., 2010. Sweep MRI with algebraic reconstruction. *Magnetic Resonance in Medicine*, vol. 64, no. 6, pp. 1685-1696.

Weiger, M., Pruessmann, K.P. and Hennel, F., 2011. MRI with zero echo time: Hard versus sweep pulse excitation. *Magnetic Resonance in Medicine*, vol. 66, no. 2, pp. 379-389.

Weiger, M., Brunner, D.O., Dietrich, B.E., Müller, C.F. and Pruessmann, K.P., 2013a. ZTE imaging in humans. *Magnetic Resonance in Medicine*, vol. 70, no. 2, pp. 328-332.

Weiger, M., D.O. Brunner, M. Wyss, B.E. Dietrich, B.J. Wilm and K.P. Pruessmann. ZTE imaging with T1 contrast*Proceedings of the 22nd meeting of the ISMRM*. Milan, 2014.

Weiger, M., Pruessmann, K.P., Bracher, A., Köhler, S., Lehmann, V., Wolfram, U., Hennel, F. and Rasche, V., 2012. High-resolution ZTE imaging of human teeth. *NMR in Biomedicine*, vol. 25, no. 10, pp. 1144-1151.

Weiger, M., Stampanoni, M. and Pruessmann, K.P., 2013b. Direct depiction of bone microstructure using MRI with zero echo time. *Bone*, vol. 54, no. 1, pp. 44-47.

Weiger, M., Wu, M., Wurnig, M.C., Kenkel, D., Boss, A., Andreisek, G. and Pruessmann, K.P., 2015. ZTE imaging with long-T2 suppression. *NMR in Biomedicine*, vol. 28, no. 2, pp. 247-254.

Werring, D.J., Frazer, D.W., Coward, L.J., Losseff, N.A., Watt, H., Cipolotti, L., Brown, M.M. and Jager, H.R., 2004. Cognitive dysfunction in patients with cerebral microbleeds on T2*-weighted gradient-echo MRI. *Brain*, vol. 127, no. 10, pp. 2265-2275.

Wharton, S. and Bowtell, R., 2015. Effects of white matter microstructure on phase and susceptibility maps. *Magnetic Resonance in Medicine*, vol. 73, no. 3, pp. 1258-1269.

Wharton, S. and Bowtell, R., 2012a. Fiber orientation-dependent white matter contrast in gradient echo MRI. *Proceedings of the National Academy of Sciences*, vol. 109, no. 45, pp. 18559-18564.

Wharton, S. and Bowtell, R., 2012b. Fiber orientation-dependent white matter contrast in gradient echo MRI. *Proceedings of the National Academy of Sciences*, vol. 109, no. 45, pp. 18559-18564.

Wheeler-Kingshott, C.A. and Cercignani, M., 2009. About "axial" and "radial" diffusivities. *Magnetic Resonance in Medicine*, vol. 61, no. 5, pp. 1255-1260.

Wiggermann, V., Hernandez Torres, E., Vavasour, I.M., Moore, G.R., Laule, C., MacKay, A.L., Li, D.K., Traboulsee, A. and Rauscher, A., 2013. Magnetic resonance frequency shifts during acute MS lesion formation. *Neurology*, vol. 81, no. 3, pp. 211-218.

Wilhelm, M.J., Ong, H.H., Wehrli, S.L., Li, C., Tsai, P., Hackney, D.B. and Wehrli, F.W., 2012. Direct magnetic resonance detection of myelin and prospects for quantitative imaging of myelin density. *Proceedings of the National Academy of Sciences*, vol. 109, no. 24, pp. 9605-9610.

Wu, Q., Butzkueven, H., Gresle, M., Kirchhoff, F., Friedhuber, A., Yang, Q., Wang, H., Fang, K., Lei, H. and Egan, G.F., 2007. MR diffusion changes correlate with ultra-structurally defined axonal degeneration in murine optic nerve. *NeuroImage*, vol. 37, no. 4, pp. 1138-1147.

Wu, Z., Mittal, S., Kish, K., Yu, Y., Hu, J. and Haacke, E.M., 2009. Identification of calcification with MRI using susceptibility-weighted imaging: A case study. *Journal of Magnetic Resonance Imaging*, vol. 29, no. 1, pp. 177-182.

Xiong, Y., Mahmood, A. and Chopp, M., 2013. Animal models of traumatic brain injury. *Nature Reviews Neuroscience*, vol. 14, no. 2, pp. 128-142.

Yablonskiy, D.A., He, X., Luo, J. and Sukstanskii, A.L., 2014. Lorentz sphere versus generalized Lorentzian approach: What would lorentz say about it?. *Magnetic Resonance in Medicine*, vol. 72, no. 1, pp. 4-7.

Yablonskiy, D.A. and Sukstanskii, A.L., 2015. Generalized Lorentzian Tensor Approach (GLTA) as a biophysical background for quantitative susceptibility mapping. *Magnetic Resonance in Medicine*, vol. 73, no. 2, pp. 757-764.

Yablonskiy, D.A. and Sukstanskii, A.L., 2014. Biophysical mechanisms of myelin-induced water frequency shifts. *Magnetic Resonance in Medicine*, vol. 71, no. 6, pp. 1956-1958.

Yablonskiy, D.A., Luo, J., Sukstanskii, A.L., Iyer, A. and Cross, A.H., 2012. Biophysical mechanisms of MRI signal frequency contrast in multiple sclerosis. *Proceedings of the National Academy of Sciences*, vol. 109, no. 35, pp. 14212-14217.

Yamada, N., Imakita, S., Sakuma, T. and Takamiya, M., 1996. Intracranial calcification on gradient-echo phase image: depiction of diamagnetic susceptibility. *Radiology*, vol. 198, no. 1, pp. 171-178.

Young, I.R., Khenia, S., Thomas, D.G.T., Davis, C.H., Gadian, D.G., Cox, I.J., Ross, B.D. and Bydder, G.M., 1987. Clinical magnetic susceptibility mapping of the brain. *Journal of Computer Assisted Tomography*, vol. 11, no. 1, pp. 2-6.

Zappala, G., de Schotten, M.T. and Eslinger, P.J., 2012. Traumatic brain injury and the frontal lobes: what can we gain with diffusion tensor imaging?. *Cortex*, vol. 48, no. 2, pp. 156-165.

Zhang, J., Chamberlain, R., Etheridge, M., Idiyatullin, D., Corum, C., Bischof, J. and Garwood, M., 2014. Quantifying iron-oxide nanoparticles at high concentration based on longitudinal relaxation using a three-dimensional SWIFT look-locker sequence. *Magnetic Resonance in Medicine*, vol. 71, no. 6, pp. 1982-1988.

Zhang, J., Idiyatullin, D., Corum, C.A., Kobayashi, N. and Garwood, M., 2015. Gradient-modulated SWIFT. *Magnetic Resonance in Medicine*, vol. 75, no. 2, pp. 537-546.

Zheng, W., Haacke, E.M., Webb, S.M. and Nichol, H., 2012. Imaging of stroke: a comparison between X-ray fluorescence and magnetic resonance imaging methods. *Magnetic Resonance Imaging*, vol. 30, no. 10, pp. 1416-1423.

Zhong, K., Leupold, J., von Elverfeldt, D. and Speck, O., 2008. The molecular basis for gray and white matter contrast in phase imaging. *NeuroImage*, vol. 40, no. 4, pp. 1561-1566.

Zhou, R., Idiyatullin, D., Moeller, S., Corum, C., Zhang, H., Qiao, H., Zhong, J. and Garwood, M., 2010. SWIFT detection of SPIO-labeled stem cells grafted in the myocardium. *Magnetic Resonance in Medicine*, vol. 63, no. 5, pp. 1154-1161.

Zhu, W., Qi, J., Zhan, C., Shu, H., Zhang, L., Wang, C., Xia, L., Hu, J. and Feng, D., 2008. Magnetic resonance susceptibility weighted imaging in detecting intracranial calcification and hemorrhage. *Chin Med J*, vol. 121, no. 20, pp. 2021-2025.

LAURI JUHANI LEHTO

MRI is a complicated yet very flexible medical imaging modality. This study explored brain imaging applications for a novel MRI technique titled SWIFT that has a minimal delay between excitation and acquisition. Conventionally, no delay would imply no phase contrast, but here SWIFT phase contrast is shown to be feasible for detection of brain calcifications and brain structures. SWIFT magnitude contrast is shown to be very sensitive to loss of myelinated axons after a traumatic brain injury.

UNIVERSITY OF
EASTERN FINLAND

uef.fi

PUBLICATIONS OF
THE UNIVERSITY OF EASTERN FINLAND
Dissertations in Health Sciences

ISBN 978-952-61-2067-6
ISSN 11798-5706